DEVELOPMENT OF FOURIER DOMAIN OPTICAL COHERENCE TOMOGRAPHY FOR APPLICATIONS IN DEVELOPMENTAL BIOLOGY

by

Anjul Maheshwari Davis

Department of Biomedical Engineering
Duke University

Date:_________________________
Approved:

____
Dr. Joseph A. Izatt, Supervisor

____
Dr. Glenn Edwards

____
Dr. Nirmala Ramanujam

____
Dr. Florence Rothenberg

____
Dr. Tuan Vo-Dinh

Dissertation submitted in partial fulfillment of
the requirements for the degree of Doctor
of Philosophy in the Department of
Biomedical Engineering in the Graduate School
of Duke University

2008

ABSTRACT

DEVELOPMENT OF FOURIER DOMAIN OPTICAL COHERENCE TOMOGRAPHY FOR APPLICATIONS IN DEVELOPMENTAL BIOLOGY

by

Anjul Maheshwari Davis

Department of Biomedical Engineering
Duke University

Date:________________________
Approved:

____
Dr. Joseph A. Izatt, Supervisor

____
Dr. Glenn Edwards

____
Dr. Nirmala Ramanujam

____
Dr. Florence Rothenberg

____
Dr. Tuan Vo-Dinh

An abstract of a dissertation submitted in partial
fulfillment of the requirements for the degree
of Doctor of Philosophy in the Department of
Biomedical Engineering in the Graduate School
of Duke University

2008

Copyright by
Anjul Maheshwari Davis
2008

Abstract

Developmental biology is a field in which explorations are made to answer how an organism transforms from a single cell to a complex system made up of trillions of highly organized and highly specified cells. This field, however, is not just for discovery, it is crucial for unlocking factors that lead to diseases, defects, or malformations. The one key ingredient that contributes to the success of studies in developmental biology is the technology that is available for use. Optical coherence tomography (OCT) is one such technology. OCT fills a niche between the high resolution of confocal microscopy and deep imaging penetration of ultrasound. Developmental studies of the chicken embryo heart are of great interest. Studies in mature hearts, zebrafish animal models, and to a more limited degree chicken embryos, indicate a relationship between blood flow and development. It is believed that at the earliest stages, when the heart is still a tube, the purpose of blood flow is not solely for convective transport of oxygen, nutrients and waste, but also to induce shear-related protein gene expression that results in maturation of the organism. Yet, to this date, the simple question of "what initiates cardiac pumping resulting in blood flow?" has not been answered. This is primarily because imaging tools have lacked the spatial, temporal and depth resolution to image the complete embryonic heart in development. Earlier work has demonstrated the potential of OCT for use in studying chicken embryo heart development, however quantitative measurement techniques still needed to be developed. In this dissertation I present technological developments I have made towards building an OCT system to study chick embryo heart development. I will describe: 1) a swept-source OCT with extended imaging depth; 2) a spectral domain OCT system for non-invasive small animal imaging; 3) Doppler flow imaging and techniques for quantitative blood flow measurement in living chicken embryos; and 4) application of the OCT system that was developed in the Specific Aims 2-5 to test hypotheses generated by a finite element model which treats the embryonic chick heart tube as a modified peristaltic pump.

Contents

Abstract iv

List of Tables ix

List of Figures x

Acknowledgements xii

1. General Background and Significance 1

- 1.1 Optical Coherence Tomography 1
- 1.2 Fourier-Domain Optical Coherence Tomography 2
  - 1.2.1 Spectral-Domain Optical Coherence Tomography 3
  - 1.2.2 Swept-Source Optical Coherence Tomography 4
  - 1.2.3 Image Resolution 5
  - 1.2.4 Imaging Depth 6
  - 1.2.5 Imaging Speed 8
- 1.3 Significance for Developmental Biology 8
  - 1.3.1 Animal Models 9
  - 1.3.2 Current Imaging Technologies In Developmental Biology 9
- 1.4 Embryonic Heart Development 13
  - 1.4.1 Animal Models for Heart Development 14
  - 1.4.2 Milestones of Heart Development 15
  - 1.4.3 Relationship Between Blood Flow and Heart Development 17
- 1.5 Applications of OCT for Imaging Chicken Embryo Development 18
- 1.6 Design Considerations for Chick Embryo Imaging 19

2. Research Aims 21

3. The Design and Demonstration of Swept-Source Optical Coherence Tomography Imaging Using a Novel Method to Extend Imaging Depth 22

3.1 Background 22

3.2 Theoretical Analysis 24

3.2.1 Imaging Depth Limitation 24

3.2.2 Heterodyne SSOCT 25

3.3 Experimental Setup 27

3.4 Results 28

3.5 Conclusions 32

4. Development of 1310 nm Spectral Domain Optical Coherence Tomography System for Non-invasive 3D Imaging of Living Embryonic Chick Hearts 34

4.1 Background 34

4.2 Design and Methods 35

4.2.1 SDOCT System Design 35

4.2.1.1 InGaAs SDOCT Spectrometer 37

4.2.1.2 SDOCT Microscope 38

4.2.1.3 SDOCT Pivoting Microscope Scanner 40

4.2.2 SDOCT Data Acquisition and Processing 44

4.2.2.1 DC Subtraction 45

4.2.2.2 Dispersion Correction 45

4.2.2.3 Re-Sampling and Fast Fourier-Transform 47

4.2.3 System Characterization 48

4.2.4 Experimental Methods 52

4.3 Results 53

4.4 Discussion 55

4.5 Conclusions 56

5. Development of Doppler Optical Coherence Tomography and Spectral Doppler Velocimetry for *In vivo* Quantitative Measurement of Blood Flow Dynamics 58

5.1 Background 58

5.2 Methods 60

5.2.1 Doppler OCT Imaging 60

5.2.2 Spectral Doppler Velocimetry. 63

5.2.3 Phase Unwrapping 64

5.2.4 Determining Vessel Diameter, Volumetric Flow Rate, and Shear Rate. 66

5.2.2 Extraembryonic Vasculature Imaging Experimental Methods 66

5.3 Validation 68

5.4 Results 69

5.4.1 Extraembryonic Vasculature Imaging 69

5.5 Discussion 75

6. Application of Spectral-Domain Optical Coherence Tomography and Spectral Doppler Velocimetry to the Study of Blood Flow in the Embryonic Heart Tube 78

6.1 Background 78

6.1.2 Mechanism of Blood Flow in the Early Embryonic Heart Tube 79

6.1.3 Hypothesis 82

6.2 Methods 83

6.3 Results 85

6.3.1 Center line velocity dynamics between inflow, center, and outflow regions of the heart tube have distinct forward and backward flow characteristics relative to the contractile wave location 85

6.3.1.1 Inflow Blood Velocity Dynamics 86

6.3.1.2 Central Heart Tube Blood Flow Dynamics 90

6.3.1.3 Outflow Tract Blood Flow Dynamics 94

6.3.1.4. Comparison of Blood Flow Dynamics Between Inflow Tract, Center Tube, and Outflow Tract 98

6.3.2 Outflow Cushions Cause Secondary Blood Flow Peak 100

6.3.3 Peak Blood Flow Velocities Exceed the Contractile Wave Speed 103
6.4 Discussion 104
6.5 Conclusions 106
7. Future Directions 107
7.1 The Embryonic Chick Heart Tube is Not an Impedance Pump...................................... 107
7.2 Study Hemodynamics During Development.. 109
7.3 Correlation Between Blood Flow Dynamics and Electrical Action Potential 110
7.4 Simultaneous Multi-site SDV Measurement.. 110
7.5. Doppler and SDV Applications in Zebrafish 111
Appendix 1. Pivoting Microscope Solidworks Design 112
Appendix 2. Matlab Code for Two-Dimensional Phase Unwrapping 114
Appendix 3. Matlab Code for Alignment of Multiple SDV Plots 122
References 123
Biography 130

List of Tables

Table 1: Milestones of early heart development in different species 15

Table 2: Finite element simulation parameters 85

List of Figures

Figure 1: Michelson interferometer 2

Figure 2: Fourier domain OCT 3

Figure 3: Fourier transform relationship 4

Figure 4: Imaging methods compared by their resolution and imaging depth capabilities 13

Figure 5: SEM images of key stages of chick heart development 17

Figure 6: Heterodyne swept-source OCT system utilizing acousto-optic modulators 27

Figure 7: Interferograms taken using heterodyne SSOCT 29

Figure 8: Falloff measurements for (a) homodyne and (b) heterodyne SSOCT 30

Figure 9: A-scans of a -60 dB calibrated reflector at a 1.0 mm pathlength difference 31

Figure 10: *In vivo* images of human anterior segment using (a) homodyne and (b) heterodyne SSOCT techniques 32

Figure 11: 1310 nm spectral domain OCT schematic and processing steps 35

Figure 12: ZEMAX design of SDOCT spectrometer with 512 pixel InGaAs CCD camera 36

Figure 13: Optical design and PSF of SDOCT microscope adapted for collinear imaging with Zeiss microscope 38

Figure 14: ZEMAX optical system design and Solidworks mounting design of pivoting microscope. 39

Figure 15: Point spread function and spot diagram through focus for pivoting microscope 42

Figure 16: Spot diagrams from nine scan positions of pivoting microscope. 44

Figure 17: 1310 SDOCT Falloff 50

Figure 18: OCT and microscope images of Air Force resolving power test chart 51

Figure 19: SDOCT volumetric reconstruction of a Stage 38 STII medaka 52

Figure 20: Chick embryo preparation 53

Figure 21: Volume images of developing chicken embryo at HH 9 (top row), HH 12 (middle row), and HH 15 (bottom row) 55

Figure 22: Doppler processing flow chart 60

Figure 23: Phase wrapped Doppler image 62

Figure 24: Minimum and maximum detectable velocity range 62

Figure 25: SDV measurement and volume rendering of chicken embryo vessel 63

Figure 26: Pivoting scan of flow phantom 65

Figure 27: SDOCT setup for extraembryonic vessel imaging 67

Figure 28: Validation of Doppler flow measurements 68

Figure 29: Blood flow measurements from three extraembryonic vessels 71

Figure 30: Doppler OCT time series of blood flow through chicken embryo heart tube at HH 11 and HH 14 72

Figure 31: Spectral Doppler velocimetry measurements from the outflow tract (oft) at HH 11 and HH 14 74

Figure 32: Geometry for finite element model (a) Model dimensions in passive state 79

Figure 33: SDOCT system with pivoting microscope arm 83

Figure 34: SDV and finite element modeling from inflow tract 89

Figure 35: SDV and finite element modeling from center of heart tube 91

Figure 36: SDV measurements from center of tube in three separate embryos. 92

Figure 37: Center-tube velocity plots N=3 93

Figure 38: SDV and finite element modeling from outflow tract 95

Figure 39: SDV measurements from outflow tract of five separate embryos. 96

Figure 40: Outflow tract velocity plot N=5 97

Figure 41: Average (blue) and standard deviation (red) of blood flow dynamics at two different locations in the heart tube 99

Figure 42: Outflow cushions cause secondary peak 100

Figure 43: Illustration of changes in lumen area during contraction 101

Figure 44: No secondary peak in the center region of the heart tube 102

Figure 45: SDV measurements from the outflow tract (a) and primitive ventricle (b) demonstrate peak velocities faster than contractile wave speed 102

Acknowledgements

What a road it has been. Countless people have supported me throughout this journey. Whether it has been physically, emotionally, or intellectually, I could not have gotten here without their support. I would like to thank Dr. Joe Izatt for first adopting me into his lab and then being not only the best mentor ever (it's true, there is a plaque that says so), but becoming a trusted friend. Dr. Florence Rothenberg has been my driving force through this project. If it was not for her, this project would never have started. But beyond that, her continuous reinforcement of the importance of my work has kept me going. Neal Shepherd really guided me through the last part of my thesis. Neal, Chapter 6 is as much yours as it is mine. Also, all of my lab mates over the years. Guys (and girls), thank you for keeping me young. I am honored to have been the queen of this hive.

On a personal note, I would like to thank my family. Thank you for the everlasting love and support. I know that wherever I am in my life you are always proud of me. I am proud of being your daughter, sister, sister-in-law, and aunt. Lastly I want to thank my husband, Bryce. Bryce has been my right-hand man. And I mean that literally, on more than one occasion he served as my right-hand when I burned mine. Bryce has supported me physically, intellectually, emotionally, and spiritually. With all the resistance I gave to accepting his help, I could not have done this without him.

"If you are not learning, you are dying."

Thank you all for helping me stay alive.

1. General Background and Significance

1.1 Optical Coherence Tomography

Optical coherence tomography (OCT) is a non-invasive optical imaging modality that acquires depth resolved images of biological samples in both two- and three-dimensions. OCT is essentially an optical analog to ultrasound imaging. However, it takes advantage of the short wavelength of light to achieve higher resolution images. As a tradeoff, shorter wavelengths suffer from higher attenuation in biological samples, so the depth of penetration achieved using OCT is typically 1-3 mm in non optically- transparent samples.

OCT was first introduced by Huang, et. al [D. Huang et al., 1991] in 1991. It is based on low-coherence interferometry which utilizes low temporal coherent light sources (superluminescent diode) or ultra-short pulsed (femtosecond) lasers to perform coherence gating. First generation OCT systems, called “time-domain” OCT (TDOCT) use depth-ranging to measure the time-of-flight of the optical signal reflected off of biological samples. This measurement provided depth-resolved contrast based on reflectivities in sample microstructure. The heart of OCT systems is a Michelson interferometer as shown in Figure 1. In a Michelson interferometer, low coherent light is split into reference and sample arms using a beam splitter, or in the more common fiber-based systems, a fiber-optic coupler. Reflections off the sample are mixed with the reflection off the reference mirror. Amplitude and time-of-flight delays from the sample reflections are measured by translating the reference mirror and measuring the resultant interferometric signal using a photodiode detector. Constructive interference only occurs when the path-lengths between the reference mirror and sample reflectors are equal within the coherence length of the light source. Two-dimensional (B-mode) and three-dimensional (C-mode) images are created by laterally (and longitudinally) scanning the sample arm light across the sample.

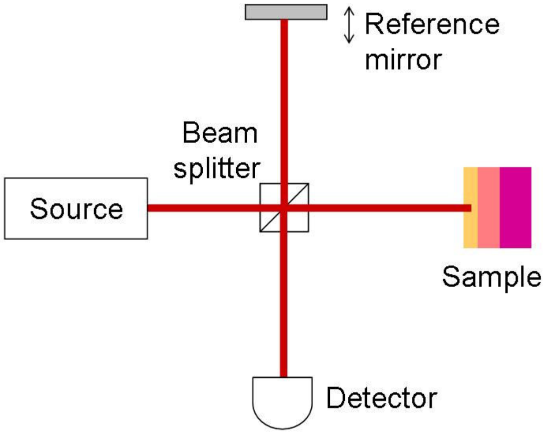

Figure 1: Michelson interferometer. Light from a low-coherence source is split into a reference and sample arm using a beam splitter. Reflections off the sample layers and reference mirror is recombined and the resulting interferometric signal measured using a photodiode detector.

1.2 Fourier-Domain Optical Coherence Tomography

Recently, a new generation of OCT technology has been developed, called “Fourier-domain” OCT (FDOCT). Based on Wolf’s solution to the inverse scattering problem for determining the structure of weakly scattering objects, FDOCT was first demonstrated in 1995 by Fercher, et. al [A. F. Fercher et al., 1995] In 2003, Leitgeb [R. Leitgeb et al., 2003] and Izatt [M. A. Choma et al., 2003] showed that FDOCT techniques provide sensitivities two to three orders of magnitude greater than TDOCT. It wasn’t until these papers were presented that FDOCT was widely accepted by the OCT population. This sensitivity advantage would enable imaging hundreds of times faster than TDOCT without sacrificing image quality. FDOCT utilizes direct acquisition of the spectral interferogram for depth resolved measurement of back-scattered light. There are two methods for acquiring the spectral interferogram in FDOCT: 1) spectral-domain OCT (SDOCT) and 2) swept-source OCT (SSOCT). Our lab was one of the earliest adapters of FDOCT, and for this reason, the remainder of this dissertation will concentrate on these techniques.

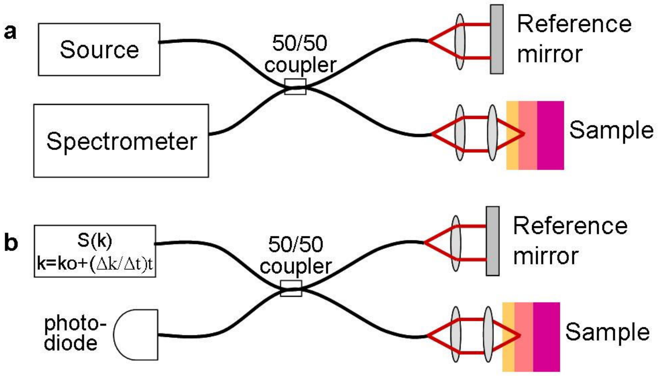

Figure 2: Fourier domain OCT. FDOCT techniques measure the spectral interferogram in two ways: (a) spectral domain OCT, which simultaneously measures the spectral interferogram using a spectrometer in the detection arm of the interferometer; and (b) swept-source OCT, which utilizes a light source that rapidly sweeps a narrow linewidth across broad band light.

1.2.1 Spectral-Domain Optical Coherence Tomography

In FDOCT the reference mirror is kept at a fixed pathlength and the interferogram is measured as a function of optical wavenumber, *k*. In SDOCT, that spectral interferogram is acquired using a spectrometer in the detection arm of the interferometer (Figure 2a). The measured photocurrent signal generated by *n* reflectors is given by

$$i(k) \propto S(k)\left[\begin{array}{l} R_R + \sum_n R_n + 2\sqrt{R_R}\sum_n \sqrt{R_n}\cos\left(2k\left[z_R - z_n\right]\right) + \\ \qquad\qquad\qquad 2\sum_n \sum_{m\neq n} \sqrt{R_n R_m}\cos\left(2k\left[z_n - z_m\right]\right) \end{array}\right] \tag{1}$$

where *i*(*k*) is the detector photocurrent and $k = 2\pi/\lambda$; *S*(*k*) is the source power spectral density; R_R and R_n are the reflectivities of the reference and n^{th} sample reflector, respectively; and z_R and z_n are the positions of the reference and n^{th} sample reflector, respectively. The first two terms in the brackets on the left-hand side represent non-interferometric spectral artifacts. The third term represents the cross-interferometric terms, and the fourth term represents the autocorrelation artifact. We calculate the back-scattered depth profile using the Fourier transform relationship between frequency and depth, as illustrated in Figure 3. *n* reflectors at various depths in the sample corresponds to a sinusoidal function with a frequency proportional to the pathlength difference between the reflector and reference arm (Figure 3a – c). The measured interferometric signal is the combination *n* interferograms multiplied by the source spectrum (Figure 3d). The Fourier transform produces an A-scan (Figure 3e) where each delta-function corresponds to the depth location of a sample reflector. DC, autocorrelation, and complex conjugate ambiguity image artifacts are also present in the A-scans and will be further discussed in Specific Aim 1.

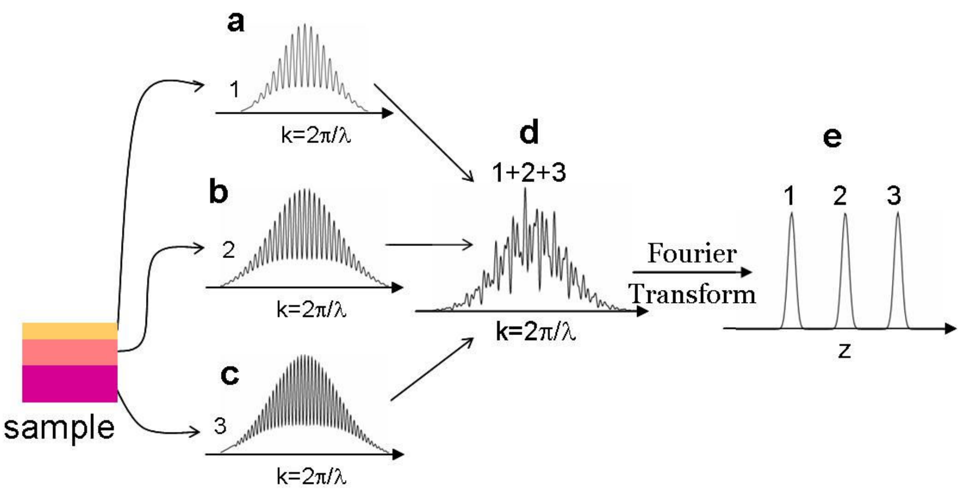

Figure 3: Fourier transform relationship. The detected spectral interferogram (d) is the combination of interferograms from reflectors at different depths in the sample (a)-(c). The Fourier transform of (d) produces an A-scan (e) where each peak location corresponds to the depth of the reflector.

1.2.2 Swept-Source Optical Coherence Tomography

In SSOCT, instead of using a spectrometer in the detection arm of the interferometer, a light source that rapidly scans a narrow spectral linewidth across broadband light is used. The spectral interferogram is collected, as a function of time, using a photodiode detector (Figure 2b). Wavenumber in Equ. 1 is parameterized in time *t* by the relationship $k = k_o + t(dk/dt)$, where k_o is the starting wavenumber, and d*k*/d*t* is the nonlinear sweep velocity. This sweeping leads to the conversion of pathlength differences in the auto- and cross-terms to an electronic frequency in *i(t)*, the time-varying photocurrent. The cross-frequencies have instantaneous values of $\omega_n = (dk/dt)(z_R - z_n)$, while the autocorrelation frequencies have instantaneous values of $\omega_{nm} = (dk/dt)(z_n - z_m)$. The time-varying photocurrent in SSOCT becomes

$$i(t) \propto S(t)\left\{ R_R + \sum_n R_n + 2\sqrt{R_R}\sum_n \sqrt{R_n}\cos[2(\omega_R t + \phi_n)] + 2\sum_n \sum_{m \neq n} (R_n R_m)^{1/2}\cos[2(\omega_{nm} t + \phi_{nm})] \right\}. \quad (2)$$

where $\phi_n = k_o(z_R - z_n)$ and $\phi_{nm} = k_o(z_n - z_m)$. Similar to SDOCT, the depth resolved A-scan is produced by using the Fourier transform relationship between temporal frequency and depth.

1.2.3 Image Resolution

The highest priority requirements typically cited for all OCT applications including developmental biology studies, are axial and lateral resolution, imaging speed, and penetration depth into the sample. In most OCT systems the axial and lateral resolutions are separable, with the axial resolution determined by the characteristics of the OCT interferometer “engine,” and the lateral resolution determined by the sample arm delivery optics.

The lateral resolution in OCT, as in microscopy, is determined by the focusing optics of the light incident on the sample. The lateral resolution, Δx, is the diffraction limited spot size on the sample and is given by:

$$\Delta x = \frac{4\lambda_o}{\pi}\frac{f_{obj}}{d} \quad (3)$$

where λ_o is the center wavelength of the light source, f_{obj} is the focal length of the objective lens and *d* is the spot size of the beam on the objective lens. There is a tradeoff in the lateral resolution as a function of depth. The depth of focus is related to the lateral resolution by:

$$2z_R = \frac{\pi \Delta x^2}{2\lambda_o} \quad (4)$$

The Rayleigh range, z_R, decreases as the lateral resolution increases. Thus, tighter focusing will decrease the depth of focus and therefore the lateral resolution in regions outside of the depth of focus will suffer. It is important to consider the sample of interest and design the focusing optics to optimize the lateral resolution throughout the depth of interest. The primary sample of interest for this dissertation is the chicken embryo heart tube which typically has a diameter between 200 and 300 μm. In developing an OCT system for imaging the chick embryo heart tube, it is optimal to design the sample arm focusing optics to have a large enough depth of focus such that the lateral resolution is constant through the entire heart tube being imaged. To achieve a depth of focus of 200 - 300 μm the lateral resolution while maintaining the highest resolution for 1310 nm OCT sample arm needs to be between 13 μm and 16 μm.

The axial, or depth, resolution of an OCT system is determined by the coherence length of the light source. The coherence length, l_c, is the spatial width (FWHM) of the field autocorrelation interferogram and can be determined by the Fourier transform of the source power spectrum. The axial resolution, δz, is inversely proportional to the optical bandwidth, and is determined by the following relationship:

$$\delta z = l_c = \frac{2 \ln 2}{\pi} \frac{\lambda_o^2}{\Delta\lambda} \tag{5}$$

where $\Delta\lambda$ is the optical bandwidth, of the light source (assuming a Gaussian spectrum). For optimal axial resolution, it is desirable to utilize broadband light sources. Drexler et. al has provided an extensive review of light sources throughout the wavelength range of 500 nm to 1600 nm for ultra-high resolution OCT imaging [W. Drexler, 2004].

1.2.4 Imaging Depth

The penetration depth of OCT imaging depends upon the wavelength and power of the light source, the system implementation, and ultimately the absorption and scattering properties of the sample under investigation. The most common light source wavelengths used in OCT are

830 nm and 1310 nm. For imaging ophthalmic structures, 830 nm is the preferred wavelength because of the increased transparency of the aqueous and vitreous humors, the higher axial resolution for the same bandwidth afforded by Equ. 5, and the ability to use less expensive silicon-based detectors. For non-ophthalmic applications such as developmental biology, 1310 nm is the preferred wavelength because of reduced scattering in tissue at this wavelength. Typical penetration depths in tissues at 1310 nm are between 1-3 mm, ideal for early embryonic chick hearts which reside less than 2 mm in depth during much of the early stages of development.

The imaging depth realized using FDOCT systems is limited by two mechanisms, which do not have counterparts in time-domain OCT system: (a) the spectral sampling interval (which limits the maximum depth observable) and (b) the system spectral resolution (which leads to a falloff of SNR with depth). The maximum imaging depth in FDOCT systems is given as [T. M. Yelbuz et al., 2003]:

$$\Delta z_{\max} = \frac{1}{4\delta_s k}, \tag{6}$$

where $\delta_s k$ is the spectral sampling interval of the FDOCT system (which is limited by the pixel spacing of the CCD in SDOCT systems). Published maximum imaging depths for 1310 nm SDOCT systems are on the order of 2.0 mm [S. H. Yun et al., 2003].

A second parameter which limits the imaging depth in FDOCT systems is SNR falloff. Falloff is the degradation of the signal sensitivity as a function of imaging depth due to fringe washout. The -6 dB falloff depth, derived from the analysis reported by Yun, et., al [S. H. Yun et al., 2003] is given by:

$$\Delta z_{-6dB} = \frac{\ln 2}{\pi \delta_r k} \tag{7}$$

where Δz_{-6dB} is the imaging depth at which the signal-to-noise ratio is reduced by half and $\delta_r k$ is the spectral resolution of the system. The spectral resolution is limited by the instantaneous linewidth of the laser in SSOCT systems, and by the spectrometer optics in SDOCT systems.

1.2.5 Imaging Speed

Imaging speed in scanning implementations of OCT (as opposed to full-field approaches) is dependent upon the A-scan rate. SDOCT systems achieve A-scan rates, limited by the readout rate of line scan CCD cameras, of 10-50 kHz, and SSOCT systems have recently been demonstrated with A-scan rates up to 300 kHz [R. Huber et al., 2005] [R. Huber et al., 2006]

1.3 Significance for Developmental Biology

Understanding developmental processes has been limited by our ability to visualize the cellular and morphological changes that occur over time, as well as by our limited ability to visualize and quantify functional, mechanical, and electrical changes *in situ*. Advanced research in molecular biology techniques has enabled genetic screening and the development of genetically manipulated animal models. Many of the recent innovations have been directed toward elucidating the genotypical changes that occur in developing biological specimens, with less emphasis on visualizing the phenotypic expression of the normal and altered gene. OCT has begun to be used as a novel microscopy technique for imaging early developmental events that take place in organisms [M. J. Wolf et al., 2006; A. Mariampillai et al., 2007] In recent years, the unique imaging capabilities of OCT have been directed toward vertebrate animal models such as the chick and mouse [T. M. Yelbuz et al., 2002; M. W. Jenkins et al., 2006; M. W. Jenkins et al., 2007] The high-resolution, real-time, non-invasive imaging capabilities of FDOCT make it ideally suited for monitoring the growth and development of biological tissues over time.

1.3.1 Animal Models

The field of developmental biology utilizes a wide selection of animal model systems ranging from simple prokaryotes, insects, fish and amphibians, to higher complex models such as small birds and mammals. Non-mammalian species including fruit flies (*Drosophila melanogaster*), fish (zebrafish, *Brachydanio rerio*; medaka, *oryzias*), and amphibians (African frog, *Xenopus laevis*) are often used because they have known genomes, rapid reproductive and developmental cycles, and are easy to care for and handle. Vertebrates such as chickens (*Gallus domesticus*) and small mammals (mouse, *Mus musculus*; rat, *Rattus norvegicus*) are preferred because the development and function of their organ systems are more closely related to human systems. Advances in genetics and molecular biology permit modification and monitoring of the genome and gene expression, and have provided the opportunity to study human diseases using these biological models [T. Doetschman et al., 1987]. Several imaging technologies are available for studying these models, all of which have their advantages and limitations. The primary area of developmental biology focused on in this dissertation is the chicken embryo heart. Here I will describe imaging technologies that are currently used for *in vivo* studies in small animal embryonic hearts.

1.3.2 Current Imaging Technologies In Developmental Biology

Imaging has played an important role in investigations of embryonic development. Several conventional imaging modalities have been adapted for studies in developmental biology. These techniques include histology, ultrasound, and confocal microscopy. Histology has been the gold standard for many years; however, the drawbacks are significant. Fixation methods shrink tissue, enlarge cavities, and alter relative relationships between structures. Also, histology requires sacrifice of the animal, thus preventing longitudinal and functional investigations.

Magnetic resonance microscopy (MRM) is a magnetic resonance imaging (MRI) technique developed for studying small animals. Compared to 0.5-2T clinical MRI systems, MRM produces high resolution images by utilizing magnetic fields as strong as 17.6T. 3D cardiac imaging of chick embryos using magnetic resonance was first demonstrated in 1986 [S. N. Bone et al.]. Since then, several studies have utilized high resolution MRM for 3D imaging of chick embryo cardiac morphology [E. L. Effmann et al., B. R. Smith et al., B. R. Smith et al., B. Hogers et al., B. R. Smith, T. M. Yelbuz et al., X. Zhang et al.]. Using a 9.4T MRM system, Zhang, et al presented 3D images of chick embryo hearts at resolutions as high as 25 μm^3 [T. M. Yelbuz et al., X. Zhang et al.]. For sufficient image contrast and resolution, the chick embryo hearts were perfused with contrast agents and image acquisition times lasted approximately 30 hours. The heart was also arrested in diastole to eliminate motion artifacts during the several hours acquisition period. These requirements for high resolution images inhibit the ability to conduct longitudinal studies. MRM imaging is also not a readily available technique. Currently, there are only a few MRM facilities available in the world. This is mainly because operating these systems require a high level of training and greater than $3 million in capital equipment for establishment of a facility [R. R. Maronpot et al.].

Micro-computed tomography (micro-CT) is a dedicated x-ray computed tomography system for high resolution structural imaging of small animals. Although micro-CT is primarily used for imaging skeletal structure, it has recently been demonstrated for imaging soft tissues. 4D micro-CT imaging of a mouse heart using respiratory-gated acquisition produced images with resolutions near 200 μm [C. T. Badea et al.]. Non-gated micro-CT techniques can achieve 80 μm [D. W. Holdsworth et al.] resolution however data acquisition can last up to 30 minutes and the sample must be sacrificed [M. J. Paulus et al.]. Longitudinal imaging of embryonic development using micro-CT is implausible due to the limited resolution and long acquisition times.

Ultrasound biomicroscopy (UBM) utilizes high frequency transducers (40-55 MHz) to achieve axial and lateral resolutions as high as 28 μm and 62 μm, respectively [F. S. Foster et al., 2002]. UBM is commonly used to image embryonic mouse hearts and assess cardiac function [C. K. Phoon et al., 2000, 2002]. Though noninvasive, ultrasound techniques require the transducer to be in acoustic contact with the sample. Currently, the highest resolutions achieved with UBM are insufficient for imaging early stage embryo development, such as chick hearts, with diameters as small as 200 µm.

Historically, optical techniques such as white-light and fluorescence microscopy have dominated the visualization of developmental biology, and much of this has relied on the examination of histologically-processed specimens at single time-points for assessing changes in normal and abnormal (mutated) morphology during development. Advances in optical imaging such as confocal and multiphoton microscopy [W. Denk et al., 1990; J. B. Pawley, 2006]. have enabled three-dimensional optical sectioning of tissue, from both histologically-processed specimens and also *in vivo*. A variant to confocal microscopy, called selective plane illumination microscopy (SPIM) utilizes a sheet of illuminating light oriented orthogonally to the direction of confocal detection. SPIM has been used to visualize small developmental biology specimens including zebrafish and Drosophila embryos [J. Huisken et al., 2004]. In addition to these types of multi-photon microscopy, other nonlinear microscopy techniques, such as second and third harmonic generation microscopy, have been used to image developing specimens, offering the potential to visualize ultrastructure in organogenesis [S.-W. Chu et al., 2003].

The development of genetically-encoded and expressed fluorescent proteins such as green-fluorescent-protein (GFP) have enabled the site-specific labeling of cells and structures with functional relevance linked to gene-expression profiles and timing [R. Y. Tsien, 1998]. Despite these advances, limited imaging penetration depth precludes the use of these methods for larger developmental biology specimens, where visualization to depths greater than a few hundred microns is desired. In addition, the use of fluorophores, including GFP and its variants, can produce cytotoxic by-products following excitation, including reactive oxygen species, which can limit the overall viability of specimens, particularly for long-term (days-weeks) imaging studies that are essential for tracking developmental changes.

Important biological events that occur early in development have been difficult to observe *in vivo*. Current versions of widely used imaging techniques have limitations of spatial or temporal resolution, imaging depth, or are impractical for longitudinal studies. For example one key event, initiation of blood flow, occurs in the chicken embryo after only 2 days of development. At this stage, the heart tube is only 100 μm to 200 μm in diameter yet it can reside over 200 μm deep inside the egg. Optical microscopy techniques such as confocal has high enough resolution to resolve the heart tube structure at this stage but the shallow penetration depth often precludes imaging of the entire heart tube. Ultrasound biomicroscopy, on the other hand, has sufficient imaging penetration but even the highest resolution ultrasound technology is limited in contrast and resolution to visualize the chicken embryo heart at the early stages [T. C. McQuinn et al., 2007]. As illustrated in Figure 4, the non-contact, high-speed, high-resolution capabilities of OCT fill a niche to provide spatial and temporal resolutions that permit simultaneous investigations of *in vivo* embryonic structure and function.

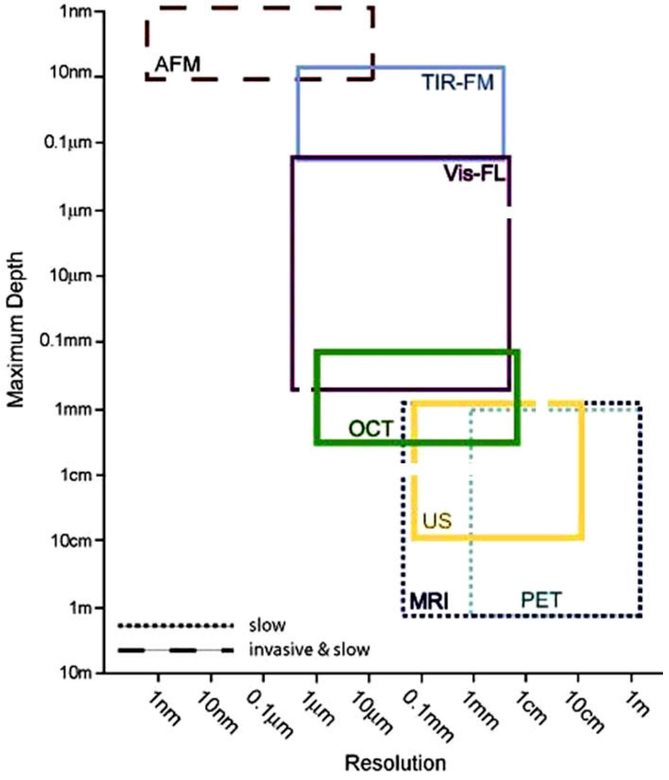

adapted from: Nature Rev. Mol. Cell Biol. 4, SS16-SS21 (2003)

Figure 4: Imaging methods compared by their resolution and imaging depth capabilities. OCT fills a niche between the resolution of optical microscopies (Vis-FL) and imaging depth of ultrasound (US). TIR-FM, total internal reflection fluorescence microscopy; AFM, atomic force microscopy; MRI, magnetic resonance imaging; PET, positron emission tomography.

1.4 Embryonic Heart Development

Embryonic heart development is a rapid and dynamic process. The cardiovascular system is one of the first organs to develop. It has long been thought that perturbations that occur during embryonic heart development lead to congenital heart defects. In the United States, congenital heart defects are present in 1% of live births and are the most common malformation among newborns [AHA, 2004]. A total of 4109 deaths due to congenital heart defects were recorded in 2001[AHA, 2004]. Still our fundamental understanding of heart development is limited. However, with advances in technology as well as increased collaborations between biologists and engineers, great strides are to be made in the field.

1.4.1 Animal Models for Heart Development

Animal models such as mouse, chicken, and zebra fish embryos are commonly used for studying cardiovascular development. Mouse embryos provide a mammalian analog to human development. A drawback to the mouse embryo, however, is that it develops within the a muscular uterus and are often hidden by placental tissue. This limits in vivo imaging studies to using technologies that can penetrate through the uterus and placenta, such as ultrasound [C. K. Phoon et al., 2000, 2002; C. K. Phoon and D. H. Turnbull, 2003] or MRI. As discussed above, these technologies have limitations in resolution or imaging rate, respectively. Alternatively procedures have been established where the mouse embryos are surgically accessed for imaging. However these procedures are invasive making them less desirable. Zebrafish are a common animal model used today for studying heart development [B. M. Weinstein and M. C. Fishman, 1996] [J. R. Hove et al., 2003] [H. M. Stern and L. I. Zon, 2003] [H. Zhu and L. I. Zon, 2004] [M. Liebling et al., 2005; A. S. Forouhar et al., 2006]. Imaging techniques such as confocal microscopy are well suited for studying zebrafish because it is small, relatively transparent. Also, the zebrafish genome is well understood which makes them attractive for testing genetic links to normal and abnormal development. Although their hearts develop into only a two-chambered system, it is believed that zebrafish heart tube development may parallel mammalian development. This dissertation primarily concentrates on development of imaging technology for studying heart development in the chicken embryo animal model. Just like mouse embryos, the warm-blooded vertebrate chicken heart develops into a four-chambered system in the same process as humans. Additionally, like zebrafish, imaging the chicken embryo requires no surgical procedure and they require very little maintenance.

Table 1: Milestones of early heart development in different species

	Human	Chick	Mouse	Zebrafish
Migration of precardiac cells	15 – 16 days	HH 4 (18 – 22 hrs)	7 dpc	5.5 hpf
Heart tube formation	22 days	HH 9 (29 – 33 hrs)	8 dpc	19 hpf
Coordinated contractions	23 days	HH 10 (33 – 38 hrs)	8.5 dpc	22 hpf
Looping	23 days	HH 11 (40 – 45 hrs)	8.5 dpc	33 hpf
Cushion formation	28 days	HH 17 (50 – 56 hrs)	9.5 dpc	48 hpf

Adapted from [M. C. Fishman and K. R. Chien].
HH – Hamburger-Hamilton staging [V. Hamburger and H. L. Hamilton, 1951]; [B. J. Martinsen, 2005]; dpc – days post conception, hpf – hours post fertilization

1.4.2 Milestones of Heart Development

The timing of some important stages of heart development in the human, mouse, chick, and zebra fish is provided in Table 1. In the chick, the heart tube coalesces by about 30 hours of development or Hamburger-Hamilton (HH) stage 8+/9- [V. Hamburger and H. L. Hamilton, 1951]. For visual reference, Figure 5 contains a series of scanning electron microscopy (SEM) images of the chick heart tube at several key stages of development that were published by Männer [J. Männer, 2000] Following the formation of the heart tube (Figure 5a), at HH 10 (36 hours), coordinate contractions begin. The heart tube expands in size and the first indications of the tube differentiating into the outflow and primitive ventricle portions are observed [J. Männer, 2000]. Additionally, the heart tube begins to bend or loop to the right, indicating entrance into the "looping" process which will last several stages and is an important step leading to septation into four chambers (Figure 5b). The first phase of looping, called "dextral looping" is usually complete by HH 12 (Figure 5c) [J. Männer, 2000]. In the phase following dextral looping, (between HH 12 and HH 18) the ‘c’-shaped heart tube continues to loop into more of an ‘s’-shaped curve (Figure 5d).

The heart tube consists of three layers, myocardium, endocardium, and sandwiched between the two, cardiac jelly. The myocardium is the outer muscular layer of the heart tube that actively contracts. The endocardium is the inner layer of the heart tube that lines the lumen through which blood flows. Studies have shown that this endocardial layer of cells express genes related to shear-stress induced by blood flow [B. C. Groenendijk et al., 2004; B. C. Groenendijk et al., 2005]. During the early stages of development a thick layer called cardiac jelly exists between the myocardium and endocardium that is filled by extracellular matrix [C. L. Davis, 1924]. The cardiac jelly is incompressible and is thought to provide an important function for enabling blood flow in the heart tube. By creating a thicker heart tube wall with cardiac jelly, the heart tube is not required to expend as much energy for sufficient contraction and propagation of blood [A. Barry, 1948]. After HH 12 the cardiac jelly in the outflow and inflow regions of the tube thickens and create a bulge or “cushion”. Valves and septa of the heart develop from these endocardial cushions [A. D. Person et al., 2005]. Expansion of the endocardial cushions is mediated by regulated secretion of extracellar matrix components by the myocardial cells [E. L. Krug et al., 1985]. The extracellular matrix excretion is believed to consist of chondroitin sulfate and hyaluronan which are highly charged hydrophilic molecules believed to promote swelling, thus forming the cushions [F. J. Manasek, 1970] [F. J. Manasek, 1975]. Still, much is unknown about the process of cushion formation. After cushion formation, mesenchymal cells have been observed in the cushions [B. M. Patten et al., 1948]. A more detailed review of the development of these cushions has be provided by Person, et al [A. D. Person et al., 2005]. Finite element simulations of blood flow through an embryonic heart tube modeled with and without endocardial cushions [L. A. Taber et al., 2007] suggest that these cushions serve an even greater purpose than valve precursors, which will be described in further detail in Chapter 6. By the end of the looping process, the outflow and primitive atria have been brought adjacent to each other (Figure

5f), in preparation for septation into a chambered system. Septation is the process which occurs during stages HH 16 – HH 34 of chick heart development and indicates the formation of septa, or walls, that divide heart into chambers [B. J. Martinsen, 2005].

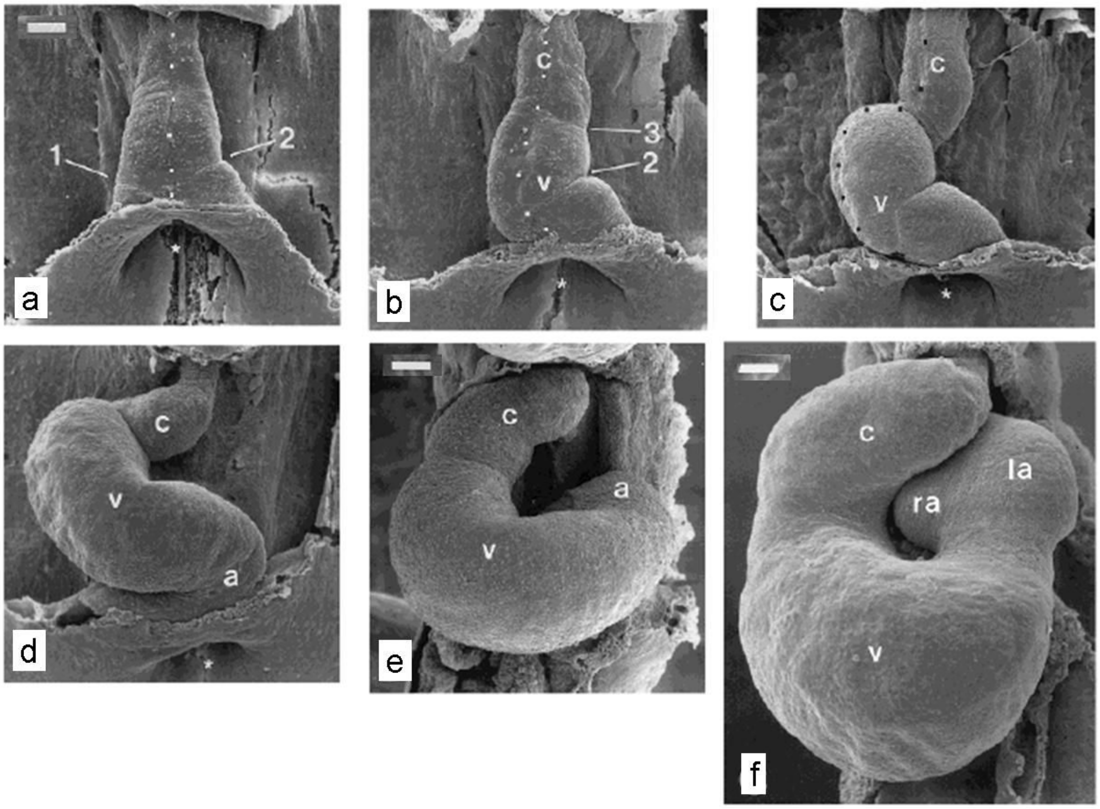

Figure 5: SEM images of key stages of chick heart development. (a) Heart tube begins to fuse at HH 9. (b) The fully fused heart tube begins looping process as indicated by dextral bend in primitive ventricle at HH 10/11-. (c) Bending and laterlization of primitive ventricle region during looping. (d) The end of dextral-looping at HH 12/13. (e) Transformation from c-shaped loop to s-shped loop at HH 15. (f) Atria and outflow (conus) appose each other prior to septation at HH 18. v, primitive ventricle; c, primitive outflow tract; r/l a, primitive atria. Scale bar = 100 µm. Images taken from [J. Männer, 2000].

1.4.3 Relationship Between Blood Flow and Heart Development

Structural and functional development of the chick embryo heart occur simultaneously. Around HH 12, just when the heart tube is in the looping stages, blood flow is first observed. Unlike adult hearts, it is believed that at this early stage of development blood flow is not used for convective transport of oxygen and nutrients or removal of waste [W. W. Burggren]. These investigators have presented data that suggests blood flow is necessary for normal structural development. Modification of intracardiac blood flow patterns by ligation of the vitelline vein can alter ventricular structure and reduce cardiac performance [B. Hogers et al., ; K. Tobita and B. B. Keller, ; N. T. Ursem et al.] perhaps by inducing changes in shear-stress related gene expression [B. C. Groenendijk et al., 2005]. The role of intracardiac flow and resulting fluid forces as epigenetic factors for heart development has also been demonstrated in zebra fish [J. R. Hove et al., 2003]. Although these studies have established a link between blood flow and structural development, the precise genes and structural changes altered by early blood flow and implications for normal cardiogenesis are still incompletely understood. Limitations in research towards this understand strongly lay in the inability to image structure and quantify blood flow simultaneously. Confocal microscopy and ultrasound biomicroscopy are the only two modalities that are so far capable of providing such information. Unfortunately the shallow penetration depth of confocal microscopy and limited spatial resolution of ultrasound render them non ideal for studying chick embryo development. OCT, on the other hand has demonstrated imaging depths of 1-2 mm and resolution less than 12 μm which makes it an attractive modality for studying the chick embryo heart.

1.5 Applications of OCT for Imaging Chicken Embryo Development

OCT was first demonstrated for imaging chick embryo cardiovascular systems in 2002 [T. M. Yelbuz et al., 2002]. In this study, embryos between stages HH 14-22 were removed from the shell and placed in a sterilized petri dish with 1.8% buffered potassium chloride until the hearts were “frozen” in diastole. Dynamic imaging of the beating heart was also demonstrated using a live HH 15 embryo. B-scan images of the looping heart were acquired at 4 kHz line rates, using a time-domain 1310 nm OCT system. B-scans at 10 μm intervals were acquired for volume reconstruction of the hearts. The results of this study showed that transverse and longitudinal images of the outflow tract correlate to histology, at the micrometer level. Volumetric reconstructions were also presented.

In this study the embryos were placed in a solution to cause relaxation of the embryonic heart and “freeze” in diastole to reduce artifacts due to motion from beating. A technique for 4D embryonic chick heart imaging was presented using gated TDOCT [M. W. Jenkins et al., 2006]. In this study, HH 13 chicken embryo hearts were excised from the embryo and paced using field stimulation at 1 Hz (normal heart cycle is 3-4 Hz) which was synchronized with data acquisition. Images were acquired using a time-domain OCT system at 4 kHz line rate. 3D volumes were acquired for several stages of the heart beat cycle. Acquisition of the entire 4D dataset took less than 5 minutes and the axial and transverse resolution was 14 μm and 10 μm, respectively. Although this demonstration required excision of the heart and pacing approximately 4 times slower than the normal heart rate, it showed that gated OCT can provide enough detail for quantification of the changes that occur during the cardiac cycle and proved necessary for accurate measurement of volumetric dimensions. More recently, 4D images were presented using an ultra-high speed SSOCT system with a frequency domain mode locked laser [M. W. Jenkins et al., 2007]. This demonstration acquired OCT images at 100,000 lines per second which enabled acquired 4D datasets without gating. Continuing advancements in OCT technologies will help understand the mechanisms of cardiovascular development in the vertebrate chick embryo.

1.6 Design Considerations for Chick Embryo Imaging

Jenkins et. al. outlined the speed requirements for accurate 4D OCT imaging of the chick embryo heart, *in vivo* [M. W. Jenkins et al., 2007]. They concluded the necessary imaging speed to minimize displacement errors in 4D images to 10 μm and with ideal spatial sampling is 7,111,000 lines per second. Currently the fastest OCT systems (based on FDML lasers) is 300,000 lines per second [R. Huber et al., 2005] [R. Huber et al., 2006]. Further development of rapid swept source lasers makes 7,111 kHz line rate a very real possibility. At this imaging rate, the major limitations are availability of fast A/D conversion, bit depth and computer processor and memory capabilities.

For whole embryo or tissue-level imaging, resolutions on the order of 10 μm are acceptable. Cellular or subcellular imaging, however, requires ultra-high resolution OCT implementations. Current ultra-high resolution OCT systems in the 1310 nm wavelength range have reported resolutions less than 2 μm axially and laterally [K. Bizheva et al., 2003; W. Y. Oh et al., 2005].

An additional requirement unique to small animal imaging is that typically a long working distance between the OCT scanner and the sample is needed, and simultaneous access to the sample via conventional microscopy may also be useful. The long working distance is required so that additional experimental tools (i.e., micromanipulators, electrodes, micropipettes) may be accommodated in the animal chamber. Implementation of a long working distance requires the use of custom large-aperture focusing optics that can also accommodate video microscopy.

At the start of this project, conventional OCT technologies (TDOCT) provided maximum imaging at 4 kHz line rate, with axial and lateral resolutions on the order of 10 μm. Also, functional extensions, such as Doppler imaging required additional system hardware to the system. The goal of this project was to build a high-speed OCT system for small animal imaging with the additional capability of functional Doppler blood flow imaging.

2. Research Aims

The overall aim of this project was to create an optical coherence tomography system for application in the fields of developmental biology. The system requirements included sufficient resolution, imaging depth, and imaging speed to enable non invasive, *in vivo* imaging of small animals and biological samples. Additionally, I developed an extension of Doppler imaging, to study blood flow dynamics in the developing chicken embryo heart tube. These goals were fulfilled through the completion of the following aims:

Specific Aim 1: Design, build, and demonstrate a heterodyne swept-source optical coherence tomography imaging system with extended imaging depth (Chapter 3).

Specific Aim 2: Design and build a 1310 nm spectral-domain optical coherence tomography system for non invasive, 3D imaging of living embryonic chick hearts (Chapter 4).

Specific Aim 3: Develop Doppler OCT techniques for quantitative blood flow measurements in living chicken embryos (Chapter 5).

Specific Aim 4: Use the instrumentation I have developed to perform quantitative tests on hypotheses generated from a finite element model which treats the developing heart tube as a modified peristaltic pump (Chapter 6).

3. The Design and Demonstration of Swept-Source Optical Coherence Tomography Imaging Using a Novel Method to Extend Imaging Depth

Here we describe a heterodyne SSOCT system that enables complete resolution of complex conjugate ambiguity and removal of non-interferometric signals. We show that frequency shifting provides a method for complex conjugate ambiguity resolution that circumvents signal falloff that occurs by placing samples at a large pathlength mismatch. Through electronic demodulation, we gain access to the in-phase and quadrature components of the interferometric signal and enable wavenumber triggering, which eliminates the necessity for over sampling. This system was intended for applications in developmental biology where the increased imaging depth would enable visualization of the entire chick embryo heart, including portions of the inflow that can reside 2 – 3 mm from the surface of the egg yolk. limitations in the sweep speed of our swept source laser, however, inhibited application for small animal imaging. Instead I successfully demonstrated heterodyne SSOCT for *in vivo* imaging of the entire human corneal anterior segment.

3.1 Background

Although the advancement of FDOCT techniques has enabled imaging 100 times faster than TDOCT while maintaining sufficient sensitivity, it has come with costs. FDOCT techniques are limited in imaging depth and suffer from two important sources of artifacts. The first, called "complex conjugate ambiguity," arises because the Fourier transform of the real-valued spectral interferometric signal is Hermitian symmetric. This results in sample reflectors at a positive displacement, $+\Delta x$, with respect to the reference reflector, being superimposed on those at a negative displacement, $-\Delta x$. The second source of artifact, termed "dc artifact," originates from the non-interferometric light and autocorrelation from sample reflectors, which transform to $\Delta x = 0$, and thereby obscure reflectors positioned at zero pathlength difference. These artifacts can be removed by retrieval of the complex interferometric signal. Additionally, retrieval of the complex interferometric signal effectively doubles the imaging depth by removal of the complex conjugate ambiguity.

Previous techniques for acquiring the complex Fourier-domain interferometric signal have relied on collecting the in-phase and quadrature (π/2-shifted) components generated by phase shifting interferometry [M. Wojtkowski et al., 2002]. or 3X3 interferometry [Michael A. Choma et al., 2003; M. V. Sarunic et al., 2005]. These techniques are constrained to homodyne insofar as both the reference and sample arm optical fields have the same phase velocity. Homodyne detection is required for SDOCT systems that employ spectrometers coupled to charge accumulation detectors such as charge-coupled devices (CCDs) and photodiode arrays. In SSOCT, however, a current-generating photodiode is employed, which enables the spectral interferometric signal to be encoded with a characteristic heterodyne beat frequency. Phase-shifting interferometry requires acquisition of multiple images and therefore is not instantaneous. 3X3 interferometry is an instantaneous technique for acquisition of the complex interferometric signal. However, *NXN* fiber couplers are wavelength dependent, making it difficult to accurately reconstruct the full complex interferometric signal.

Two techniques for complex conjugate artifact removal using heterodyne SSOCT have previously been reported. The first described a system utilizing electro-optic phase modulators to introduce a heterodyne beat frequency in the reference arm [J. Zhang et al., 2005]. A drawback to this technique is that electro-optic modulators are polarization dependent and highly dispersive, thus requiring methods for controlling the polarization and compensation of the group-velocity dispersion. The second technique utilized acousto-optic modulators for heterodyne SSOCT [S. H. Yun et al., 2004]. This system entails an interferometric topology in which the frequency shifting components were placed between the sample and the receiver. Frequency shifting elements, such as electro- and acousto-optic modulators, are typically lossy. Placing these elements downstream from the sample prevents the ability to compensate power losses due to light exposure limitations on *in vivo* samples. Additionally, both published techniques required over sampling of the intrinsic signal bandwidth due to the heterodyne modulation, and the latter technique required a computationally intensive algorithm for re-sampling the acquired data into frequency space.

is the goal was to build a heterodyne SSOCT system at 1310 nm that allows for efficient detection of the complex interferometric signal, thus having the potential for increased signal-to-noise ratio (SNR). Imaging depth capabilities over 4 mm can be valuable for applications such as endoscopy, small animal imaging, and human anterior segment imaging. This system was intended for applications in developmental biology where the increased imaging depth would enable visualization of the entire chick embryo heart, including portions of the inflow that can reside 2 -3 mm from the surface of the egg yolk.

3.2 Theoretical Analysis

3.2.1 Imaging Depth Limitation

The imaging depth achieved using FDOCT systems is limited by two mechanisms, the spectral sampling interval (which limits the maximum depth observable) and the system spectral resolution (which leads to a falloff of SNR with depth). The maximum imaging depth in FDOCT systems is described as [M. A. Choma et al., 2003].

$$\Delta z_{\max} = \frac{1}{4\delta_s k} \tag{8}$$

where $\delta_s k$ is the spectral sampling interval of the FDOCT system. In SDOCT systems, the spectral sampling interval is limited by the pixel spacing of the CCD. Reported maximum imaging depths for 1310 nm SDOCT systems are of the order of 2.0 mm [S. H. Yun et al., 2003]. Alternatively, in SSOCT systems, the spectral sampling interval is limited by the sampling rate of the temporally sweeping source frequency. Over 4.0 mm maximum imaging depth has been achieved for 1310 nm SSOCT systems [A. M. Davis et al., 2005].

The second parameter that limits the imaging depth in FDOCT systems is falloff. Falloff describes how the sensitivity of FDOCT systems degrades as a function of imaging depth due to fringe washout. The −6 dB falloff depth, derived from analysis reported by Yun et al [S. H. Yun et al., 2003] is given by

$$\Delta z_{-6dB} = \frac{\ln 2}{\pi \delta_r k} \qquad (9)$$

where $\Delta z_{-6\mathrm{dB}}$ is the imaging depth at which the SNR is reduced by half, and $\delta_r k$ is the spectral resolution of the FDOCT system. In SDOCT, the spectral resolution is limited by spectrometer optics and/or the pixel width of the CCD. The preceding expression for the −6 dB falloff point was derived assuming the spectral resolution of SDOCT systems is limited by the Gaussian beam profile in the spectrometer as opposed to the width of the CCD pixel. For SSOCT systems, the spectral resolution is defined by the instantaneous linewidth of the swept laser source. Since spectral sampling and spectral resolution are coupled in spectrometer-based SDOCT systems, they are more limited by falloff compared to SSOCT techniques. The −6 dB imaging depth of a 1310 nm SDOCT system was reported to be 1.6 mm [S. H. Yun et al., 2003]. In comparison, the −6 dB imaging depth for 1310 nm SSOCT is 3.7 mm, more than double the distance achieved using SDOCT.

3.2.2 Heterodyne SSOCT

The time-varying photocurrent signal detected in SSOCT is

$$i(t) \propto S(t)\left\{ R_R + \sum_n R_n + 2\sqrt{R_R}\sum_n \sqrt{R_n}\cos\left[2(\omega_R t + \phi_n)\right] + 2\sum_n \sum_{m\neq n} (R_n R_m)^{1/2}\cos[2(\omega_{nm} t + \phi_{nm})]\right\} \qquad (10)$$

If the reference arm optical field is shifted by some beat frequency ω_D, then Equ. 10 becomes

$$i(t) \propto S(t)\left\{ R_R + \sum_n R_n + 2\sqrt{R_R}\sum_n \sqrt{R_n}\cos\left[2(\omega_R - \omega_D)t + 2\phi_n\right] + 2\sum_n \sum_{m\neq n} (R_n R_m)^{1/2}\cos[2(\omega_{nm} t + \phi_{nm})]\right\}. \qquad (11)$$

After frequency shifting, the autocorrelation and source spectral terms remain centered at baseband, while the cross-interference terms are recentered around ω_D. While the Fourier transform of *i(t)* remains Hermitian symmetric, the transform of fringes generated by pathlength differences of equal magnitude but opposite sign no longer overlap. This resolves complex conjugate ambiguity because positive displacements are above ω_D, while negative displacements are below ω_D as long as ω_D is larger than the maximum ω_n. If the wavenumber sweep is linear over a bandwidth sweep Δk that takes Δt seconds to complete, then ω_D corresponds to a pathlength shift of $z_D = \omega_D \Delta t / (2\Delta k)$. This shift does not lead to signal falloff as falloff in SSOCT occurs because the interferometric signal is integrated over the source linewidth at the photodiode. If the source linewidth is of the order of $2\pi/(z_R - z_n)$, then the linewidth spans an appreciable portion of the interferometric fringe. This decreases the fringe visibility, which decreases the peak height in the Fourier transform of *i(t)*. Frequency shifting creates a time-varying beat frequency that is independent of sweep speed or source linewidth and, as such, it is not susceptible to falloff.

The cross-interferometric signal can be recovered by bandpass filtering around ω_D with a noise equivalent bandwidth of $NEB = 2z_{\max} \Delta k / \Delta t$. If demodulation is performed the bandpassed signal is electronically mixed with orthogonal local oscillators with frequency ω_D. In this case, the in-phase (real) and quadrature (imaginary) parts of the complex interferometric signal can be recovered:

$$\begin{aligned} i_{\mathrm{Re}}(t) &= 2S(t)\sqrt{R_R}\sum \sqrt{R_n}\,\cos(\omega_n t + \phi_n), \\ i_{im}(t) &= 2S(t)\sqrt{R_R}\sum \sqrt{R_n}\,\sin(\omega_n t + \phi_n). \end{aligned} \tag{12}$$

Additionally, after demodulation, the interferometric signals are dependent only on the time-varying frequency ω_n, thereby enabling wavenumber triggering.

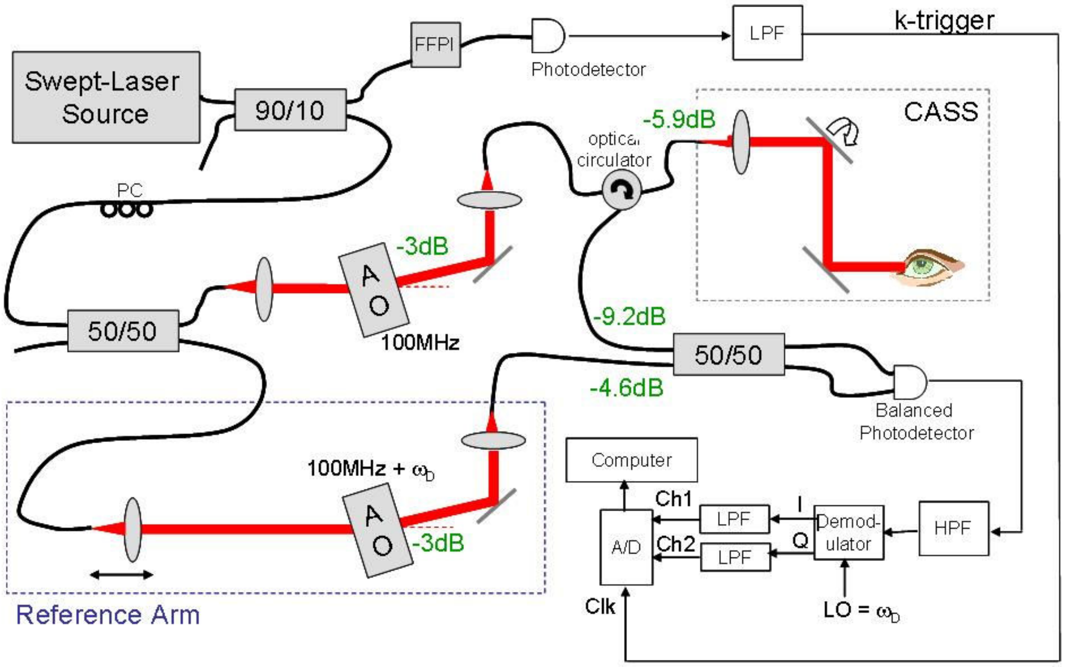
FFPI
Photodetector
LPF
k-trigger
Swept-Laser Source
90/10
PC
-5.9dB
optical circulator
CASS
-3dB
A O
100MHz
50/50
-9.2dB
50/50
-4.6dB
Balanced Photodetector
Computer
100MHz + ω_D
A O
-3dB
Ch1
LPF
I
Demod-ulator
HPF
A/D
Ch2
LPF
Q
Clk
LO = ω_D
Reference Arm

Figure 6: Heterodyne swept-source OCT system utilizing acousto-optic modulators. The swept-laser source has a center wavelength λ_o=1310 nm and bandwidth Δλ=100 nm. A balanced photoreceiver is used for DC artifact suppression. FFPI, Fiber Fabry-Perot Interferometer; PC, polarization controllers; AO, acousto-optic modulator; C, circulator; CASS, corneal anterior segment scanner.

3.3 Experimental Setup

We constructed the heterodyne SSOCT setup shown in Figure 6 using a fiber-based swept laser source (Micron Optics, Inc., λ=1310 nm, Δλ=100 nm, 250 Hz sweep rate), acousto-optic modulators (ACM-1002AA6 IntraAction, Corp.), and a New Focus balanced photoreceiver. The acousto-optic modulators (AOs) had a common center frequency of 100 MHz, one of which having a user-adjustable offset (ω_D) from that frequency. The diffraction efficiency of the AOs was measured to be 60%, and using the optical setup depicted in the figure, the maximum diffracted optical bandwidth recoupled into the circulator was 64 nm. To trigger each line acquisition, a 250 Hz clock was provided by the swept-laser source. Spectral interferogram samples evenly spaced in wavenumber were clocked into the data acquisition system using a fiber Fabry-Perot interferometer (FFPI, Micron Optics, Inc.). Ten percent of the swept-laser source output was delivered to the FFPI. Then the output was detected using a New Focus 125 MHz photoreceiver. The detected signal was passed through a 2.1 MHz low-pass filter and an electronic gain to produce an electronic comb, where each 5 V peak was evenly spaced in wavenumber. The wavenumber spacing was 0.1 nm, given by the free spectral range of the FFPI.

The heterodyne interferometric signal collected using the balanced photoreceiver was high-pass filtered (500 kHz) to remove the spectral and autocorrelation artifacts, then demodulated (RF Micro Devices RF2713) by mixing with a local oscillator (LO) of frequency ω_D. The in-phase and quadrature components were low-pass filtered (500 kHz cutoff frequency) and digitized in dual analog-to-digital (A/D) channels (National Instruments PCI 6115) using the clocking signal from the wavenumber trigger. The output power of the swept-laser source was 500 μW. There was approximately −6 dB source power attenuation in the system prior to the sample (−3 dB through the AO and −2.9 dB insertion loss into the fiber of the optical circulator), resulting in 60 μW illumination on the sample (cornea).

The SNR of the system, using a −60 dB calibrated reflector near zero pathlength difference, was measured to be 99 dB. The predicted SNR, assuming same signal power, was 112 dB. The heterodyne SSOCT setup described here places the AO in front of the sample. This design enables compensation of optical power loss from the AO and, therefore, the SNR of the system could be increased by use of a higher power laser source.

3.4 Results

To illustrate the behavior of the cross-interferometric term in Equ. 10 with the reference arm frequency shifted with respect to the sample arm, we show in Figure 7 the fringe patterns of typical interferograms at two pathlength differences, centered around zero, for homodyne (Figure 7a and Figure 7b) and heterodyne (Figure 7c and Figure 7d) SSOCT setups. The homodyne setup was measured by setting ω_D, the frequency difference between the two AOs, to zero. The fringe frequency for the cross-correlation term, when $\omega_D = 0$, was identical for equivalent positive (Figure 7a) and negative (Figure 7b) displacements, and it was thus ambiguous whether the pathlength difference was positive or negative. However, when ω_D =20 kHz, the fringe frequency for the positive displacement (Figure 7c) was higher than for a negative displacement (Figure 7d), as expected from Equ. 11, and therefore the positive and negative locations were resolved.

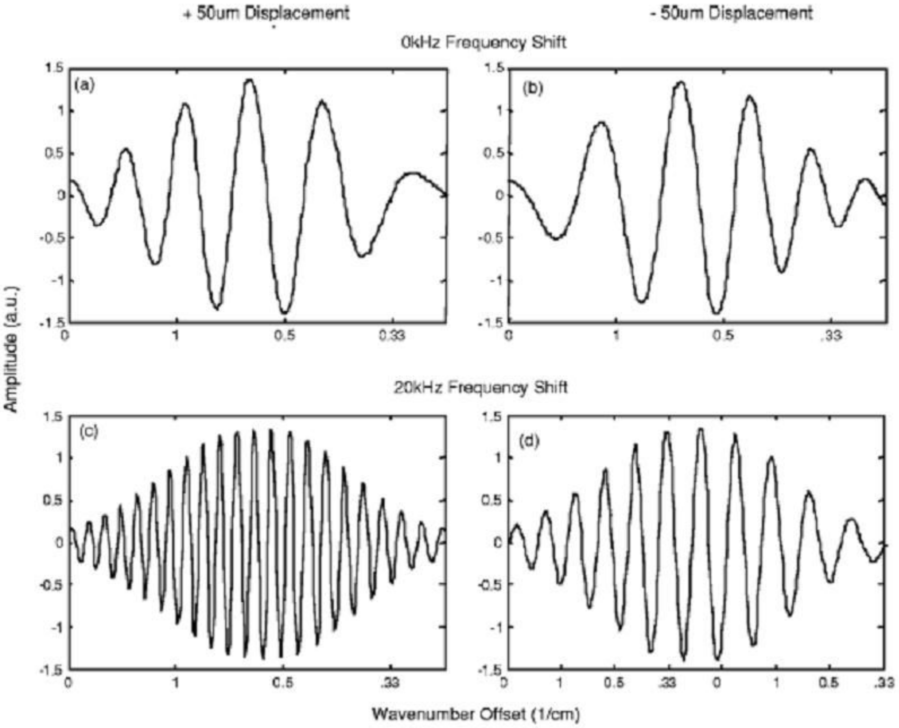

Figure 7: Interferograms taken using heterodyne SSOCT. (a) and (b) taken from a reflector at +50 µm and -50 µm pathlength difference, respectively, with a 0 kHz frequency shift, and (c) and (d) collected at the same pathlength difference, but with a 20 kHz frequency shift. By using heterodyne detection, reflectors at positive positions produce higher fringe frequencies than those at negative positions and therefore are unambiguously resolved. The chirped signal is a result of wavenumber triggering without demodulation, reinforcing the importance of demodulation when acquiring heterodyne data using a wavenumber trigger.

Figure 8 demonstrates that the signal falloff remained centered at zero pathlength difference, even as the electronic frequency was shifted. Figure 8a shows falloff centered at zero pathlength for homodyne SSOCT. By shifting the zero pathlength difference frequency to ω_D =1 MHz, the image contents were moved away from dc and bandpass filtered to remove the spectral artifacts. After filtering and demodulation, the falloff was recentered around zero frequency and the −3.5 dB signal attenuation out to a 4.0 mm scan depth was preserved.

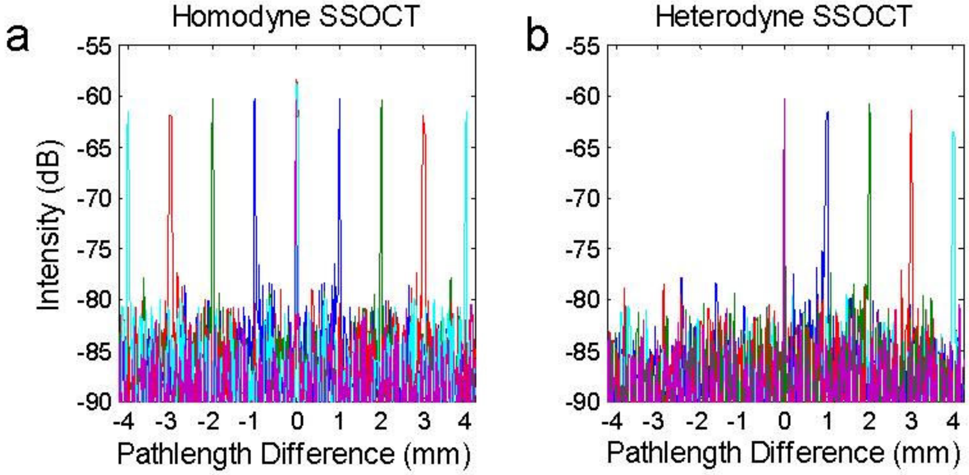

Figure 8: Falloff measurements for (a) homodyne and (b) heterodyne SSOCT. Acquired using setup in Figure 6; the -3.5 dB signal falloff was preserved using heterodyne SSOCT; -60 dB calibrated reflector used in sample arms; 1 MHz heterodyne frequency shift.

In Figure 9, complete removal of complex conjugate ambiguity and dc artifacts is demonstrated using heterodyne SSOCT. In the A-scan acquired using homodyne SSOCT (Figure 9a), the complex conjugate ambiguity artifact is clearly shown. At zero pathlength difference a strong dc peak from the noninterferometric spectral artifact is also present. By shifting the frequency of the reference arm by ω_D =1 MHz, the complex conjugate ambiguity was completely resolved (Figure 9b). Also, the spectral artifact located at dc was removed. There is, however, still present a small dc artifact that originated from a small (<0.1 V) dc offset from the demodulation board. As a result, this dc offset appeared as a small peak located at zero pathlength difference in the A-scans. The dynamic range of the system was limited to 25 dB by the input requirements of the demodulation board (<80 mV). As a result, we were able to demonstrate 25 dB extinction of the complex conjugate ambiguity artifact. In theory, however, the capability of the system to remove this artifact is not limited.

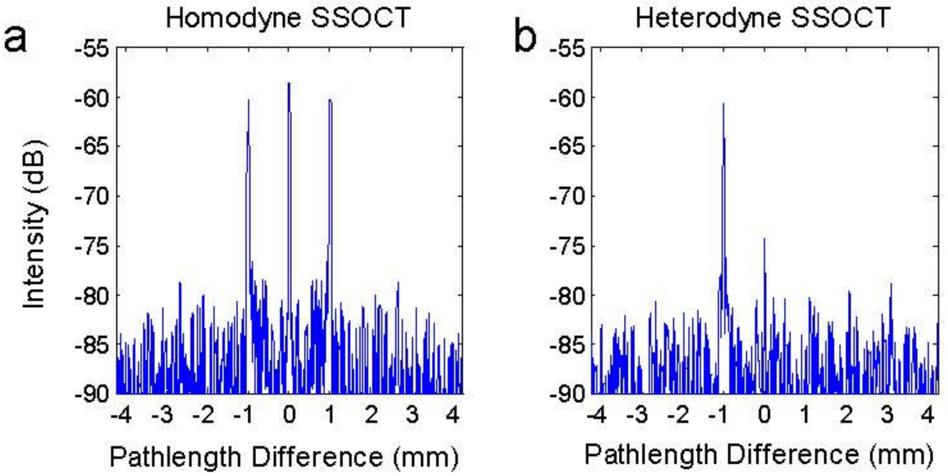

Figure 9: A-scans of a -60 dB calibrated reflector at a 1.0 mm pathlength difference. (a) A-scan showing unresolved complex conjugate ambiguity acquired using homodyne SSOCT. The complex conjugate ambiguity prevents distinguishing reflectors at +1.0 mm from those at -1.0 mm pathlength difference. Using heterodyne SSOCT (b), the complex conjugate ambiguity is resolved. The spectral artifact located at dc is also removed, however, a small artifact resulting from a dc offset in the electronic demodulator is present.

In vivo images acquired using homodyne and heterodyne SSOCT techniques are shown in Figure 10a and Figure 10b, respectively. These images are of the anterior segment of a human eye and were constructed using 500 lines/image acquired at a rate of 250 Hz. In the homodyne SSOCT image, the iris, cornea, and sclera were obscured by the mirror image arising from the complex conjugate ambiguity artifact. Using heterodyne SSOCT, however, the artifact was completely removed and the cornea, iris, and sclera were no longer obscured. It is evident that at least 6 mm of imaging depth is necessary to visualize the entire anterior segment.

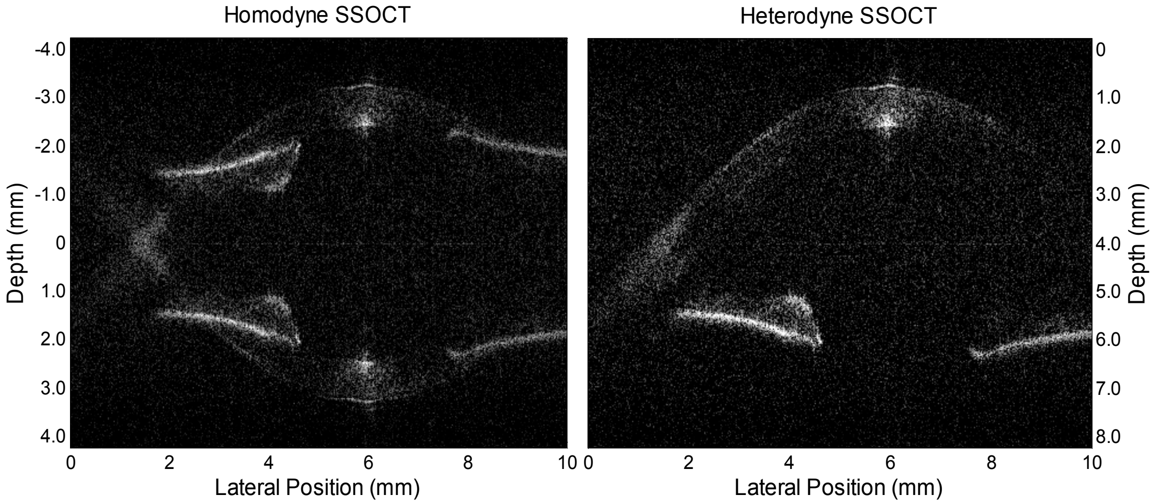

Figure 10: *In vivo* images of human anterior segment using (a) homodyne and (b) heterodyne SSOCT techniques. Complete complex conjugate ambiguity removal and doubling of the imaging depth is shown to be necessary in order to visualize the entire anterior segment of the eye

3.5 Conclusions

We demonstrated a heterodyne SSOCT technique using AOs for complex conjugate ambiguity and dc artifact removal. This technique provided double the imaging depth in human anterior segment of the eye. We also presented an efficient heterodyne SSOCT design that minimizes power losses after the sample, enabling an increased SNR. This technique enables the zero pathlength difference to be shifted away from electronic dc with no penalty due to finite laser linewidth falloff. Combined with coherent demodulation, this technique provides access to the entire complex interferometric signal without oversampling, as the method also enables data acquisition using wavenumber triggering, thus eliminating computationally intensive re-sampling algorithms. Although the available laser source power and speed was insufficient for *in vivo* small animal imaging due to increase absorption in tissue and motion artifacts, we demonstrated *in vivo* human anterior segment images with more than 6 mm imaging depth.

During this project developments in Indium Gallium Arsenide (InGaAs) detectors have produced linescan cameras which can operate at 10s of kilohertz line rates. InGaAs semiconductors have optimized responsivity in the near IR wavelengths (1000 – 1600 nm). Yun, et. al. published work on the development of a 1310 nm SDOCT system using a high-speed InGaAs line scan CCD [S. H. Yun et al.]. We have designed and built an SDOCT system using the same InGaAs CCD optimized for small animal imaging which is described in the next chapter.

4. Development of 1310 nm Spectral Domain Optical Coherence Tomography System for Non-invasive 3D Imaging of Living Embryonic Chick Hearts

Here we describe a spectral-domain OCT system designed for *in vivo* embryonic chick heart imaging. This system has been optimized for 19 kHz cross-sectional and rapid (< 7 s) volumetric imaging of small animals and biological samples. We present design parameters and demonstrate the application of this system for studies in developmental biology. These studies show the utility of SDOCT for tracking small animal development over time.

4.1 Background

The goal in Chapter 3 was to build a SSOCT system for small animal imaging. Unfortunately, at the time, swept-source laser development was at the very early stages so the source output power was too low for sufficient SNR (90 dB) in biological tissue. Additionally the sweep speed of the source was only 250 Hz, producing one image every 2 seconds. This imaging rate would require fixation of the sample or gated acquisition to avoid severe motion artifacts from *in vivo* imaging of non-anesthetized small animals. In the meanwhile developments in Indium Gallium Arsenide (InGaAs) detectors were also continuing. InGaAs semiconductors have optimized responsivity in the near IR wavelengths (1000 – 1600 nm). Yun, et. al. published work on the development of a 1310 nm SDOCT system using a high-speed InGaAs line scan CCD [S. H. Yun et al., 2003]. As a result, our goal was to design and build an SDOCT system using the same InGaAs CCD optimized for non invasive, *in vivo* imaging of embryonic chick hearts.

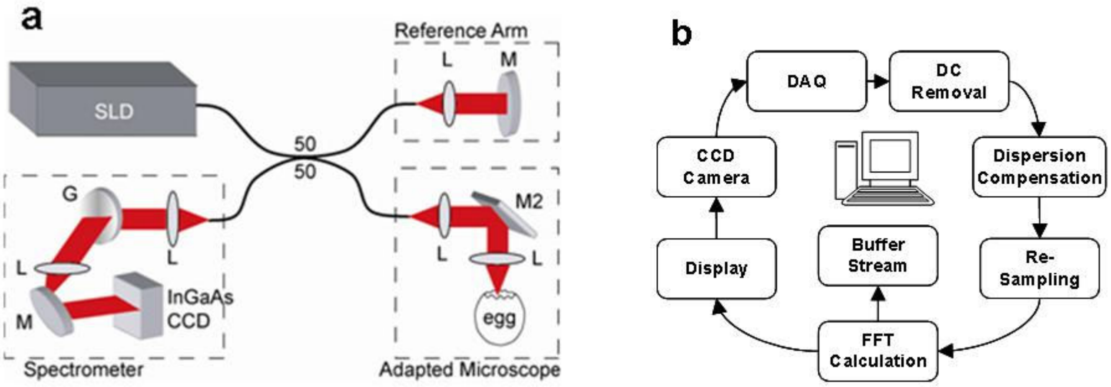

Figure 11: 1310 nm spectral domain OCT schematic and processing steps. (a) Schematic of fiber-based SDOCT system. Light from a superluminescent diode is split into a reference arm and sample arm. Sample arm light is scanned across the sample in two directions. Interferometric signal is measured using a custom-made spectrometer with a 512 pixel InGaAs CCD camera. (b) Processing steps performed by the data acquisition software include DC removal, dispersion compensation, re-sampling the spectrogram from evenly-spaced in wavelength to wavenumber, fast Fourier transform, display, and data archiving. The entire process occurs in real time. This system runs at 18.9 kHz line rate. L, lens; M, mirror; M2, 2-axis scanning mirror; G, grating.

4.2 Design and Methods

4.2.1 SDOCT System Design

In 2003, Yun et. al., demonstrated the first 1310 nm SDOCT system utilizing a 19 kHz linescan CCD camera [S. H. Yun et al., 2003]. The goal for this chapter was to describe our 19 kHz 1310 nm SDOCT system designed for small animal imaging and more specifically for *in vivo* imaging of the chicken embryo heart. A schematic of our SDOCT system and flow chart of the processing steps performed are shown in Figure 11. Figure 11a shows a schematic of our fiber-based SDOCT system. The light source consisted of a super luminescent diode (InPhenix) centered at 1310 nm (Δλ=84 nm full-width half-max). The optical power (appx. 30 mW) was split into the sample and reference arms using a 50/50 fiber optic coupler (AC Photonics). The reference arm consists of a collimator (Thorlabs, Inc.), neutral density filter (not shown), and mirror. The reference arm power is attenuated such that the system is shot noise limited [M. A. Choma et al., 2003]. The optical pathlength of the reference arm is built to match the optical pathlength of the sample arm. Light reflected from the sample is mixed with the back reflected light from the reference arm. As described in Chapter 1.2.1 Spectral-Domain Optical Coherence Tomography, a spectral interferogram is produced by the mixing of the sample and reference arms where the frequency of the interferogram is related to the pathlength distance of the reflectors in the sample. The interferogram is dispersed spectrally using a custom made spectrometer and measured using a CCD linescan camera.

There are three main components to an SDOCT system: 1) SDOCT spectrometer (or "engine"), 2) sample arm ("adapted microscope in Figure 11a), and 3) data acquisition and processing (Figure 11b). In this section I will describe, in detail, the design of our SDOCT spectrometer, two generations of sample arm microscopes, and data processing steps for small animal imaging.

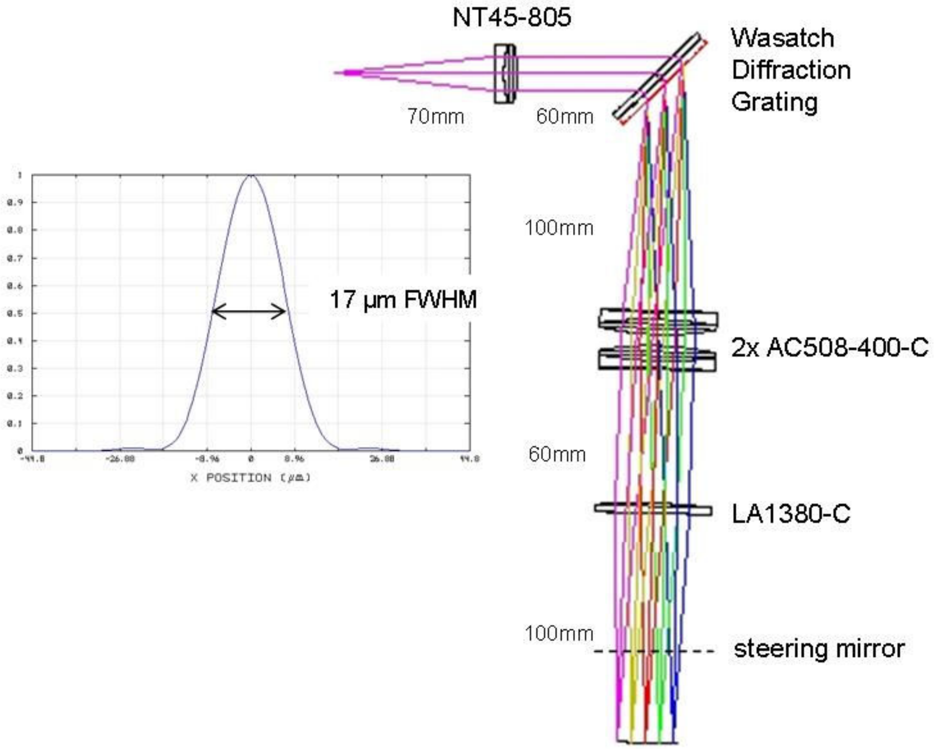

NT45-805
Wasatch Diffraction Grating
70mm
60mm
100mm
2x AC508-400-C
60mm
LA1380-C
100mm
steering mirror
17 µm FWHM
1
0.9
0.8
0.7
0.6
0.5
0.4
0.3
0.2
0.1
0
-44.8
-26.88
-8.96
0
8.96
26.88
44.8
X POSITION (µm)

Figure 12: ZEMAX® design of SDOCT spectrometer with 512 pixel InGaAs CCD camera. Steering mirror is depicted as transmissive in this illustration. Colors represent wavelength range of SLD light. Blue, 1250 nm; green, 1275 nm; red, 1300 nm; olive, 1325 nm; violet, 1350 nm. Inset: PSF of focused spot on CCD detector at central wavelength λ=1300 nm. (design adapted from B. Applegate).

4.2.1.1 InGaAs SDOCT Spectrometer

The optical design for our 1310 nm SDOCT spectrometer (Figure 12) was adapted from Brian Applegate’s (former post-doctoral fellow) original design. The design of this spectrometer was based on optimizing the spectral resolution to maximize imaging depth, as described in Chapter 1.2.4 Imaging Depth. The 19 kHz InGaAs CCD camera has 512 pixels where each pixel is 50 μm wide and 500 μm wide. We wanted to design a spectrometer where the optical spot size is smaller than the pixel dimension so that the signal “falloff” is limited by the CCD camera and not by spectrometer design.

The light from the spectrometer arm of the 50/50 optical coupler was collimated using a 75 mm focal length, 25 mm diameter achromatic doublet (Edmund Optics). This collimating lens was spectrally dispersed using a Wasatch transmissive diffraction grating. Two, 50 mm, 400 mm focal length achromatic doublets (200 mm effective focal length, Thorlabs, Inc.) are used to collimate the spectrally dispersed beam. The spectrally dispersed beams were then focused onto the CCD pixel array using a 50.8 mm diameter plano-convex lens with a 500 mm focal length (Thorlabs, Inc.). For easier steering of the spectrally dispersed beams, I included a 50.8 mm gold coated mirror (PF20-03-M01, Thorlabs, Inc.) between the focusing plano-convex lens and the CCD array. Insertion of the steering mirror enables design of a more compact spectrometer however it should be kept in mind that the spectrum illuminated onto the CCD array is in reverse order (longer wavelengths on the left rather than right); this impacts calibration of the spectrometer for data processing, which will be discussed later in this section. The theoretical focused spot size of the spectral interferogram at center wavelength of 1310 nm is 17 μm FWHM, sufficiently smaller than the 50 μm pixel size. The theoretical spot size at a wavelength of 1260 nm was approximately 25 μm (FWHM). The InGaAs CCD camera had two detection settings, high-sensitivity and high-capacity. The high-sensitivity mode is for best detection and enables readout of the CCD array at maximum speed without sacrificing signal. The high-capacity setting is for greater resolution of weak absorbance peaks. For all of the studies presented in this dissertation, I was interested in high-speed imaging and therefore utilized the high-sensitivity mode.

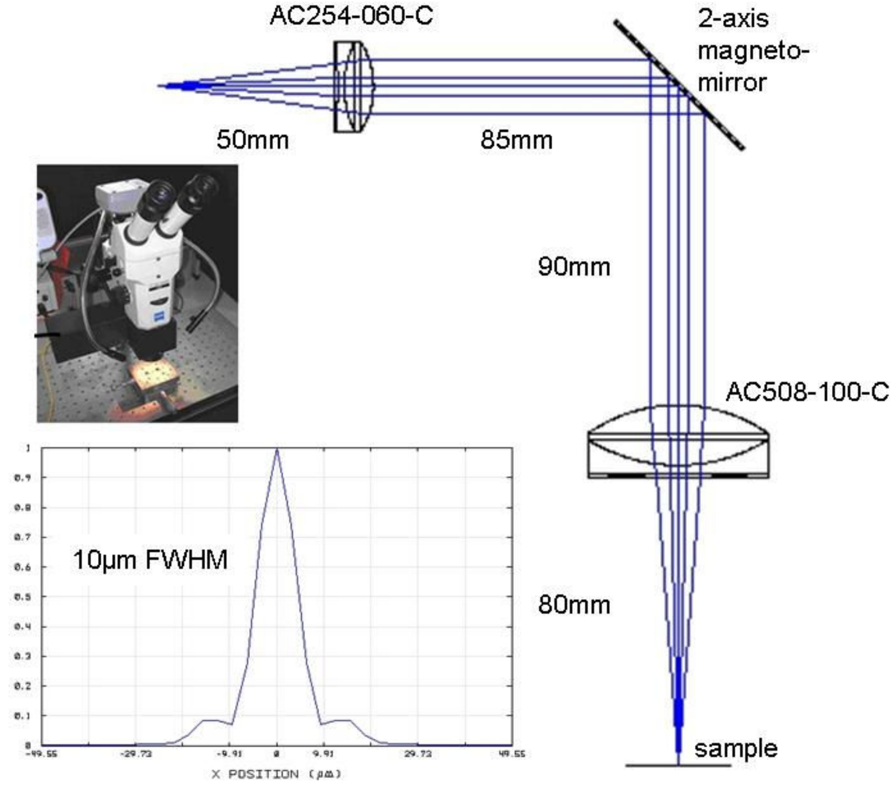
AC254-060-C
2-axis magneto-mirror
50mm
85mm
90mm
AC508-100-C
10µm FWHM
80mm
sample
1
0.9
0.8
0.7
0.6
0.5
0.4
0.3
0.2
0.1
0
-49.55
-29.73
-9.91
0
9.91
29.73
49.55
X POSITION (µm)

Figure 13: Optical design and PSF of SDOCT microscope adapted for collinear imaging with Zeiss microscope. X,Y scanning is performed by software controlled magnetically-steered mirror. Theoretical lateral resolution is 10 µm. Photograph of actual microscope with OCT scanning optics (black box on left side of microscope) is provided. (design by B. Applegate)

4.2.1.2 SDOCT Microscope

The first generation SDOCT microscope for small animal imaging was designed by Brian Applegate. This microscope scanner was designed to be incorporated into a Zeiss stereo-zoom microscope (photo in Figure 13) enabling collinear visible and OCT microscopy. For imaging of small animals the SDOCT microscope needed to be optimized high lateral resolution (<15 µm), long depth of focus (to preserve lateral resolution throughout a certain depth), long working distance (to enable repositioning or manipulation of the sample), and two-dimensional scanning for volumetric OCT imaging. Figure 13 shows the ZEMAX® design of our 1st generation SDOCT microscope which I built. The OCT beam was collimated using 25 mm diameter achromatic doublet with a focal length of 60 mm (Thorlabs, Inc.). The collimated beam was laterally scanned in two dimensions using a magnetically steered mirror (Optics In Motion, LLC). This mirror has an optical aperture of 50 mm and for this optical design could scan up to 9 mm across a sample. The collimated beam was focused onto the sample using a 50.8 mm diameter achromatic doublet with a focal length of 80 mm (Thorlabs, Inc.). The theoretical spot size focused onto the sample was 10 µm (FWHM) at the center of the scan. The microscope design was not optimized for spot sizes at the edges of the scan; therefore the theoretical spot size at 2.5 mm from the center was approximately 20 µm.

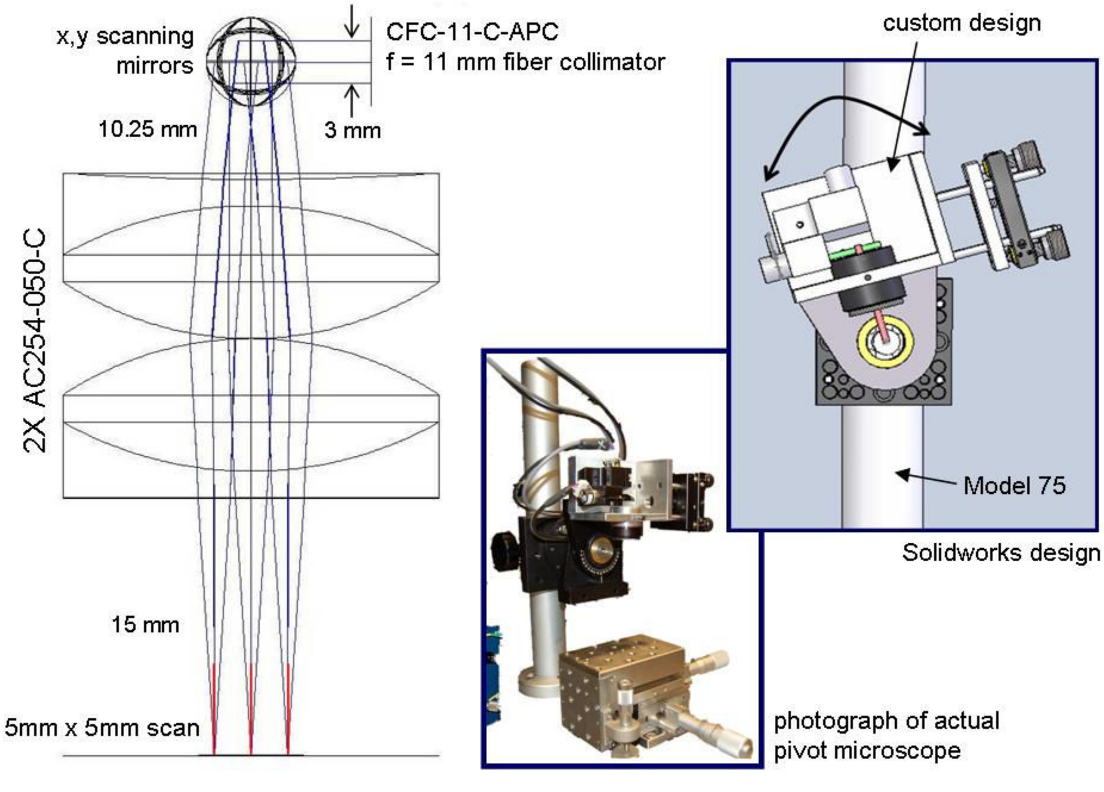
x,y scanning mirrors
CFC-11-C-APC
f = 11 mm fiber collimator
10.25 mm
3 mm
2X AC254-050-C
15 mm
5mm x 5mm scan
custom design
Model 75
Solidworks design
photograph of actual pivot microscope

Figure 14: ZEMAX® optical system design and Solidworks® mounting design of pivoting microscope. X,Y scanning is performed by two galvanometer mirrors. This microscope was specifically designed for *in vivo* chicken embryo heart imaging. The custom made housing for the microscope optics enables the microscope to pivot around the focal point. Photograph of functioning pivot microscope also included. Solidworks® design files are provided in Appendix 1.

4.2.1.3 SDOCT Pivoting Microscope Scanner

Throughout our studies we experience two key limitations to our SDOCT microscope described above. First, although the dual axis magneto-mirror had a large aperture and eliminated the need of a second scanning mirror for two-dimensional scanning, it had a limited scanning rate. Second, one criteria set forth in designing an SDOCT system for *in vivo* imaging of the embryonic chicken heart was to keep the embryo *in ovo*. As a result, optical reflections from the air-yolk interface were very strong. For high-speed imaging using the Sensors Unlimited 19 kHz InGaAs CCD, the CCD camera is set for high-sensitivity imaging. As a result, strong optical reflections caused saturation of the camera. To minimize saturation due to these strong reflections, a common practice is to tilt the sample such that the light reflected from the surface is reflected into a difference direction. This has proven to be very difficult, if not impossible, in the case of *in ovo* imaging because the young embryo floats inside a liquid yolk which constantly maintains a surface perpendicular to the scanning optical beam due to gravity. To address these limitations I designed and built a 2nd generation scanning microscope that pivots around the focal point of the SDOCT optical beam. In addition to enabling higher speed imaging without scanning artifacts and reduction of saturation artifacts, this microscope enables control of the scanning beam angle relative to sample structure and blood flow. The advantage of having the ability to control the scan beam angle will be discussed in Chapter 5.

The challenges in designing the pivoting microscope was to optimize lateral resolution, depth of focus, working distance, and scan length while maintaining a small footprint, telecentricity, and collimated beam within the aperture of the galvanometers (5 mm). Figure 14 shows the optical and mechanical design for our pivoting microscope. A 11 mm focal length fiber collimator (CFC-11-C-APC, Thorlabs, Inc.) was used collimate the sample arm OCT light onto the center of the two scanning 6 mm aperture galvanometers (Model 6210H with x,y mount) which were separated by 9.5 mm. The collimated beam diameter was approximately 3 mm. Two 25.4 mm diameter, 50 mm focal length lenses (effective focal length = 25 mm) were used to focus the collimated light onto the sample. The focused spot was approximately 15 mm away from the back surface of the second focusing beam. This microscope was designed to be telecentric to eliminate differences in optical pathlength between the center and edges of one lateral scan which cause artificial curvatures in an image. A telecentric system has the location of the entrance and exit pupils set to infinity. This means all of the rays are parallel to the optical axis across a lateral scan, as indicated by the red lines in Figure 14. We have designed a telecentric system by having equivalent front and back focal lengths. In the ZEMAX® design, the back focal point is at the first scanning galvanometer mirror. However, in the actual optical set up, I aligned the optics so the back focal plane is between the two scanning mirrors, 4.75 mm in front of the first scanning mirror. This was due to restraints in physical space between the x,y galvanometer mount and lens tube surface. Included in Figure 14 is an illustration and photograph of the pivoting microscope. Using Solidworks® drafting software, I designed the custom mount which enables alignment of the collimated OCT sample beam with the x,y galvanometer mirrors, and focusing optics. The design files for the custom mount are provided in Appendix 1. The mount was attached to a Swivel Mount (LC1A, Thorlabs, Inc.) which I removed the cage plates and attached one of the swivel brackets to a vibration dampening pillar (Model 75, Newport Corp.). The pivoting microscope was designed such that if the optics are aligned as designed in Figure 14, the microscope can pivot over a range of approximately 170 degrees around the focal point, without displacement of the focus position relative to the sample. A 3-axis stage and rotational mount (not in photograph) was used to assist in positioning and alignment of the sample under the microscope.

The point-spread function (PSF) at the focus and spot sizes through defocus are shown in Figure 15. We show that the diffraction limited spot diameter is 12.5 μm (FWHM). This spot size is larger than the diffraction limited spot size for the 1st generation microscope, but still within the desired resolution of 15 μm. Another important consideration is how well the lateral resolution is maintained throughout the imaging depth. The bottom of Figure 15 shows central spot diagrams through the focus of the system. The diagram is for all wavelengths (1250 nm through 1350 nm, indicated by the different colors) at the central scan position (x = 0, y = 0). From this diagram we expect the spot diameter to maintain less than 20 µm throughout a 200 µm depth of focus, which is acceptable for imaging early stages of chicken embryo hearts. We were able to achieve this greater depth of focus by utilizing two 50 mm focal length lenses.

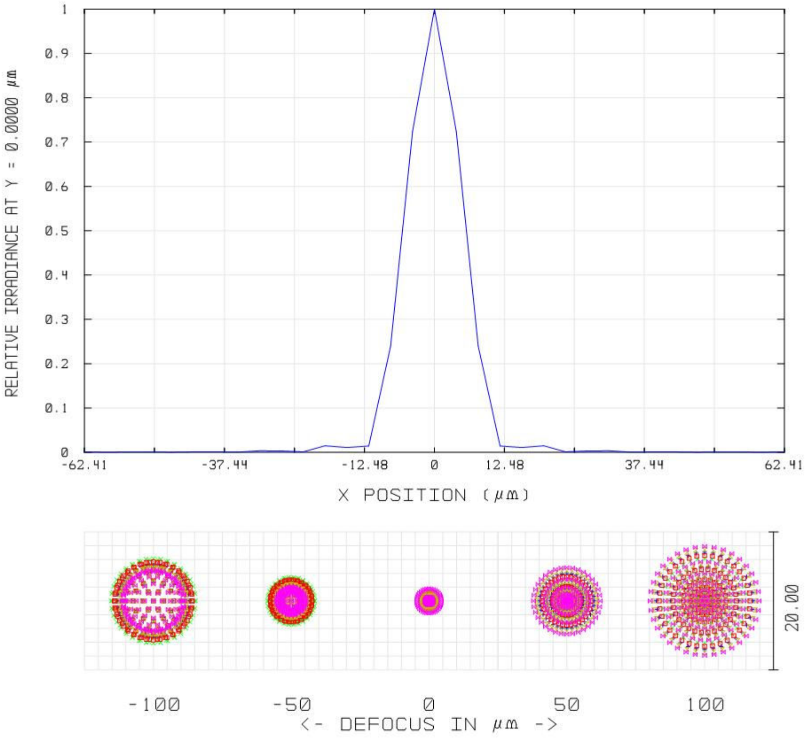

Figure 15: Point spread function and spot diagram through focus for pivoting microscope. The theoretical lateral resolution is less than 20 µm within 200 µm of imaging depth center at the focus.

Figure 16 shows spot diagrams at the focus at nine different scanning positions over a 5 mm by 5 mm area. Although the 5 mm square scan area is smaller than that achieved using the 1st generation OCT microscope, it is sufficient for imaging chicken embryo hearts which grow to less than 1 mm during the developmental stages of our interest. This decrease in scan length is due to limitations in optical design. In order to design an optical system which can scan a greater distance, larger diameter focusing optics would need to be incorporated. Aside from designing expensive, custom-made optics, large diameter, short focal length optics (i.e. high-NA) are not readily available. As described in Chapter 1.2.3 Image Resolution the lateral resolution of our imaging system is dependent on the collimated beam diameter and strength of the focusing optics (i.e. focal length). The aperture of the scanning galvanometers is 6 mm. This means that the collimated beam, reflecting off of the galvanometer mirrors needs to be less than 6 mm in diameter. We have also found that minimizing the spot size on the galvanometer mirrors can reduce phase noise caused by mechanical vibrations of the mirrors. We attempted to design an optical system where the small collimated beam is expanded before focusing on the sample but the footprint of such system was considerably large (greater than 200 mm, or 8 inches), inhibiting the chance of building it on a pivoting mount. As shown in Figure 16, the focused theoretical spot diagrams for most scanning positions (except extreme corners, position x = 5 mm, y = 5 mm) are within the diffraction spot diameter of 12.9 µm. The diffraction spot diameter was determined from the Airy disk calculation in the ZEMAX® model. The different colors represent wavelengths of 1250, 1275, 1300, 1325, and 1350 nm.

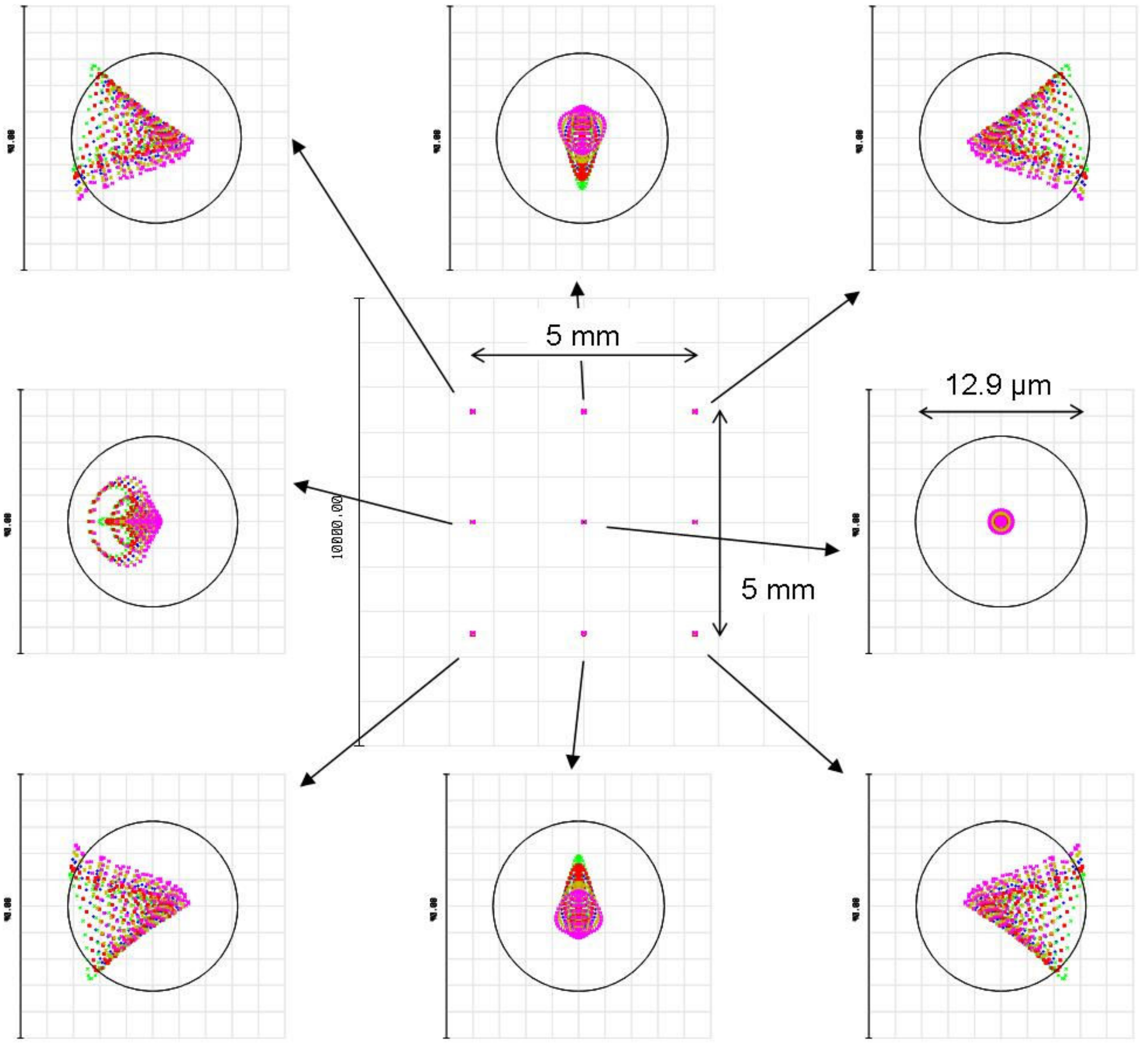

Figure 16: Spot diagrams from nine scan positions of pivoting microscope. 5 mm x 5 mm total scan length (center). 12.9 µm diffraction limited spot size.

4.2.2 SDOCT Data Acquisition and Processing

The SDOCT system was driven by high-performance software that controlled the lateral scanners in the microscope and performed data acquisition, processing, and data archiving in real time. This software was developed in collaboration with Bioptigen, Inc (software version: OCT_r1.2v1200). The flow chart in Figure 11b outlines the processing steps necessary for real-time display of SDOCT images.

4.2.2.1 DC Subtraction

When data acquisition is initiated by the user, collection of the spectrogram is triggered by the CCD camera through a 4-channel, 12-bit, 5 Ms/s/channel data acquisition board (NI-PCI 6110, National Instruments). After buffered acquisition of the user-defined number of lines (per frame), the DC signal (or source spectrum which produces a DC peak) is subtracted using the following steps:

$$\begin{aligned} f_{DC}(z) &= \sum_{i=1}^{numlines} f_i(z) \\ f_i^{'}(z) &= f_i(z) - f_{DC}(z) \end{aligned} \tag{13}$$

where $f(z)$ is the interferometric spectrum detected by the CCD camera and $f_i^{'}(z)$ is the ith DC subtracted line.

4.2.2.2 Dispersion Correction

Dispersion is phase velocity that depends on the frequency (or wavelength) of light. Phase velocities is dependent on the “dispersive” in which material light passes through, such as lenses and optical fibers. In SDOCT we utilize broadband light sources to maximize our axial resolution (Equ. 5). As a consequence we need to address dispersion effects that can occur when the phase velocity of the broadband light passes through different dispersive elements in the sample arm relative to the reference arm. In OCT images dispersion causes structures to appear blurred in the axial direction where the blurring worsens deeper in the sample, due to longer pathlength delays that compound differences in phase velocities. There are two ways to correct dispersion: 1) through optical design, or 2) numerical compensation during data processing. The first method, through optical design, is often the easiest. This method requires that all of the dispersive elements that are in the sample arm are used in the reference arm, including match optical fiber lengths. In an ideal system, if such system was built, there should be zero dispersion effects in the OCT image. In reality, however, it is nearly impossible to perfectly match the two arms. Depending on the optics used in the sample arm, this technique can be expensive (from purchasing 2X of every optic). Also, the sample itself can be dispersive and therefore often cannot be matched in the reference arm. One exception to this is in OCT imaging of the eye; a water cell is sometimes used in the path of the reference arm to match the dispersion induced by the fluid in the eye.

Dispersion compensation in SDOCT has been described, in detail by Wojtkowski, et. al. in 2004 [M. Wojtkowski et al., 2004]. The frequency dependent phase velocity $\phi(\omega)$ can be expressed as the following polynomial:

$$\phi(\omega) = a_0(\omega_0) + a_1(\omega - \omega_0) + a_2(\omega - \omega_0)^2 + a_3(\omega - \omega_0)^3 ... \tag{14}$$

where ω_0 is the center frequency, a_0 is the velocity constant at the center frequency, a_1 is the group velocity constant, a_2 is the group velocity dispersion which represents the variation in group velocity with frequency, and a_3 is third-order dispersion which attributes to asymmetric burring of the OCT PSF [M. Wojtkowski et al., 2004]. While the zeroth, and first order terms do not contribute to pulse broadening, the second, third and any higher-order terms do. Therefore, to compensate for dispersion, the spectral interferogram, detected by the CCD camera, in Equ. 1 is modified to correct for the remaining terms in the expansion, i.e. :

$$\phi(\omega) = -a_2(\omega - \omega_0)^2 - a_3(\omega - \omega_0)^3 ... \tag{15}$$

to balance group velocity dispersion $-a_2$ and higher order frequency dependent dispersion $-a_3$. The specific method by which this dispersion correction process is implemented in the Bioptigen-developed software we used for these studies is proprietary. In use, however, determining optimal values for the dispersion coefficients is an iterative process where values for a_2 and a_3 are determined by optimizing image quality metrics. In practice, this was done by using an attenuated reference reflector (such as a mirror with neutral density filter) for the sample and iteratively adjusting a_2 and a_3 until the width of the correlating A-scan peak is minimized. As mentioned earlier, the greatest impact of dispersion is seen at deeper positions, or greater pathlength differences. Therefore, I would set the reference reflector at a pathlength distance considerably far from DC (i.e. $\Delta z \sim z_{max}$) then adjust a_2 and a_3. The dispersion coefficients I used in all of the studies presented in this dissertation were 1.2×10^{-4} and 1×10^{-6}, respectively. The exceptionally small third-order dispersion coefficient suggests that third-order dispersion was negligible. It should be noted that there are automated methods for optimizing a_2 and a_3 and higher order coefficients [M. Wojtkowski et al., 2004].

4.2.2.3 Re-Sampling and Fast Fourier-Transform

The spectral interferogram measured from our SDOCT spectrometer is a function of wavelength. The Fourier-transform relationship between spectral interferogram and depth-resolved A-scan requires the spectral interferogram to be sampled as a function of wavenumber (inverse wavelengths) or frequency. As a result, the measured spectral interferogram which is evenly sampled over wavelength needs to be re-sampled such that it is evenly sampled in frequency. The most important step in re-sampling the interferogram as a function of frequency is accurately calibrating the SDOCT spectrometer. Several methods are used in calibrating OCT spectrometers including linear interpolation based on center wavelength and two other reference wavelengths or a more accurate method is to use light sources with characteristic spectral peaks. Recently, a technique using Doppler to calibrate an OCT spectrometer was presented (Au: Dirk Faber presented at SPIE Photonics West 2008, unable to locate proceedings) which provided a method for determining the exact wavelengths for each pixel element in the spectrometer. For 1310 nm SDOCT systems, I could not find readily available calibration sources with spectral peaks in the 1300 nm region. Therefore, the spectrometer for my SDOCT system was calibrated based on matching the detected source spectrum to the source spectrum measured using a commercial optical spectrum analyzer (Agilent). Three wavelengths were extracted from the analyzer spectrum, λ_{max} (wavelength with maximum spectral intensity), $+/-\lambda_{50\%}$ and $+/-\lambda_{25\%}$, (wavelengths where the spectral intensity is 50% and 25% of maximum, respectively). Pixels in the SDOCT spectrometer spectrum that correlate to maximum, 50% and 25% intensities are set to the wavelengths determined from the analyzer. From these five calibrated wavelengths I calibrated the wavelength spacing between each pixel. In the software, the starting wavelength of the detected spectrum and the wavelength spacing (*dλ)* between each pixel element was entered. I used a steering mirror in the spectrometer (Figure 12) which reverses the wavelengths onto the CCD array. This was accounted for by inputting the starting wavelength as the longest wavelength detected on the CCD and the wavelength spacing as –*dλ*. Based on that information the spectrum is re-sampled from λ to *k* (wavenumber) using the following conversions:

$$\begin{aligned} k &= \frac{2\pi}{\lambda} \\ dk &= 2\pi \frac{d\lambda}{{\lambda_o}^2} \end{aligned} \tag{16}$$

Where *dk* and *dλ* are the spectral sampling intervals in wavenumber and wavelength, respectively and λ_o is the central wavelength.

Once the spectral interferogram is re-sampled, a fast Fourier-transform (FFT) is performed where the zero frequency (DC) is shifted to the center. The resulting FFT produces an “A-scan” or a plot of optical intensity as a function of depth. As the scanning mirrors in the sample arm scan the OCT beam across a sample, a “B-scan” or 2-D cross-sectional image. OCT images are traditionally displayed as power-spectrum where A-scans are presented as $20 \times \log(FFT)$. The phase information which inherently arises from taking the FFT is used for Doppler calculations and will be discussed in Chapter 5.

4.2.3 System Characterization

The signal-to-noise ratio (SNR) was measured by using an ideal reflector (mirror) in place of the sample. The sample arm reflection was attenuated using a 2.2 neutral density (ND) filter. Reference arm power was attenuated using a variable ND filter until the system was shot noise limited (i.e. dominating contributor of noise is electrical). The measured SNR for this system was 100 dB which was calculated using the following expression:

$$SNR(dB) = 20\left[\log_{10}\left(I \middle/ \sigma_{noise} \right) + 2.2ND\right] \tag{17}$$

where I is the FFT peak intensity and σ_{noise} is the standard deviation of the noise. The standard deviation of the noise is measured by recording the pixel location of the peak. The sample arm is then blocked so the only signal comes from the reference arm and a second A-scan is recorded. The standard deviation of the A-scan from a 20-40 pixel range centered at the previously recorded peak location. This value represents the standard deviation of the noise. The theoretical SNR for this system is 116 dB which was calculated using the following equation:

$$SNR = 10\log\frac{\rho S R_s \Delta t}{2e}, \tag{18}$$

where ρ is the detector responsivity (0.8 A/W), S is the power on the sample (7 mW), R_s is the sample reflectivity (R_s=1), Δt is the CCD integration time, and e is the electron charge (1.6 X 10^{-19} C).

Signal degradation as a function of pathlength difference, called “falloff” in SDOCT is attributed to the combination of the finite size of each CCD pixel and the spectral sampling interval determined by spectrometer optics [S. H. Yun et al., 2003]. The measured falloff of our SDOCT system in Figure 17 shows we get a 50% signal power falloff (-6 dB) at 1.3 mm pathlength difference.

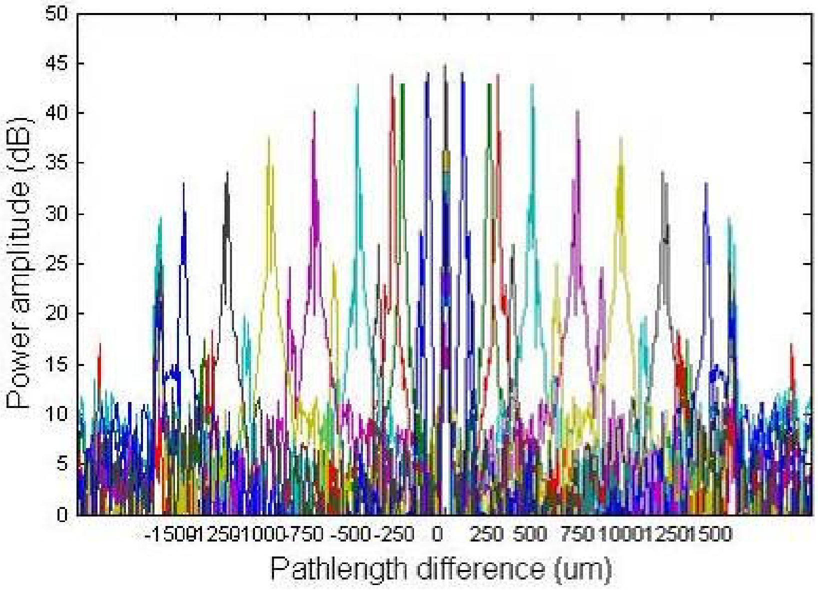

Figure 17: 1310 SDOCT Falloff. This is a plot of signal degradation over increasing pathlength differences. The signal falloff in SDOCT is attributed to the finite size of the CCD pixel and the spectral resolution of the spectrometer. 50% signal loss occurs at approximately 1.3 mm pathlength difference.

The axial resolution is approximately 12 µm which was measured by measuring the FWHM of an A-scan peak from a sample mirror. We measured the lateral resolution using an Air Force resolving power test target (NT55-622, Edmund Optics). Figure 18 contains images of the test target acquired with the pivoting microscope system (Figure 14). Figure 18a and Figure 18b are volume intensity projections (VIP) of the chart taken with the SDOCT system where the test target was placed at the focus of the pivoting microscope. To produce this VIP, a volume dataset was acquired which scans across the test target. Then all of the intensity values were summed over the entire depth. Figure 18b is a higher resolution image from the center target in Figure 18a. It was acquired by increasing the sampling over a smaller scan region. From this VIP, we find that the highest frequency of lines that can be visually resolved is Group 6 Element 1 (Figure 18b, red circle). This target contains 64 line pairs per millimeter which is equivalent to a lateral resolution of 15.6 µm. This value is close to the theoretical lateral resolution of 12.9 µm. Figure 18c contains a microscope image of the test target which was taken by blocking the reference arm and imaging the reflectivity from the pivoting microscope. In this image, the highest frequency of lines that can be visually resolved is Group 6 Element 2 which has 71.8 line pairs per millimeter and is equivalent to a lateral resolution of 13.9 µm. This lateral resolution is very close to the theoretical calculation. Possible reason for the lateral resolution to be lower in the VIP images is that the test target is a glass plate with a highly reflective chromium coating making up the bars. The interferometric fringes from the highly reflective bars become saturated which causes spurious peaks in the A-scan and can blur the image. I would expect if an ND filter was placed in front of the test target when acquiring the VIP images, the resolving power would increase.

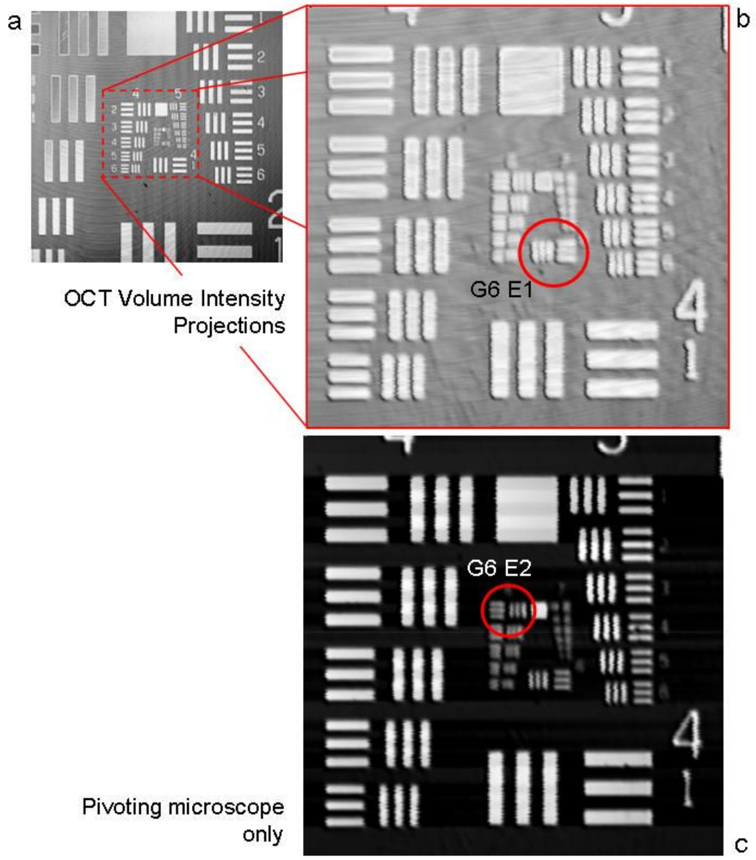

Figure 18: OCT and microscope images of Air Force resolving power test chart. This chart is used to determine the resolving power, or lateral resolution of the imaging system. (a) and (b) are volume intensity projections of OCT volumetric scans of the test chart. (a, red circle) The highest frequency bars resolved by OCT imaging is 64 line pairs/mm or 15.9 µm lateral resolution (Group 6 element 1). (c) Image of same test chart taken from pivoting microscope (reference arm blocked). The microscope resolving power is 71.8 line pairs/mm or 13.9 µm resolution.

Figure 19 demonstrates the volume imaging capability of this system. Here we acquired images from a live Medaka embryo that resides within the chorion of the egg.

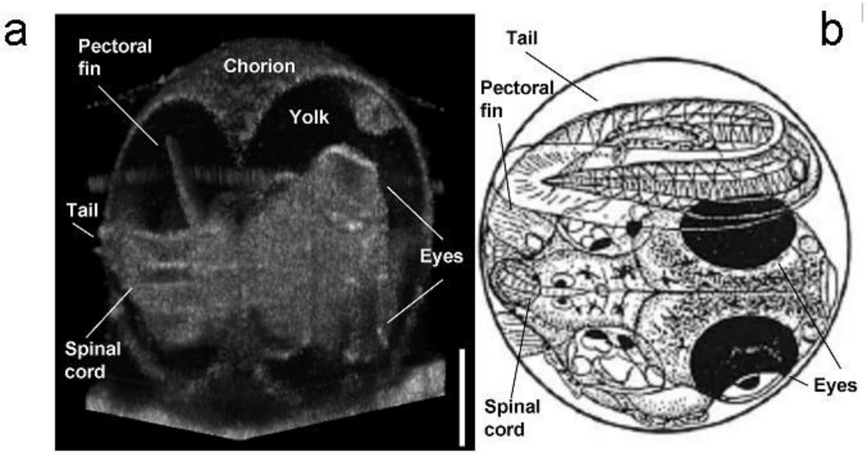

Figure 19: SDOCT volumetric reconstruction of a Stage 38 STII medaka. (a) "cut-away" 3D reconstruction. The tail wraps around the back of the egg and the tip re-emerges near the head. (b) Illustration of Stage 38 medaka. Scale bar: 500 µm. Reconstruction made using 3DView software.

4.2.4 Experimental Methods

This investigation examined chicken embryo heart development between Hamburger Hamilton (HH) stage 9 (30 hrs) to HH 15 (60 hrs) (full development is 21 days, 46 stages) [V. Hamburger and H. L. Hamilton, 1951]. Fertilized Hubert Ross chicken eggs were incubated at 38°C. Part of the shell was removed for optical access to the embryo (Figure 20). After 24 hours of incubation, volumetric images were acquired every three hours. Each imaging session lasted less than 3 minutes to minimize the time the embryo spent outside of the incubator. Between imaging sessions, the eggs were covered with tape, and incubated for further development. Each volume data set consisted of 512 X 256 X 256 pixels and took less than 7 seconds to acquire. Volumetric renderings were made by manual segmentation in three-dimensions using commercial software (Mercury Systems, Inc.).

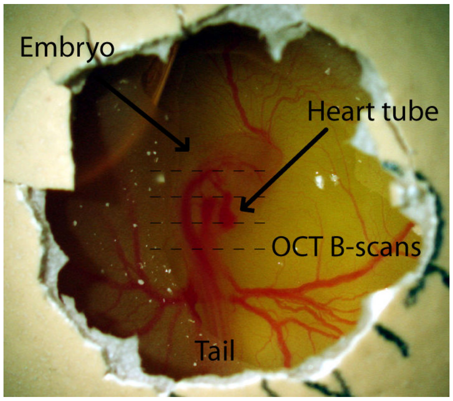

Figure 20: Chick embryo preparation. For OCT imaging, a small window in the outer shell is created for optical access to the embryo. Multiple lateral B-scans are acquired to form a volume dataset

4.3 Results

Three dimensional OCT images were acquired, *in ovo*, from live embryos over development from stage HH 9 to HH 15. This period of development is of primary interest as it covers the initial formation of the embryonic heart tube, through the onset of blood flow, into the looping stage (prior to septation into a four-chambered system). Previously described technologies are unable to adequately image at these stages of development, especially in an *in ovo* setting. Figure 21 contains volumetric images of an embryonic heart at stages HH 9, HH 12, and HH 15.

The three-dimensional OCT reconstructions (Figure 21, 2nd column) are constructed from a stack of 512 cross-sectional B-mode OCT images (Figure 21, 1st column) that were acquired in less than 7 seconds. These reconstructions provide gross inspection of anatomical features and morphology over development. In Figure 21, 3rd column, we show surface renderings of just the heart tube at the three stages of development. These renderings enable visualization of the heart tube without obstruction from other anatomical structures, such as the neural tube. The semitransparent renderings were produced by manual segmentation of the myocardial and endocardial layers of the heart tube wall. The light purple indicates regions between the myocardium and endocardium, which also includes the cardiac jelly. The dark purple is the lumen of the heart tube where blood passes through. The 4th and 5th columns in Figure 21 are representative light microscopy and SEM [J. Männer, 2000] images of excised embryonic chick hearts at the same stages of development.

Here we show at HH 9 (Figure 21, top row) the endocardial tubes have began to fuse into a heart tube starting from the head and continuing caudally. At this stage the heart tube is only a few hundred micrometers in diameter and sits underneath the developing neural tube. The size and location of the forming heart tube, at this stage, prevents other imaging technologies from imaging it, *in vivo*.

In Figure 21, middle row, we show that by stage HH 12 the endocardial tube has fully fused as well as began the looping phase, as evidenced by the bend in the ventricle region. At this point, the heart tube wall has thickened in large part due to the formation of cardiac jelly, an acellular fluid formed by the myocardium. In the volumetric reconstructions, it is evident that the embryo has developed significantly from HH 9 to HH 12. Also at this stage, the embryo as a whole has turned slightly to the side and individual somites can be identified. These are key developmental factors that are used in staging embryos [V. Hamburger and H. L. Hamilton, 1951]. The ability to nondestructively stage embryonic development is one key advantage of OCT in that it enables longitudinal studies in the same embryo.

At HH 15 (Figure 21, bottom row) the heart tube is in the looping stage, bringing the outflow tract and atrial regions of the heart tube closer together. Volumetric imaging will always provide better insight of the shape and size of anatomical features than traditional video microscopy in which only a projection is visualized. As can be seen here, during looping the heart tube has a twisted ‘c’ shape, making volume imaging imperative for accurate visualization of anatomical features relative to each other in the beating heart.

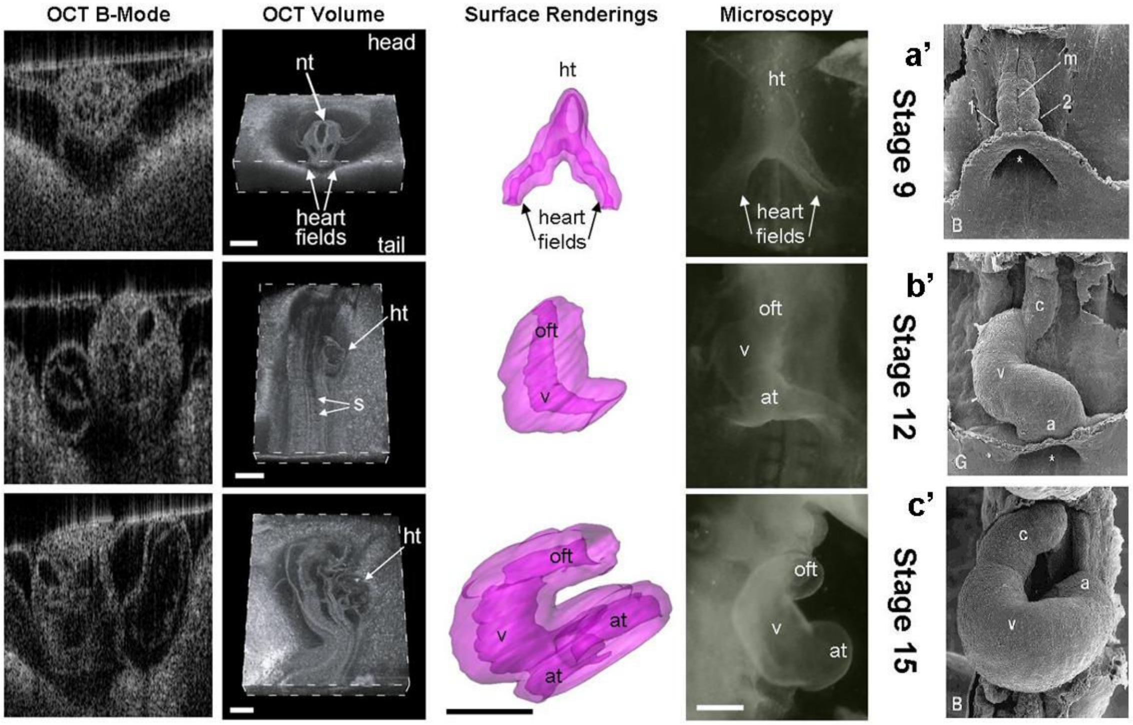
OCT B-Mode
OCT Volume
Surface Renderings
Microscopy
head
nt
heart fields
tail
ht
heart fields
ht
heart fields
a'
Stage 9
m
1
2
*
B
ht
s
oft
v
oft
v
at
b'
Stage 12
c
v
a
G
*
*
ht
oft
v
at
at
oft
v
at
c'
Stage 15
c
a
v
B

Figure 21: Volume images of developing chicken embryo at HH 9 (top row), HH 12 (middle row), and HH 15 (bottom row). SDOCT reconstructions (left column) display the embryo in 3D. Volume datasets were acquired in less than 10 seconds. Semi-transparent surface renderings of the heart (middle column) from SDOCT data show stages of heart development without obstruction of other anatomical features. Dark field microscope images (right column) were taken from representative embryos at or near the same stage of development. (a'), (b'), and (c') SEM images of chick embryo heart at HH 9, HH 12, and HH 15, respectively. nt, neural tube; ht, heart tube; s, somites; oft, outflow tract; v, primitive ventricle; at, atria. SEM images taken from [J. Männer, 2000]. Scale bar = 500 µm.

4.4 Discussion

Chicken embryo development lasts 21 days prior to hatching. Heart formation begins after 24 hours of development (HH 8). Heart fields, which consist of clusters of myocardial precursor cells, coalesce to form left and right endocardial tubes on each side of the neural tube. At HH 9 (Figure 21, top row) the endocardial tubes migrate together and fuse into a heart tube. The fusing processes is completed by HH 11 (40 hours). The heart tube begins to beat at HH 10, at which time early embryonic red blood cells flow through the heart tube.

At HH 12 (Figure 21, middle row) the beating heart tube has fully fused. The heart tube has begun to loop at this stage, as evidenced by the dextral bend in the primitive ventricle. Although difficult to see in the OCT volume reconstruction in Figure 21, middle row second column, it can clearly be visualized using the rendering in Figure 21, middle row third column. At this point, the heart tube wall has thickened in large part due to the formation of endocardial cushions [B. J. Martinsen, 2005], which will ultimately mature into cardiac valves.

At HH 15 the heart tube (Figure 21, bottom row) has continued to loop, bringing the outflow tract (oft) and atrial (at) regions of the heart tube closer together [J. Männer, 2000]. This looping process is necessary for septation to occur later in development. During looping, the heart tube has a cork-screw shape, making volume imaging imperative for accurate visualization of anatomical features relative to each other in the beating heart.

These volume datasets were acquired *in vivo*, producing motion artifacts that affect image quality. At HH 9, the heart tube had just begun to form but had not begun to beat, producing a smooth surface rendering (Figure 21, top row third column). Coordinated contractions began at HH 10 at a rate between 120 to 180 beats per minute. Motion artifacts due to beating did not degenerate single B-mode images, because they were acquired in less than 30 ms. However, volume datasets comprised of multiple B-mode images which were acquired in 7-10 seconds cover 14 – 30 beats and therefore renderings contained ripples (Figure 21 middle and bottom rows third column). Since we were primarily interested in the overall morphology, the motion artifacts in the volume renderings were not a concern. Other groups are developing OCT for quantitative measurement of structural dynamics, and have therefore developed a gated OCT technique [M. W. Jenkins et al., 2006].

4.5 Conclusions

OCT imaging of small animals *in vivo* requires several design considerations which include imaging resolution, imaging speed, and working distance, as described in Chapter 1. Here we have developed a SDOCT system which is capable of real-time acquisition and display of B-mode OCT images at a rate of 18,900 lines per second. We have demonstrated the volumetric imaging capabilities on a live Medaka embryo. Additionally, we have provided, to our knowledge, the first volume images of early heart development taken from the same embryo over several key stages of development. This system will be used in conjunction with Doppler imaging to provide a mechanism for studying blood flow in the embryonic heart.

5. Development of Doppler Optical Coherence Tomography and Spectral Doppler Velocimetry for *In vivo* Quantitative Measurement of Blood Flow Dynamics

Here I describe functional extensions of spectral-domain OCT that I applied for quantitative measurement of blood flow in the chicken embryo heart. These extensions provide a non-invasive technique for visualizing structure while measuring blood flow with spatial resolvability. In this chapter I will describe, in detail, Doppler OCT and spectral Doppler velocimetry and demonstrate these techniques for measuring blood flow dynamics in the chicken embryo.

5.1 Background

Shear stress produced by flow of blood through vasculature is a well known stimulus for gene expression in endothelial cells (for review, see [S. Chien, 2007]). Regulation of genes in the endothelial lining can then alter vascular smooth muscle function [D. G. Harrison et al., 2006]. Shear stress has also been shown to alter cellular identity of mesenchymal stem cells *in vitro* [H. Wang et al., 2005]. Blood flow, therefore, has a powerful influence on cellular expression and identity. It has been shown that blood flow in the early embryonic heart influences the morphology of the developing heart [J. R. Hove et al., 2003; N. T. Ursem et al., 2004]. Abnormal shear stress has also been shown to change expression of genes in the endocardium of the embryo [B. C. Groenendijk et al., 2005]. Alterations in venous return in the chicken embryo caused a reduction in ET-1 (endothelin-1), an endothelial growth hormone and vasoconstrictor. It also caused upregulation of NOS-3 (nitric oxide synthase), a catalysis for generation of nitric oxide (a known vasodilator) as well as KLF2 (Krüppel-like factor) which is known to be expressed in adult human aortas under high shear stress. These results suggest that altered blood flow can cause increased shear stress which then induces changes in endothelial response. Alterations of flow and shear stress induced by venous ligation were not measured directly mainly because technology has not existed that would permit accurate, non-invasive measurements in such small systems at the early stage of development during which the ligature was applied. Micro particle image velocimetry techniques have been used for whole-field velocity measurements in embryonic avian hearts as early as HH 15 [P. Vennemann et al., 2006] and more recently in extra embryonic vessels of an HH 18 chick [J. Y. Lee et al., 2007]. Doppler ultrasound has also recently been reported for non-invasive investigations of atrio-ventricular valve formation in HH 9-39 embryonic chicken hearts [J. T. Butcher et al., 2007], however limitations of spatial resolution limit identification of structural features at stages younger than HH 17 [J. T. Butcher et al., 2007; T. C. McQuinn et al., 2007].

As I have demonstrated in the previous chapter, spectral-domain OCT is well suited for longitudinal imaging of chicken embryo cardiovasculature. A functional extension of OCT, called Doppler OCT can be used to measure Doppler frequency shifts caused by motion or fluid flow [S. Yazdanfar et al., 1997; L. Wang et al., 2004; A. Mariampillai et al., 2007]. Measurements of flow-induced shear rate in capillary tubes have also been demonstrated using Doppler OCT [T. van Leeuwen et al., 1999]. Here we describe an extension of Doppler OCT called “spectral Doppler velocimetry” (SDV) which provides spatially-resolved non-invasive quantitative measurement of blood flow with high temporal resolution. In this Chapter I describe Doppler OCT, the SDV technique, associated challenges, and demonstrate its capability by measuring *in vivo* blood flow through extraembryonic vasculature in the HH 17 chicken embryo. From the SDV measurements I calculate the volumetric flow rate and shear rate from a known location in each vessel. I present blood flow dynamics and spatial velocity profiles from three different vessels in the embryo as well as present Doppler images and SDV measurements of blood flow through the same young embryonic heart tube at two stages of development.

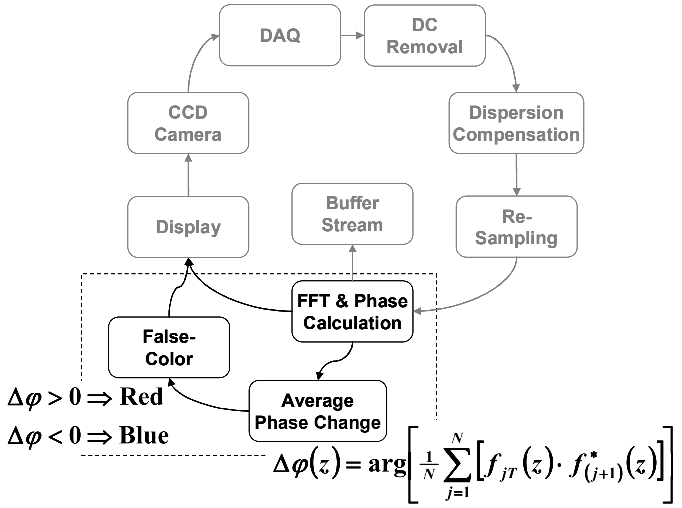
DAQ
DC Removal
CCD Camera
Dispersion Compensation
Display
Buffer Stream
Re-Sampling
FFT & Phase Calculation
False-Color
Average Phase Change
$\Delta\varphi > 0 \Rightarrow$ Red
$\Delta\varphi < 0 \Rightarrow$ Blue
$\Delta\varphi(z) = \arg\left[\frac{1}{N}\sum_{j=1}^{N}\left[f_{jT}(z)\cdot f_{(j+1)}^{*}(z)\right]\right]$

Figure 22: Doppler processing flow chart. Five sequential A-scans are collected at each lateral position. The calculated phase shift corresponds to positive (red) or negative (blue) flow relative to the OCT beam.

5.2 Methods

5.2.1 Doppler OCT Imaging

Doppler imaging is a functional extension of OCT for measurement of flow. In FDOCT implementations, there are no additional hardware requirements necessary for Doppler imaging. The flow chart in Figure 22 includes the additional processing steps which are implemented for Doppler imaging. To measure Doppler frequency shifts, several A-scans are acquired at each lateral position. After performing the FFT, the average phase change, $\langle\Delta\phi(z)\rangle$, over a user defined number of A-scans (*N*) is calculated using the following equation [L. Wang et al., 2004]:

$$\Delta\varphi(z) = \arg\left[\frac{1}{N}\sum_{j=1}^{N}\left[f_j(z)\cdot f_{(j+1)}^{*}(z)\right]\right]. \tag{19}$$

f is the jth A-scan and is a function of axial position, *z*. The Doppler frequency, v_D, is proportional to $\langle\Delta\phi\rangle$ and dependent on the integration time of the CCD camera (*T*). The maximum (v_{max}) and minimum (v_{min}) detectable frequency shifts are given by:

$$\begin{aligned} \nu_D &= \frac{\Delta\varphi}{2\pi T} \\ \Delta\nu_{\max} &= \frac{1}{T} \\ \Delta\nu_{\min} &= \frac{\sigma}{2\pi T} \end{aligned} \tag{20}$$

where σ is the standard deviation of the phase noise, which is dependent upon system SNR [M. A. Choma et al., 2005]. σ is measured in a similar method to measuring noise for calculating SNR. Using an attenuated ideal reflector (such as a mirror) for a sample, the standard deviation of the phase across a range of pixels where the A-scan peak is located is calculated. The maximum detectable frequency occurs when the average phase change is equivalent to 2π. At this point, faster frequencies will undergo phase wrapping, leading to a characteristic ring-like Doppler flow signature in vessels. An example of phase wrapping is shown in Figure 23. For absolute velocity measurements, the angle of flow relative to the OCT scanning beam needs to be known. The velocity (*V*) is then related to the angle by:

$$V = \frac{\nu_D \lambda_o}{2\cos\theta} \tag{21}$$

where *θ* is the angle between the incident light and path of flow and λ_o is the center optical wavelength of the source. The maximum detectable velocity is inversely dependent on the integration time of the detector, as described in Equ. 20. Faster detectors are therefore capable of measuring higher velocity flow profiles before suffering from phase wrapping artifacts. Our SDOCT system is capable of imaging up to 19,000 lines per second, thus 512-line B-mode images are displayed at 38 frames/sec (exceeding video rate). Estimating the flow velocity from five sequential A-scans acquired at the same lateral position (i.e., N=5 in Equ. 19) allows for false-color Doppler flow imaging at 3800 lines/sec, or display of 256-line false-color Doppler images at 7.9 frames/sec (220 inactive lines/frame). The Doppler frequency range ($v_{\min}$ and $v_{\max}$) detectable by our SDOCT system is 21 Hz to 19 kHz and the minimum and maximum detectable velocity range, as a function of angle, based on Equ. 21 is plotted in Figure 24.

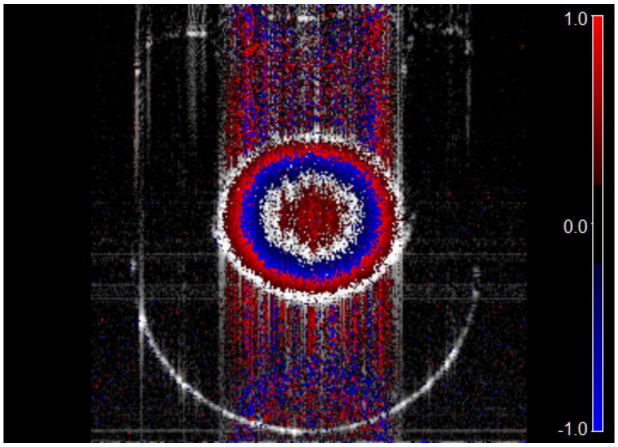

Figure 23: Phase wrapped Doppler image. This example of phase wrapping is from 1% Liposyn pumped through a capillary tube. The wrapped phase is caused by the axial component of the flow velocities being faster than the detection speed of the OCT system. Phase wrapping appears as red-blue rings in the Doppler OCT overlay images.

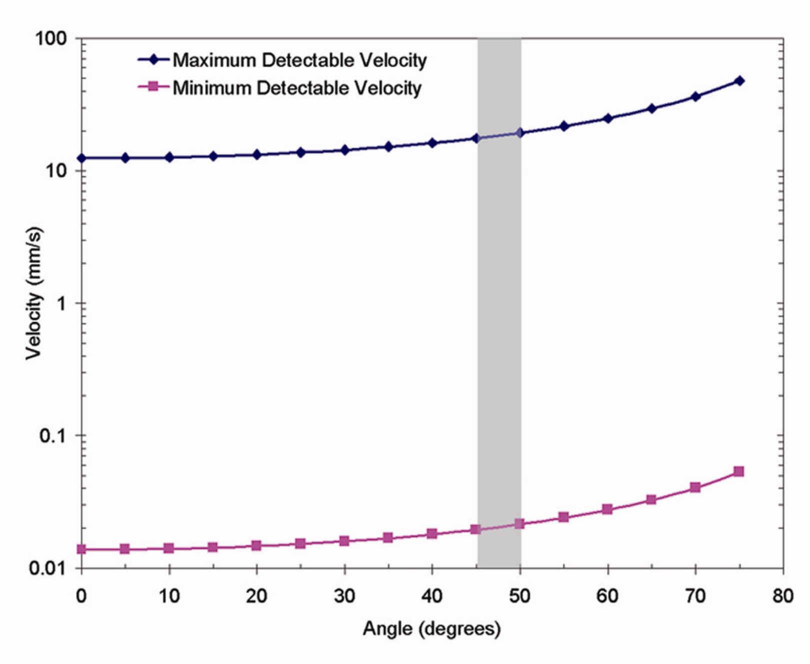

Figure 24: Minimum and maximum detectable velocity range. This plot shows the angular dependency on the minimum and maximum detectable velocities. The range of angles shaded in gray represent the typical flow angles of the extraembryonic vessels relative to the OCT beam using the adapted microscope system. These values were calculated based on Equ. 21.

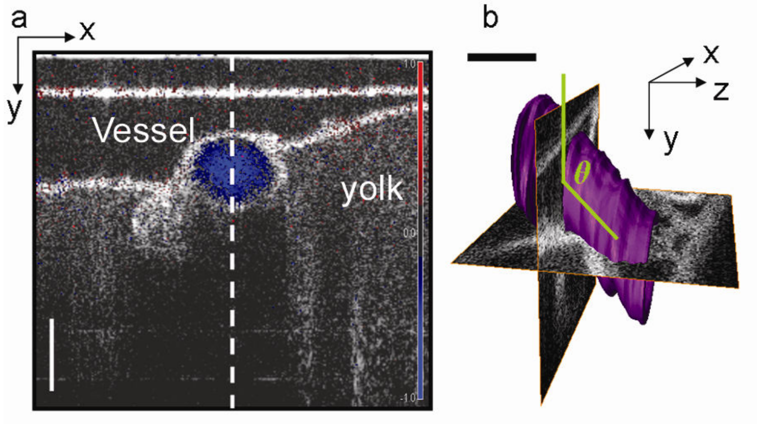

Figure 25: SDV measurement and volume rendering of chicken embryo vessel. (a) Doppler OCT image (blue) superimposed on an SDOCT intensity image of a cross-section of Vessel 2. The vertical dotted line indicates the location where SDV measurements were acquired. (b) 3D volume rendering of Vessel 2. The volume rendering is used to measure the angle of blood flow (green), relative to the OCT scanning beam. Here two orthogonal OCT planes are displayed where the x-y plane corresponds to the image shown in (a). Scale bar = 200 µm.

5.2.2 Spectral Doppler Velocimetry.

SDV is a technique I developed to study flow dynamics at a user-defined spatial location in the sample in conjunction with B-mode Doppler OCT imaging. This technique is analogous to pulsed wave (or spatially gated) Doppler ultrasound which has been used to study blood flow through the embryonic cardiovascular system [C. K. Phoon et al., 2002]. Since SDV stems from Doppler OCT images, an advantage of this technique over pulsed wave Doppler ultrasound is that it is depth-resolved. This means that SDV provides hemodynamic measurement at all depths simultaneously, rather than averaged over a focal volume. SDV is measured by acquiring Doppler M-mode (depth or A-scans vs. time) from a user defined location in the sample at a rapid rate (4.7 kHz). The blood flow velocity is then calculated as a function of time, *V(t)* using Equ. 21.

Accurate quantification of flow velocity cannot be made using a single B-mode image (Figure 25a), unless the vessel is oriented so that the direction of flow lies in the plane of the OCT beam scan (this would be equivalent to the y-z plane in Figure 25b). To measure the angle of flow independent of the orientation of the sample, volume images were also acquired at each SDV location. The volume datasets were manually reconstructed using Amira® software package

(Mercury Systems, Inc.). Then, using the volume renderings, the angle of the center of the vessel lumen relative to the OCT scanning beam was measured (Figure 25b).

5.2.3 Phase Unwrapping

Doppler OCT measurements are constrained by the integration time of the system, where the integration time is set by the readout time of the CCD camera. When flow rates are faster than the integration time, the measured signal becomes phase-wrapped and velocity is not uniquely extractable from the phase. Phase wrapped Doppler OCT images appear to have “rings” of positive (red) and negative (blue) frequency shifts, as is seen in Figure 23. The first attempt we made to address phase wrapping was by low-pass filtering the Doppler measurements to reduce the phase noise and then implementing previously described two-dimensional phase-unwrapping algorithms described in text by Ghiglia, et. al. [D. C. Ghiglia and M. D. Pritt, 1998]. The two-dimensional phase-unwrapping algorithm was implemented by a former undergraduate student, Tzuo Hann Law. The scripts (written for Matlab® programming platform) are provided in Appendix 2. These techniques ended up being very difficult to apply towards our Doppler datasets mostly due to the extreme noisiness of the data and the multiply wrapped phase.

After that time, I developed the a pivoting microscope (Figure 14) described in the previous chapter. Not only did the microscope enable reduction of bright reflections off the yolk surface, it was also designed to take advantage of the angular dependence on the maximum detectable flow velocities (Figure 24). In Equ. 21, the velocity is calculated based only on the axial component of the velocity vector. A microscope which pivots provides user control of the magnitude of the detected axial component. Decreasing the axial component by rotating the OCT scanning beam close to perpendicular to the direction of flow, enables detection of faster velocities.

Figure 26 demonstrates the phase-resolving ability the pivoting microscope provides. In this demonstration, 1% Liposyn was pumped through a 500 μm inner diameter capillary tube at a peak velocity of 75 mm/s. Based on the graph in Figure 24, we predict that the flow angle, relative to the OCT scanning beam needs to be greater than 80 degrees to detect the Doppler frequency shift without suffering from wrapped phase. The two rows in Figure 26 show cross-sectional and lateral images, respectively, of the capillary tube at four different microscope pivot positions. As the capillary tube approaches a position almost perpendicular to the OCT scanning beam, the red-blue rings which indicated wrapped phase disappear.

There are physical limitation in imaging the chicken embryo, *in ovo*. These limitations, such as the shell or other anatomical parts of the embryo, can prevent scanning the OCT beam at any pivot position of choice due to other structures blocking the view. As a result, I found that often the Doppler data could not be completely phase resolved by pivoting the microscope. So, in all Doppler studies taken with the pivoting microscope, I would align the embryo and pivot tilt the scan angle until I knew that the phase was only singly wrapped. Singly wrapped phase appears as only one red-blue ring (Frame 3 in Figure 26). Then the phase profiles were low-pass filtered and then unwrapped using built in Matlab® algorithms, or in the case of noisy phase data, 2π was manually added to wrapped phase values.

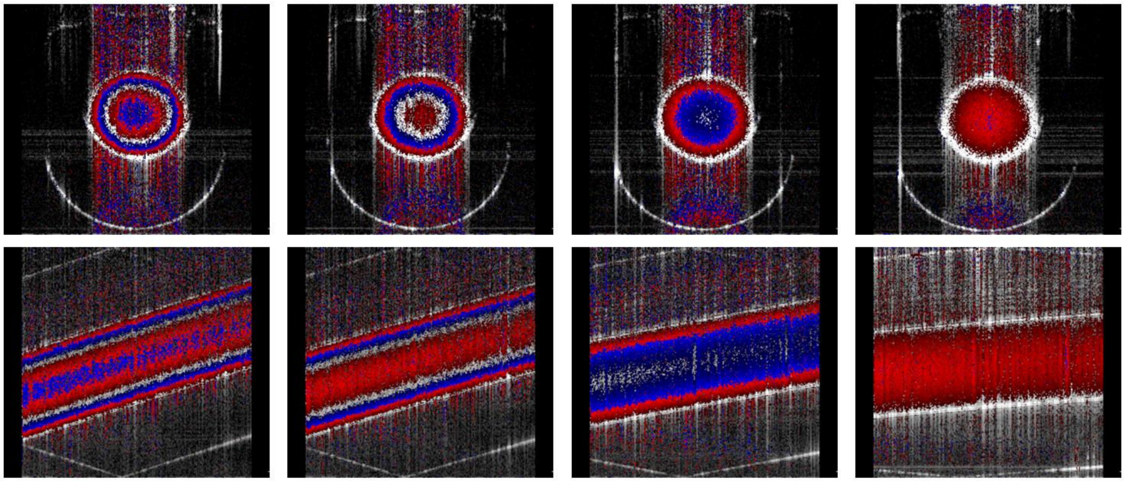

Figure 26: Pivoting scan of flow phantom. This is a series of Doppler OCT images of Liposyn flow through a capillary tube. The top row of images displays the Doppler phase shift in the cross-section of the tube. The bottom row displays a lateral view of the tube to illustrate the changing of the OCT scan beam as the microscope pivots around the focal point. In the last frame, the OCT scan beam is near 90 degrees to the flow which enables resolution of the absolute phase (no rings).

5.2.4 Determining Vessel Diameter, Volumetric Flow Rate, and Shear Rate.

The diameter of the vessels was measured twice, once using structural B-mode (two dimensional) and a second time using structural M-mode (one dimensional) images that were acquired at the same location as SDV measurements. The two diameter measurements were averaged, where the difference between the two measurements for all three vessels was always less than 12 µm. Volumetric flow rate was calculated assuming fully developed laminar flow [J. Y. Lee et al., 2007] and that the vessels and heart tube were cylindrical with a circular cross-section using the following equation:

$$Q = \frac{1}{2}\pi R^2 V_{\max} \tag{22}$$

Where Q is the volumetric flow rate, R is the vessel radius, and V_{max} is the maximum blood flow velocity along the vessel cross-section. The shear rate is defined as [T. van Leeuwen et al., 1999]:

$$\tau = \frac{\partial V}{\partial R} \tag{23}$$

Where τ is the shear rate (s^{-1}) and $\partial V/\partial R$ is the change in blood flow velocity over a known radial distance, adjacent to the vessel wall. $\partial V/\partial R$ was determined by calculating the slope of the velocity rise over 25 µm from the edge of the vessel wall using the spatial velocity profile, at a time in the heartbeat cycle when the blood flow velocity was maximum.

5.2.2 Extraembryonic Vasculature Imaging Experimental Methods

We incubated fertilized Hubert Ross chicken eggs, blunt-end up at 38°C for 72 hours. Staging was determined based on number of hours of incubation, structure of the heart, and shape of the entire embryo [V. Hamburger and H. L. Hamilton, 1951; J. Männer, 2000; B. J. Martinsen, 2005]. At early stages of development, the shape of the embryo changes dramatically. The head turns starting at HH 9 and continues to grow and bend through HH 18. These are the stages of primary interest. Also, during these stages the heart undergoes significant developments from fusing into a tube, to looping. All of these anatomical benchmarks were used to estimate the stage of the embryos. Immediately prior to imaging, a small window was created through the outer shell and chorionic membrane to gain optical access to the live embryo (Figure 27b). The egg was removed from the incubator and Doppler B-mode, SDV measurement and volume datasets were acquired across the three numbered vessels shown in Figure 27b. Each recording session required less than 3 minutes. The egg was placed back in the incubator for 5 minutes between imaging each vessel as a pre-emptive measure to ensure the embryo had a consistent heart rate for each measurement. The heart rate was monitored based on imaging the pulse rate of blood flow through the vessel of interest.

For blood flow imaging through the embryonic heart tube, Hubert Ross chicken eggs were incubated for 48 hours. At that point, the eggs were prepared for imaging as described above. Doppler OCT images and SDV measurements were acquired every three hours for a total of 12 hours. As with the vessel study, a volumetric dataset was acquired with each SDV measurement to enable velocity calculation and pinpoint the location SDV measurements relative to the three-dimensional structure of the heart tube.

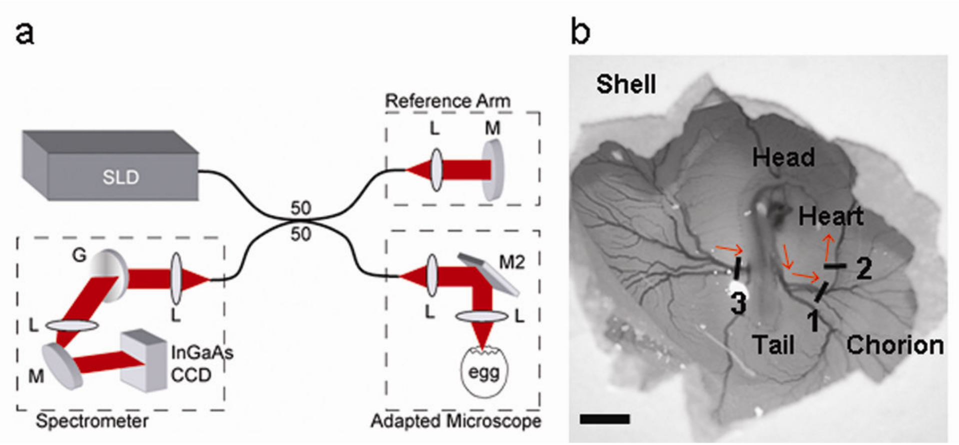

Figure 27: SDOCT setup for extraembryonic vessel imaging. (a) SDOCT system setup. The 1st generation adapted microscope was used for this study. (b) Scanning of the SDOCT beam across three vessels was performed using an adapted Zeiss stereo zoom microscope. Red arrows indicate direction of blood flow. SLD, superluminescent diode (InPhenix); L, lens; M, mirror; M2, dual-axis scanning mirror (Optics in Motion); G, grating (Wasatch). Scale bar = 5 mm.

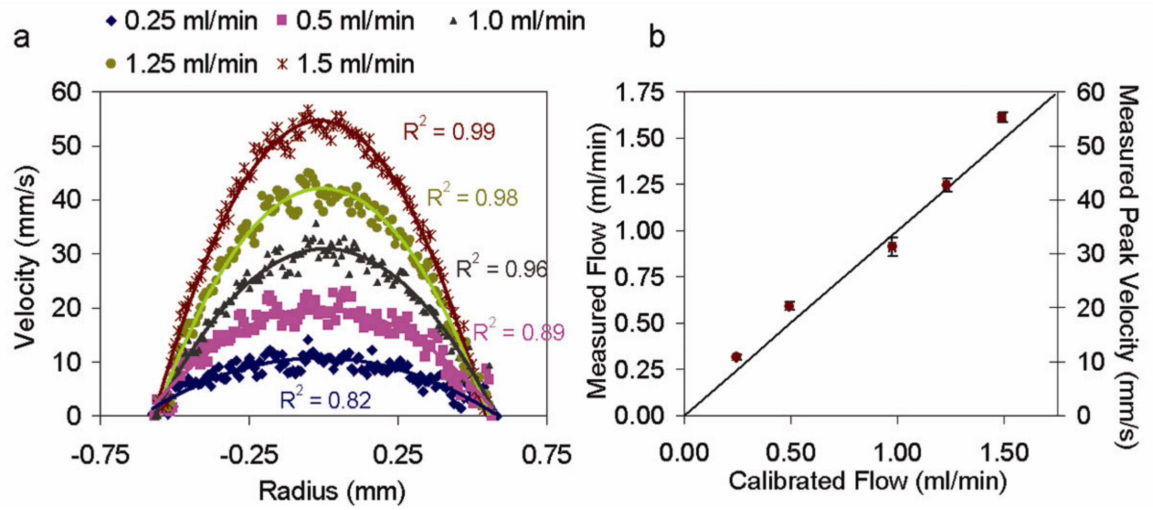

Figure 28: Validation of Doppler flow measurements. Doppler measurements were taken of 10% Liposyn flowing through a 1.2 mm inner diameter capillary tube at rates of 0.25 ml/min, 0.5 ml/min, 1.0 ml/min, 1.25 ml/min and 1.5 ml/min (a) Averaged Doppler velocity profiles (dotted) and corresponding quadratic fit (solid line) at each flow rate. R^2 values are provided for each fit. (b) Comparison of measured and calibrated flow rates.

5.3 Validation

To test the accuracy of velocity and flow measurements using Doppler OCT we measured flow of 10% Liposyn through a 1.2 mm inner diameter glass capillary tube at five different flow rates. The flow rate was controlled using a Harvard Apparatus syringe pump where we varied the flow rate between 0.25 ml/min and 1.5 ml/min. To calculate each flow rate, we plotted the average cross-sectional velocity profile from five Doppler OCT images. A second-order polynomial fit to each averaged profile provided the peak velocity (Vmax) used in Equ. 22. The measured and fitted velocity profiles for each flow rate is shown in Figure 28a. Figure 28b shows a comparison between the measured flow using Doppler OCT and the calibrated flow from the syringe pump. Syringe pump calibration was performed by measuring the volume of fluid which flowed through the system for a given amount of time. For each flow rate, calibration was performed three times. The average flow rates and standard deviations for both the Doppler and calibrated flow measurements are provided (Figure 28b). The vertical standard deviation was calculated between the flow rate averaged from five Doppler OCT images and the flow rate measured using each individual frame. Phase unwrapping algorithms were performed on Doppler OCT measurements at flow rates of 1 ml/min, 1.25 ml/min, and 1.5 ml/min which correspond to peak velocities between 30 mm/s and 55 mm/s.

5.4 Results

5.4.1 Extraembryonic Vasculature Imaging

In vivo Doppler and three-dimensional OCT images were acquired from three blood vessels in an HH 17 chick embryo. Figure 25a contains a normalized color Doppler OCT image of blood flow through the cross-section of Vessel 2 superimposed over a B-mode OCT structural image. The red or blue of the Doppler OCT image corresponds to blood flow in the direction towards or away from the incident OCT beam. The intensity of the grayscale structural image correlates to the reflectivity of the microstructures in the tissue. The dotted line in Figure 25a indicates the A-scan location for SDV measurement. SDV measurements were taken along the center of all three vessels as illustrated in Figure 25a. Figure 25b is a volumetric rendering of Vessel 2 (purple) with display of two orthogonal OCT cross-sectional images. The x-y plane pinpoints the location of the SDV measurement within the 3D vessel structure. This plane is the same as Figure 25a. The angle of flow relative to the OCT beam is measured using similar volume renderings for all three vessels.

Blood flow velocity dynamics and the spatial velocity profile of the three vessels are shown in Figure 29. An example Doppler M-mode (depth – y-axis vs. time – x-axis) image from Vessel 2 is shown in Figure 29a. As in Figure 25a, the normalized color Doppler is superimposed over OCT A-scans collected over time, from the same location in the vessel. A plot of the Doppler measurement from the center of the vessel as a function of time provides information on the blood flow dynamics in the vessel (Figure 29b). Velocity as a function of time in each vessel was calculated using Equ. 21. This plot provides time-resolved velocity measurements of blood flow through Vessel 1 (red), Vessel 2 (green), and Vessel 3 (blue). The initial time for each measurement was arbitrarily chosen at a point when the velocity was near zero. These plots show the increase in velocity as blood passes through the SDV line of interrogation. Peak velocities were approximately 3.1, 2.0, and 8.0 mm/s for Vessel 1, Vessel 2, and Vessel 3, respectively; and the velocity drops to zero at times correlating to diastole. The blood velocity rates are on the order of those measured using micro particle image velocimetry [J. Y. Lee et al., 2007]. These results are also consistent with the expectation that peak blood flow velocities decrease in peripheral vessels further downstream from the heart. In the vitelline vessel (Vessel 3), a major blood vessel that connects to the dorsal aorta, we measured velocity flow rates over 2.5 times faster than the other two, more peripheral vessels. In each case there is also a small decrease in velocity that occurs during peak flow. This transient decrease in flow may represent the dicrotic notch and wave that is observed in post-embryonic peripheral arteries [M. Troxler and D. Wilkinson, 2007] (see discussion).

As previously mentioned, an inherent advantage of SDV over pulsed wave Doppler ultrasound is the ability to acquire depth resolved velocity measurements. A plot of the blood flow velocity through the diameter of each vessel is shown in Figure 29c. These velocity profiles were sampled at a time near peak flow through the vessels (t = ~110 ms for Vessel 1 and 2, t = ~145 ms for Vessel 3).

One challenge in resolving the blood flow profiles is that the high optical attenuation of blood reduces optical contrast in OCT images. This is best demonstrated in Figure 25a, where a “shadow” appears below the blood vessel. This shadow can also add additional phase noise to Doppler images in the same region. As a result, accurately measuring blood flow in vessels that are large or reside deeper in tissue may prove difficult. The asymmetry of the blood flow profile from Vessel 3 was most likely caused by optical attenuation near the bottom of the vessel. The shear rate on the vessel wall was based solely on the ascending slope of the velocity profile. The calculated shear rates for Vessels 1, 2, and 3 were 54.2, 74.5, and 25 s^{-1}, respectively. The table in Figure 29 outlines the measured diameter and volumetric flow rate from each vessel. This investigation of extraembryonic vessels was necessary to develop the technology for interpreting flow through the more complex and dynamically beating heart tube.

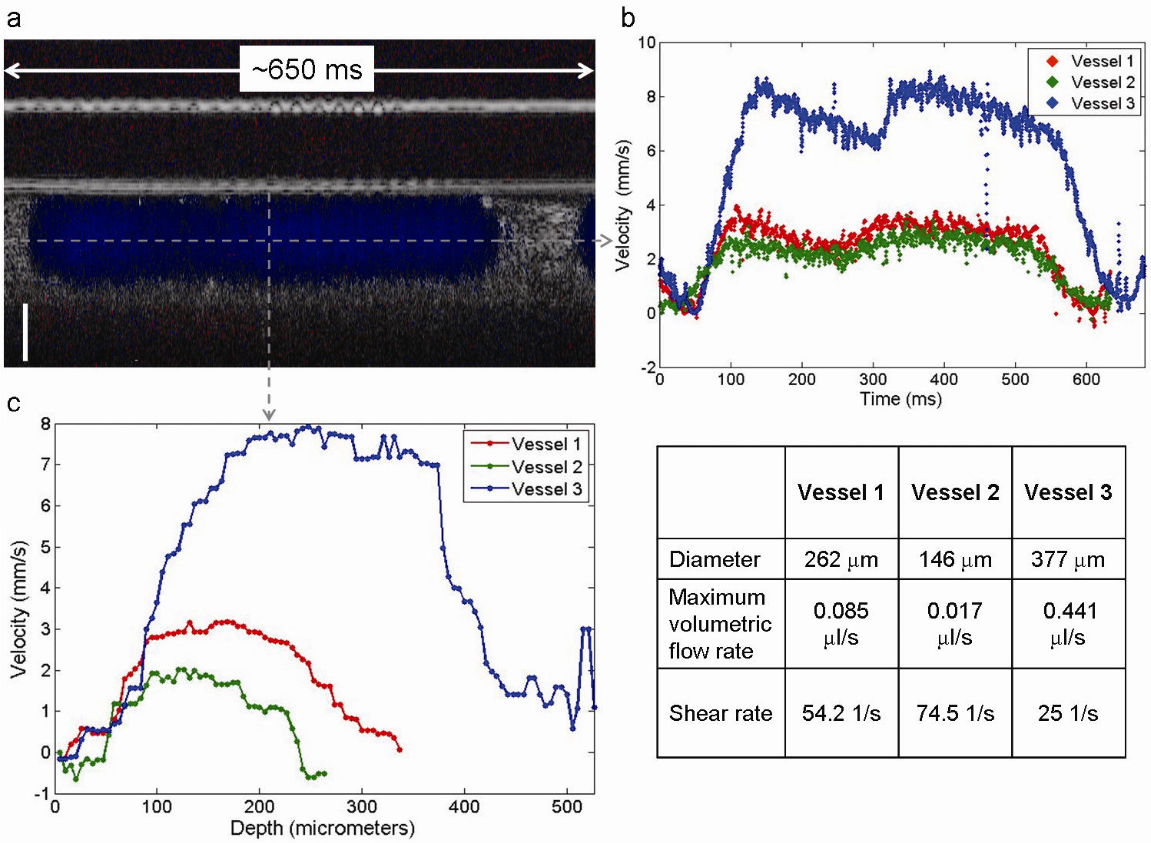

	Vessel 1	Vessel 2	Vessel 3
Diameter	262 μm	146 μm	377 μm
Maximum volumetric flow rate	0.085 μl/s	0.017 μl/s	0.441 μl/s
Shear rate	54.2 1/s	74.5 1/s	25 1/s

Figure 29: Blood flow measurements from three extraembryonic vessels. (a) Depth (y-axis) vs. time (x-axis) Doppler M-mode (blue) superimposed over M-mode OCT scans of Vessel 2. (b) SDV measurement taken along the dotted horizontal line in (a) shows the blood flow velocity dynamics as a function of time for all three vessels (Vessel 1-red, Vessel 2-green, Vessel 3-blue). (c) Velocity profile along the dotted vertical line in (a) for all three vessels. (table) Measured diameter, volumetric flow and shear rates for all three vessels. Scale bar = 100 μm.

A series of Doppler OCT images of blood flow through the primitive ventricle of the heart tube at stages HH 11 and HH 14, are shown in Figure 30. As is standard in color Doppler ultrasound, false-color Doppler OCT images (red/blue) are superimposed on SDOCT intensity images (grayscale); this imaging mode is performed in real-time. Blood flow begins near stage 10 of development, therefore these images were acquired during the very first hours of blood flow development. From these cross sectional views, the myocardium and endocardium are easily resolved. Blood flows from the primitive ventricle out of the heart tube through the outflow tract (dotted arrow). Then by HH 14 (Figure 30b) the Doppler OCT images reveal the continued development of the embryonic heart tube. At the end of the outflow tract, the endocardial cushions have begun to form. These cushions are the precursors to the aortic valves and are believed to have significant influence on the mechanism of blood flow [L. A. Taber et al., 2007].

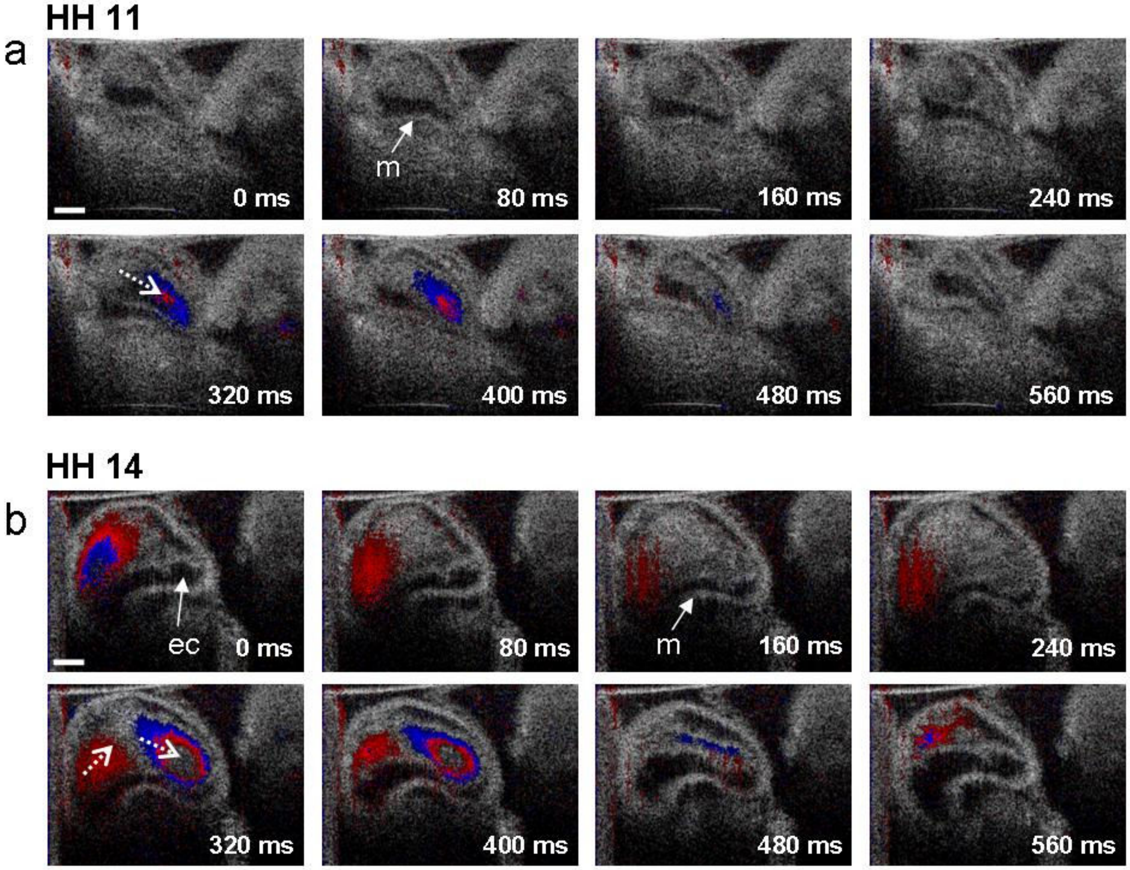

Figure 30: Doppler OCT time series of blood flow through chicken embryo heart tube at HH 11 and HH 14. Endocardial cushions have not begun to form at HH 11. Doppler OCT B-mode images (red/blue) are superimposed on SDOCT images of the primitive ventricle and outflow tract. The red-blue rings are artifacts caused by phase wrapping. Dotted arrows show direction of flow. m, myocardium; ec, endocardial cushion. Scale bar = 250 μm.

To correlate blood flow dynamics with heart development, we acquired volumetric, Doppler, and SDV measurements from the outflow tract at the same stages. Figure 31 contains volumetric renderings and SDV measurements from these two stages of development. The volume renderings (Figure 31a and e) show that at HH 11 the heart tube began to bend in the ventricle region, indicating the initial phase of the looping process. By HH 14, the heart tube bulged towards the right in a later phase of looping. Along with providing identification of structural stage, these renderings are used to measure the flow angle and calculating blood flow velocity using Equ. 21. SDV measurements (velocity vs. depth vs. time) and M-mode (depth or A-scan vs. time) are simultaneously acquired along the dotted yellow line through the center of the outflow tract shown in Figure 31b and Figure 31f. The combination of SDV measurements (Figure 31c and Figure 31g) and M-mode (Figure 31d and Figure 31h) enable correlation of blood flow with expansion and dilation of the outflow tract. At both stages, the bulk of the out flow occurred as the diameter of the outflow tract decreased (grey dotted lines), indicating that the region under observation was actively moving the blood by local contraction. This is consistent with a peristaltic model of pumping by the chick heart [L. A. Taber et al., 2007]. Following contraction, the outflow tract expanded with nearly no net blood flow (blue dotted lines), due to the region filling with blood almost equally from flanking regions toward both the inflow and outflow. There was a difference between HH 11 and HH 14 stages of development. At HH 11 outflow shows a definite backflow as the region fills (Figure 31c, red arrow). The backflow may be related to the undeveloped endocardial cushions (valve precursors) at HH 11, allowing rapid regurgitation of blood into the outflow region. At the later stage the blood being regurgitated is less due to beginning development of the cushions and is apparently matched by the forward flowing blood from the inflow region, since there is little net blood flow during expansion of the heart tube.

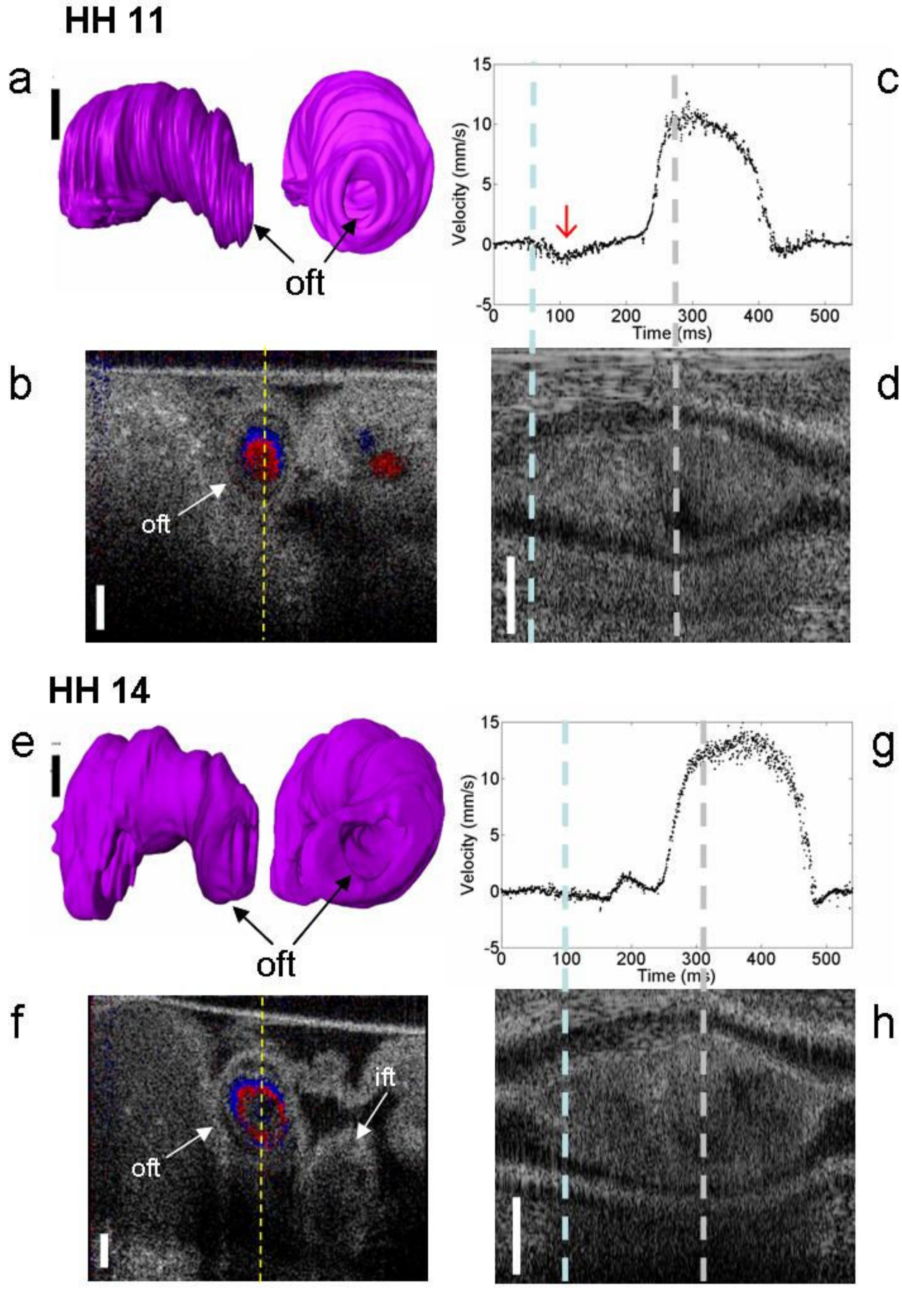
HH 11
a
oft
c
Velocity (mm/s)
15
10
5
0
-5
0
100
200
300
400
500
Time (ms)
b
oft
d
HH 14
e
oft
g
Velocity (mm/s)
15
10
5
0
-5
0
100
200
300
400
500
Time (ms)
f
oft
ift
h

Figure 31: Spectral Doppler velocimetry measurements from the outflow tract (oft) at HH 11 and HH 14. (a) and (f) show volume renderings of the heart tube at HH 11 and HH 14, respectively. (b) and (g) are B-mode Doppler OCT images of blood flow out of the oft (flow coming out of the plane). SDV measurements were acquired along the yellow dotted line. It is evident the heart tube is in midst of looping at HH 14 as evidenced by the U-shape rendering in (e) and the appearance of the inflow tract (ift) in (f). (c) and (g) show blood flow velocity dynamics from HH 11 and HH 14, respectively. The red arrow highlights decreased regurgitation over development. (d) and (h) show M-mode Doppler OCT images where the vertical axis is depth and the horizontal is time. Scale bar = 250 µm.

5.5 Discussion

Cardiovascular development is a dynamic process. Relationships between blood flow, gene expression, and structural morphology in these small vessels and the early heart tube has remained open for investigation, largely because technology that could measure blood flow with spatial and temporal resolution sufficient for early embryonic development has been limited. But it is precisely at these early stages of development that considerable cardiac defects may occur as a result of aberrant flow or structural development. Advancements in ultrasound biomicroscopy can now provide resolution as low as 28 μm axially and 60 μm laterally [D. Sedmera et al., 1999; C. K. Phoon and D. H. Turnbull, 2003]. This technology enables visualization of the heart tube in embryos as young as HH 12 and pulsed Doppler ultrasound measurements in embryos as young as HH 17 [T. C. McQuinn et al., 2007]. To fully understand the relationship between blood flow, shear rate and cardiovascular development, it is desirable to measure blood flow at earlier stages of cardiovascular development, where the vessel lumen can be are as small as 100 μm in diameter. Here we described a technique for non-invasive acquisition of spatially resolved blood flow dynamics in embryonic vasculature using spectral Doppler velocimetry. The high resolution also minimizes artifacts that may occur from averaging over focal volumes that cross areas of vessel wall or animal motion. Such low-velocity movements may cause underestimation of actual blood flow in the developing cardiovasculature. An additional advantage of this system is that SDV permits depth resolved velocity measurements. Shear rate, therefore, can be determined by calculating the velocity gradient near the vessel wall.

A transient decrease in velocity occurred during forward flow in the peripheral vessels (Figure 29b). This may represent the dicrotic notch and wave that is seen in normal human peripheral blood flow measurements [M. Troxler and D. Wilkinson, 2007]. The dicrotic notch in humans represents the closure of the aortic valve and the transient decrease in velocity associated with this. The dicrotic wave represents reflected flow from distal vasculature. The transient dip in velocity we observed may reflect closure of the outflow tract cushion at end-systole.

To correlate flow through the heart tube in relation to the heart tube itself, we utilized Doppler M-mode imaging (Figure 31d and h). These images are acquired simultaneously with SDV measurements providing direct correlation of flow with the heart tube diameter. This permits a higher temporal resolution through a single region than would ordinarily be possible. The peak blood flow velocity only slightly increased over the two stages of development, from 11 mm/s to 14 mm/s. These measurements are within the range of 14.3 mm/s to 30 mm/s reported using laser Doppler velocimetry [N. Hu and E. B. Clark, 1989], micro-particle image velocimetry [P. Vennemann et al., 2006], and pulsed Doppler ultrasound [J. T. Butcher et al., 2007; T. C. McQuinn et al., 2007]. These reported measurements were taken in embryos between HH 12 [N. Hu and E. B. Clark, 1989] and HH 24 [T. C. McQuinn et al., 2007].

Accurate quantification of blood flow velocity in embryonic cardiovasculature using OCT is confronted with several challenges. The maximum detectable velocity is dependent on the integration time of the OCT system. In this case, flow rates which induce Doppler frequency shifts greater than 19 kHz will suffer from phase-wrapping artifacts and thus require implementation of phase unwrapping algorithms. When measuring blood flow in large vessels, these algorithms are sometimes complicated by attenuation of the OCT signal deeper in the vessel, resulting in inaccurate reconstruction of the blood flow profile. This limitation can be resolved by utilizing faster OCT systems or adjusting the OCT scan angle which will then increase the maximum detectable velocity (Equ. 21). The presence of the endocardial cushions insures that the inner surface of the heart tube is not cylindrical, as assumed here. This may produce an overestimation of volumetric flow rates. Here we have also assumed that flow is laminar. This assumption is acceptable for measurement in extraembryonic vessels [J. Y. Lee et al., 2007]. Improved computational analyses are being developed and applied to overcome these limitations, including more recent work on developing a more general expression for volumetric flow [Y. Wang et al., 2007].

The relationship between blood flow and heart development is not completely understood, primarily due to the inability to simultaneously image heart structure and quantitatively measure blood flow with high spatial resolution early in embryogenesis. Spectral Doppler velocimetry, in conjunction with spectral-domain optical coherence tomography provides a new set of tools for non-invasively imaging and quantification of blood flow dynamics in embryonic cardiovasculature. This technology enables spatial mapping of blood flow profiles and associated shear rates that will soon be applied to studies during the earliest stages of cardiogenesis. These measurements can also be used to support and validate computational models already established to estimate the dynamic blood flow related processes that occur during embryonic development [L. A. Taber et al., 2007].

6. Application of Spectral-Domain Optical Coherence Tomography and Spectral Doppler Velocimetry to the Study of Blood Flow in the Embryonic Heart Tube

The goal of this project was to developing OCT for applications in developmental biology. My motivation comes from the need for a noninvasive imaging modality that is capable of imaging the chicken embryo heart as well as measure blood flow. Here I will describe how I used this system and functional extensions for studying blood flow in the embryonic heart tube.

6.1 Background

The relationship between fluid dynamics and cardiac structure at the earliest stages of mammalian heart development is unknown, however studies in older or non-mammalian embryonic hearts suggest a close correlation [N. Hu and E. B. Clark, 1989; T. Ishiwata et al., 2003; A. S. Forouhar et al., 2006; A. deAlmeida et al., 2007]. Wall shear stress induced by blood flow is also known to influence gene and protein expression in the mature cardiovascular system (see review [R. S. Reneman et al., 2006]). In studying embryonic heart development, researchers have also found a link between blood flow and the structural development. A study using zebra fish embryos demonstrated that when flow at either the cardiac inflow or outflow tracts is occluded, the heart develops an abnormal 3rd chamber and had diminished looping and impaired valve formation [J. R. Hove et al., 2003]. Artificially altered flow in the chick embryo has led to changes in shear stress responsive and other endothelial gene expression [B. C. Groenendijk et al.] as well as cardiovascular deformations after septation [B. Hogers et al., 1999]. Although these studies provide insight in the relationship between blood flow and development, a more fundamental questions still needs to be answered, “what is the mechanism that creates the flow of blood in the pre-chambered, pre-valve embryonic heart tube?”

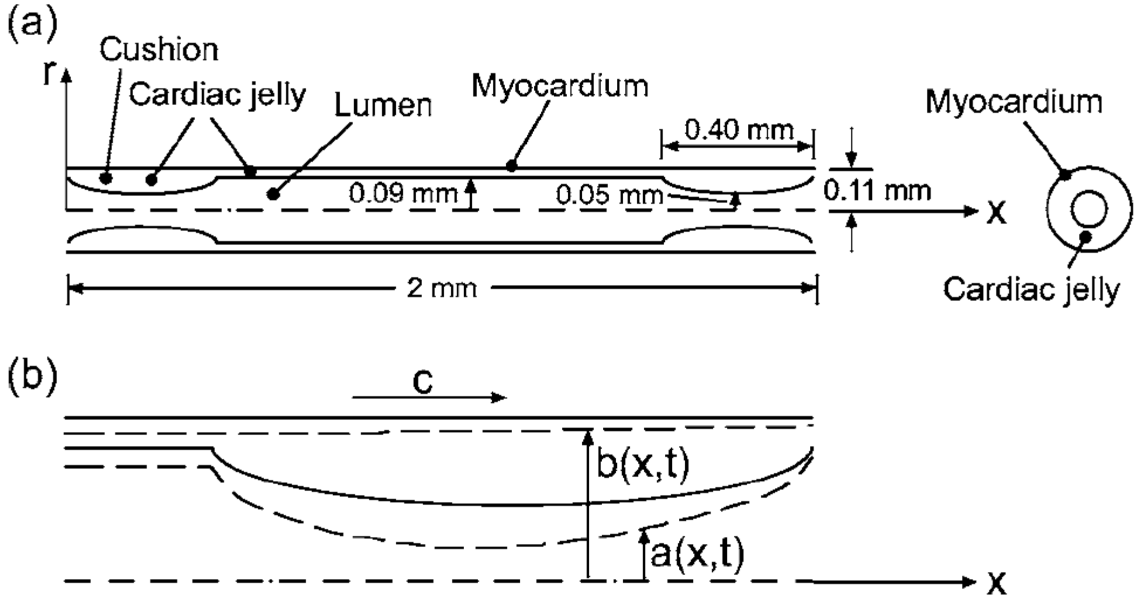

Figure 32: Geometry for finite element model (a) Model dimensions in passive state. Cross section from cushion region is shown at right. (b) Undeformed model (solid lines) and deformed model (dashed lines) near endocardial cushion as contractile wave passes through outflow region. Note the thickening of the cushion as the wave passes.

6.1.2 Mechanism of Blood Flow in the Early Embryonic Heart Tube

The mechanism of blood flow in the early embryonic heart has been something of interest dating back to the 1920's. Early anatomists and developmental biologists have been interested in understanding not only the mechanism of blood flow but the functional significance of certain anatomical structures within in the heart tube. In 1948 Barry rationalized that the early embryonic chicken heart tube could only pump blood by a "peristatoid type contraction" [A. Barry, 1948].

Recently, Taber, et. al. published work on modeling the mechanics of blood flow through the embryonic chick heart tube [L. A. Taber et al., 2007]. Using finite element modeling, velocity dynamics were calculated through a model of an embryonic chick heart tube as a contractile wave travels down the length of the tube. In this work, the chicken embryo heart tube was modeled as a tube with finite length and consisted of 3 layers: a thin outer layer of myocardium, a thicker middle later of extracellular matrix called cardiac jelly, and a thin inner layer of endocardium (see Figure 32). At each end of the tube, an axially symmetric elliptical mound is added to the cardiac jelly which causes the endocardium to extend into the lumen of the heart tube (Figure 32b). The mounds are used to simulate the presence of endocardial cushions.

Using finite element software, the heart tube is dynamically deformed to simulate a contractile wave traveling along the length of the tube. The shape of the wave has the following form (see Figure 34d for example):

$$f(x,t) = \left\{ \begin{array}{l} \sin^2 \dfrac{\pi}{\lambda}\left[x - ct + n(\lambda + \Delta) + \lambda\right], \\ \qquad ct + n(\lambda + \Delta) - \lambda \leq x \leq ct + n(\lambda + \Delta) \\ 0, \quad other\ x \end{array} \right\} \tag{24}$$

where λ is the wavelength of the contractile wave, Δ is the distance between waves, *c* is the wave speed and the period is $T = (\lambda + \Delta)/c$. The myocardial radius (*b*) deforms by

$$b(x,t) = b_o\left[1 - \varepsilon f(x - ct)\right] \tag{25}$$

where b_o is the undeformed outer radius and ε is the maximum fractional decrease in the myocardial radius. With the cardiac jelly being incompressible, the heart tube lumen radius (*a*) will deform by

$$a(x,t) = \left[b^2(x,t) = b_o^2 + a_o^2(x)\right]^{1/2} \tag{26}$$

where $a_o(x)$ is the undeformed lumen radius.

During the simulation, the incompressible Navier-Stokes equation is solved for axisymmetric flow. The general form of this equation is as follows

$$\frac{1}{r}\frac{\partial}{\partial r}(ru_r) + \frac{\partial u_x}{\partial x} = 0 \tag{27}$$

where u_r is the radial velocity which will change as Equ. 26 deforms and u_x is the axial velocity.

At discrete points in time and positions along the heart tube, Equ. 27 is solved for the axial velocity $u_r(x, r, t)$. The volumetric flow rate (Q) and pressure (p) is then directly calculated from the axial velocity using the following equations

$$Q(x,t) = 2\pi \int_0^a u(x,t,r) r dr \tag{28}$$

and

$$p(x,t) = RQ(x,t) \tag{29}$$

where the pressure is set to zero at the inflow and is assumed to pump against a vascular resistance, *R*, along the rest of the tube. It is important to note that in these simulations the pressure is directly determined from the velocity calculations and are simply proportional to the volumetric flow rate. Furthermore, one potentially significant limitation in this model is that it ignores elasticity of the heart tube walls. We expect that the omission of this parameter will not drastically change the dynamic velocity profiles but rather either underestimate or overestimate absolute velocity values. For further details on the finite element simulation, boundary conditions, and validation of this model, see [L. A. Taber et al., 2007]. To my knowledge, this is the first work that has been conducted towards analytically modeling blood flow through the embryonic heart tube. What makes this so important is that this model incorporates a unique anatomical feature of the heart tube, the endocardial cushions.

Endocardial cushions are the developmental precursors to the mature heart valves and septa. Increased production of cardiac jelly at the inflow and outflow regions of the heart tube begin just after the heart tube starts to loop (HH 12) [A. D. Person et al., 2005]. At this stage, the cardiac jelly is primarily composed of extracellular matrix. From that point on, the endocardial cushions continue to develop in size. At HH 17-18, mesenchymal cells begin to infiltrate the cushions [B. M. Patten et al., 1948]. After mesenchymal cells populate the cushions, a series of events occur which lead to the formation of valvular structures and septation of the mature heart. Endocardial cushions are of great interest because even at the beginning stages of development they appear to function as premature valves.

By incorporating endocardial cushions in their finite element model, Taber, et. al. unveil three unique characteristics in the velocity dynamics through the heart tube. First, the centerline velocity dynamics at the inflow, center, and outflow regions of the heart tube have distinctly different profiles. Opening of the inflow cushions causes negative flow, or flow in the backward direction, whereas the opening of the outflow cushions causes rapid forward flow of blood. Second, a secondary flow peak follows the primary peak at or near the location of the outflow cushions. The second peak was observed when contraction of the endocardial cushions caused a rapid decrease in lumen radius. This secondary peak was therefore not observed towards the center of the heart tube, where there are no cushions. The last observation, which contradicts peristalsis in a simple straight tube, is that peak blood flow velocities exceed the contractile wave velocity. According to the Taber et. al. simulations, the increase in blood flow velocities over contractile wave velocity can only occur in a tube that geometrically narrows at the ends, such as a heart tube with cushions.

Although these simulations provide a better understanding of the relationship between blood flow and heart tube structure, there are several simplifications that were made. These simplifications include modeling a straight tube, axisymmetric cushions as well as omission of elasticity of the heart tube wall. However, with any new model, these predicted velocity profiles need to be experimentally validated.

6.1.3 Hypothesis

I aim to use the instrumentation I have developed in Chapters 4 and 5 to perform quantitative tests on hypotheses generated by Taber et. al.'s a finite element model which treats the developing heart as a modified peristaltic pump. More specifically I will test the following hypotheses:

1) center line velocity dynamics between inflow, center, and outflow regions of the heart tube have distinctly different forward and backward flow characteristics relative to the contractile wave location,

2) a secondary flow peak following the primary peak occurs only at the locations of the outflow cushions, and

3) peak blood flow velocities exceed the contractile wave speed.

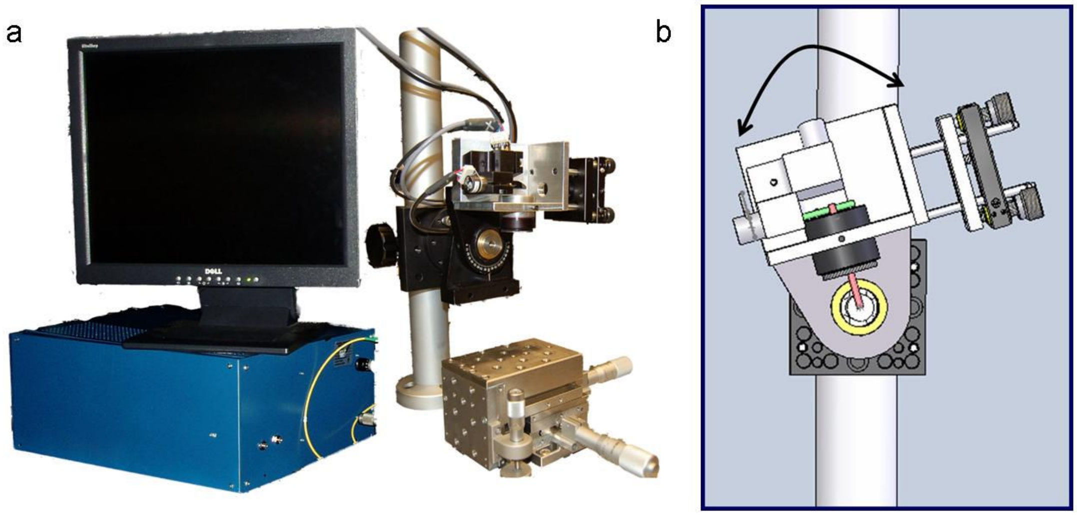

Figure 33: SDOCT system with pivoting microscope arm. (a) Photo of SDOCT system. The SDOCT engine resides inside the blue box. The sample arm optics are contained within the custom made microscope on the right. (b) Illustration of pivoting microscope. The microscope consists of x-y galvanometers for two dimensional scanning and rotates about the focal point axis.

6.2 Methods

For this study we incubated Hubert Ross chicken eggs for between 54 and 58 hours, corresponding to stages HH 15 – HH 17. At this stage, the endocardial cushions are developing and the heart tube is in the looping process. A total of 12 embryos were imaged multiple times at different locations in the heart tube. At each imaging session volumetric and SDV measurements were acquired in the heart tube using the 1310 nm spectral domain OCT engine described in Chapters 4 and 5. To show reproducibility of these results, I compiled velocity plots acquired in similar locations in the heart tube from several embryos of the same age (based on hours of incubation). Several processing steps were performed to correlation between measurements. The velocity profiles were first normalized in magnitude. The main reason for this was because a few datasets could not be volume rendered (missing volume datasets) and therefore the absolute velocity could not be extracted. However, the Doppler frequency plots, which directly stem from the SDV datasets, are proportional to velocity (Equ. 21), and can be used for qualitative comparisons of waveforms. Due to finite computer buffer size, a maximum of 1.5 seconds worth of SDV measurements can be acquired. This means that depending on the heart rate, between 2 to 4 heart beats were collected over that time. To normalize the plots over time, I roughly extracted a single heart beat from each SDV dataset, where t=0 when V=0. Each extracted heart beat was then interpolated such that they contained the same number of elements and then cross correlated using built in Matlab® cross-correlation function. My intention was to align the peak of all of the datasets by determining how much each extracted dataset should be shifted (in time). Through an iterative process, the extracted plots were shifted until the cross-correlation was maximized (see Appendix 3 for the Matlab® algorithm).

In this chapter, I compare SDV measurements to finite element simulations of blood flow through a modeled heart tube. All references to simulated data is work conducted by Taber [L. A. Taber et al., 2007]. I have worked with Taber in associating his simulations with the SDV measurements presented in this dissertation. With this collaboration Taber has provided raw data that was produced in [L. A. Taber et al., 2007], as requested. Input parameters into these simulations and references from which these parameters were extracted are outlined in Table 2. Note, the heart tube geometry was based on rough measurements Taber made in his group. These dimensions strongly depend on the stage of the embryo. These measurements are different than actual heart tube dimensions in embryo studied in this dissertation, I found that the heart tube, at the stages I studied, were between 1.2 mm and 1.7 mm in length compared to 2.0 mm used in the simulations. The undeformed myocardium radius was more than double of the model; between 0.210 mm and 0.45 mm compared to 0.11 mm. Likewise, the undeformed lumen radius in the center of the tube ranged between 0.190 mm and 0.24 mm. These differences in geometries can contribute to differences in the velocity measurements compared to the simulations. The cushions could not be definitely viewed in the OCT images and therefore I could not compare actual geometries to those used in the model.

Table 2: Finite element simulation parameters

Heart Tube Geometryŧ	
Length, L	2 mm
Undeformed myocardium radius	0.11 mm
Undeformed lumen radius in center of heart tube	0.09 mm
Undeformed lumen radius at thickest part of cushions	0.05 mm
Length of cushions	0.4 mm
Simulation Parameters	
Wave speed, c* [F. de Jong et al., 1992]	8 mm/s
Fractional decrease in myocardial radius, $\varepsilon^{\#}$ [L. A. Taber et al., 1994; P. W. Alford and L. A. Taber, 2003]	0.1
Wavelength, λ	1.6 mm
Wave spacing, Δ	2 mm
Mechanical Properties	
Blood density, ρ	1 g/cm^3
Blood viscosity, μ	3×10^{-3} Pa s
Vascular resistance, R [N. Hu and E. B. Clark, 1989]	2×10^{12} Pa s/m^3

ŧ Based on measurements conducted by Taber [Internal communication with Taber].

* Based on speed of electrical depolarization wave at HH 13 – HH 14.

# Based on measured myocardial strains at HH 12 – HH 16

6.3 Results

6.3.1 Center line velocity dynamics between inflow, center, and outflow regions of the heart tube have distinct forward and backward flow characteristics relative to the contractile wave location

SDV measurements were first acquired at different locations along a single chick embryo heart tube. Here I will provide a detailed description of the measured velocity dynamics from the inflow, center, and outflow regions of the heart tube. These measurements were compared to simulations of velocity dynamics at representative locations in the heart tube using Taber's finite element model.

6.3.1.1 Inflow Blood Velocity Dynamics

Figure 34 shows a comparison between SDV measurements acquired near the inflow tract (Figure 34a and b) and finite element calculations of blood flow velocity (Figure 34d, pink line) at the inflow region of the heart tube. Figure 34c contains a volumetric surface rendering of the embryonic heart tube. The grayscale cross-sectional image is a B-mode OCT image taken at the exact location where SDV measurements were acquired. A plot of the outer radius of the modeled heart tube as it dynamically changes when the contractile wave passes the inflow tract is the blue line shown in Figure 34d. For comparison, an M-mode image (Figure 34a) which was acquired simultaneous with the SDV measurements (Figure 34b) provides similar visualization of the heart tube diameter as it changes during the heartbeat cycle.

At initiation of contraction the inflow region closes (Figure 34a and b, red line), and the contraction pushes blood in both forward and backwards directions. The concept of this action is similar to pressing a finger down onto the middle of a tube; however, the outflow portion of the heart tube is open, but the lumen is narrowed, due to the presence of the cushions. This creates a large resistance to flow. On the other hand, the vascular resistance upstream from the inflow is less because the veins are very compliant. As a result of the large resistance in the outflow region and the low resistance upstream from the inflow region, net blood flow was in the backwards direction. At the same time, by closing the inflow region, the contraction increases the pressure inside the rest of the heart tube, due to the combination of decreased tube volume and outflow resistance. When the contractile wave moves toward the center of the tube (Figure 34a and b, green line), the inflow cushions begin to open. Venous blood will slowly fill into the opening area of the inflow tract. This causes a small forward flow as indicated by the blue line in Figure 34a and b. While the inflow tract is completely open (Figure 34a and b, between blue and yellow lines), there is low forward flow due to the continued movement of the contractile wave towards the outflow region. Near the end of the beat cycle, blood flow into inflow region rapidly increases when the outflow region begins to close (Figure 34a and b, yellow line). When contractile wave closes the outflow cushions, the change in closing volume rapidly increases. This rapid decrease in volume forces blood out of the heart tube. This rapid ejection of blood plus the low forward flow of blood due to the movement of the contractile wave results in rapid forward flow into the inflow region (Figure 34a and b, purple line)

The finite element calculations for centerline velocity at the inflow region of the heart tube (Figure 34d) predicted the same characteristic peaks measured in Figure 34b. The pink plot is the calculated center line velocity and the blue plot shows the outer tube (myocardium) radius, indicating the timing of the approach of the contractile wave. Blood flows in the backward direction when the contractile wave begins to close the inflow tract (Figure 34d, red line) and returns to zero velocity when the contractile wave passes the inflow region (Figure 34d, green line). Small forward flow of blood occurs at a time when the inflow tract is almost completely open (Figure 34d, blue line) and flow maintains low forward velocity as the contractile wave travels down the tube. When the contractile wave approaches the outflow cushions (Figure 34d, yellow line), the inflow region of the heart sees a rapid increase in forward blood flow.

Based on the finite element simulations and calculation of center line velocity, the pressure along the heart tube was also calculated using Equ. 29. The calculation for pressure along the entire heart tube, at several time points is shown in Figure 34e. Figure 34e' contains the same pressure calculations on an expanded scale at the inflow region of the heart tube. From $t = 0.22$ to $t = 0.28$, the contractile wave passed through the inflow tract and the regional pressure is higher than the inflow tract but decreases to near 0 Pa (Figure 34e', royal blue and pink lines, respectively). This decrease in local pressure is accompanied by the reduction of backflow through the inflow tract (Figure 34d, green line). Then, when the contractile wave has completely passed the inflow tract and is in the center of the tube ($0.5 < t > 0.7$), the pressure between the cushions decreases to lower than the inflow region with blood flowing in the forward direction (Figure 34d, yellow line). Finally, when the contractile wave reaches the outflow tract ($t = 0.7$), peak blood flow in the inflow tract is reached, and the pressure in the heart tube increases from being negative, resulting in the inflow blood velocity dropping back to zero.

To date, I have successfully performed measurement from the inflow once. Collecting SDV measurements from the inflow region is difficult. When the heart tube is in the looping stages, it first bends into a horseshoe shape that is on its side, where one end is the inflow and the other end the outflow. The inflow part of the horseshoe tube sits below the outflow such that blood flow up (towards the surface) and out. The inflow region lies deeper inside the egg and often cannot be clearly viewed using OCT, due to signal falloff. In the embryo presented here, the heart tube was conveniently close to the surface enabling visualization of both the inflow and outflow portions of the tube.

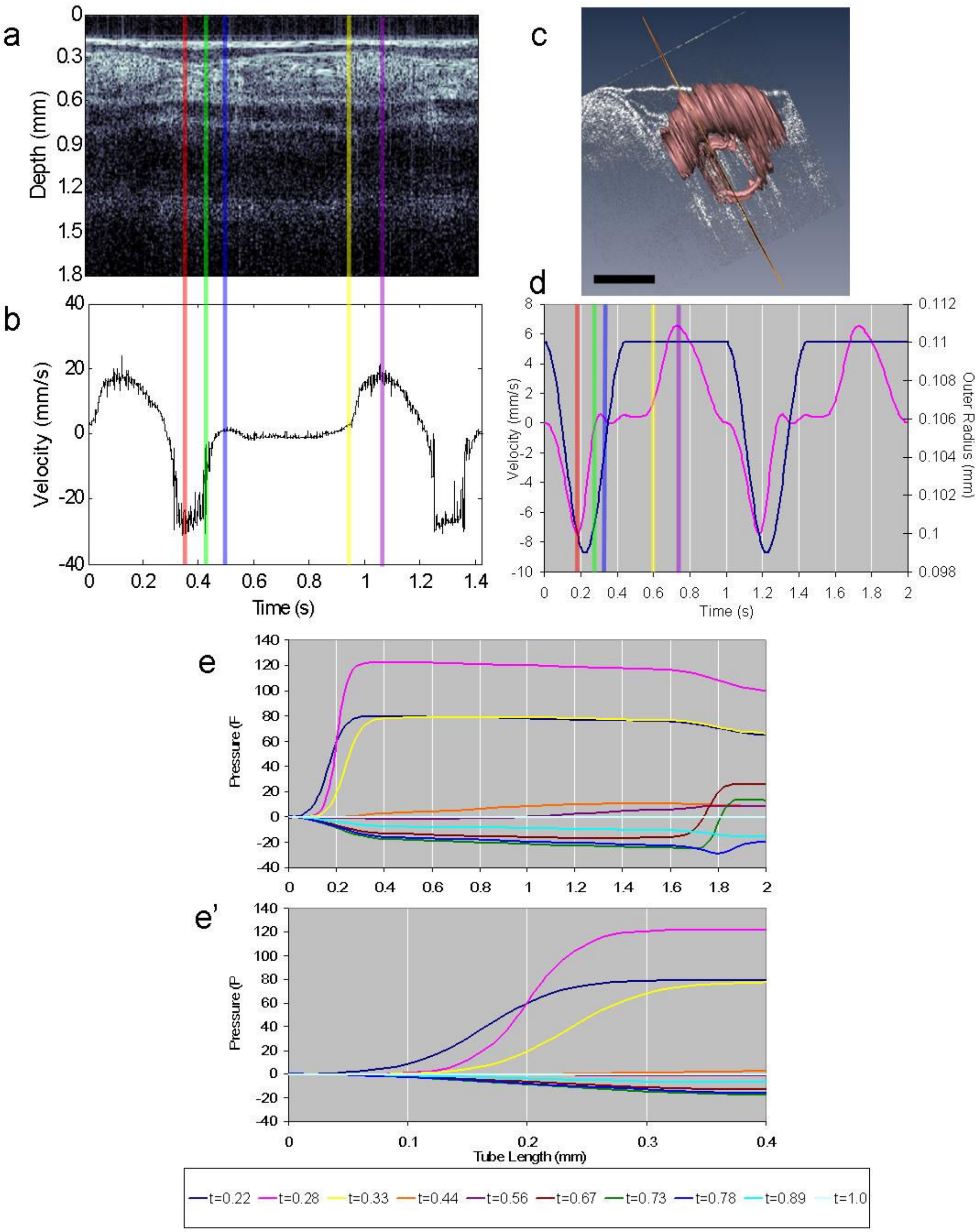

Figure 34: SDV and finite element modeling from inflow tract. (a) and (b) M-mode and SDV measurements. (c) Volume rendering of heart tube containing cross-sectional slice where SDV measurements were acquired. (d) Finite element calculation of centerline velocity dynamics at the inflow region of the heart tube. (e) Calculated pressure along the length of the modeled heart tube. The legend at the bottom corresponds to the time points for the pressure plots.

6.3.1.2 Central Heart Tube Blood Flow Dynamics

The second location in the heart tube where we acquired SDV measurements was towards the center of the tube (Figure 35). This region of the heart tube is just inside the inflow cushions. So, the lumen of the heart tube has a larger radius than the inflow and outflow regions. We expect that the heart tube in these regions does not completely close when the contractile wave passes through it. When the inflow tract is closed, there is no flow downstream of the inflow cushions (Figure 35a and b, red line). As the inflow cushions open, and contractile wave begins to narrow the center of the tube (Figure 35a and b, green line), the contraction forces blood in both the forward and backward direction, resulting in net zero flow. Because the inflow lumen volumetric capacity increases more rapidly than the center of the tube (downstream from the contraction), blood will move more rapidly to fill the upstream space. This causes negative blood flow. As the contractile wave moves to the outflow cushion, downstream resistance increases. With the passing of the contractile wave, the center of the heart tube reopens and blood flows into the central region from upstream, where the resistance to flow is low (Figure 35a and b, blue line). Lastly, when the contractile wave leaves the outflow tract, the center of the tube is completely open and the outflow is opening. The blood velocity reduces back to zero (Figure 35a and b, yellow line).

Based on the finite element velocity calculations (Figure 35e), the pressure in the center of the heart tube relative to the inflow transitions from very high when the contractile wave is passing through the inflow cushions, to negative when the contractile wave reaches the outflow cushions. This creates a transition of blood flow from backwards flow to forwards flow as the contractile wave moves across the center of the tube.

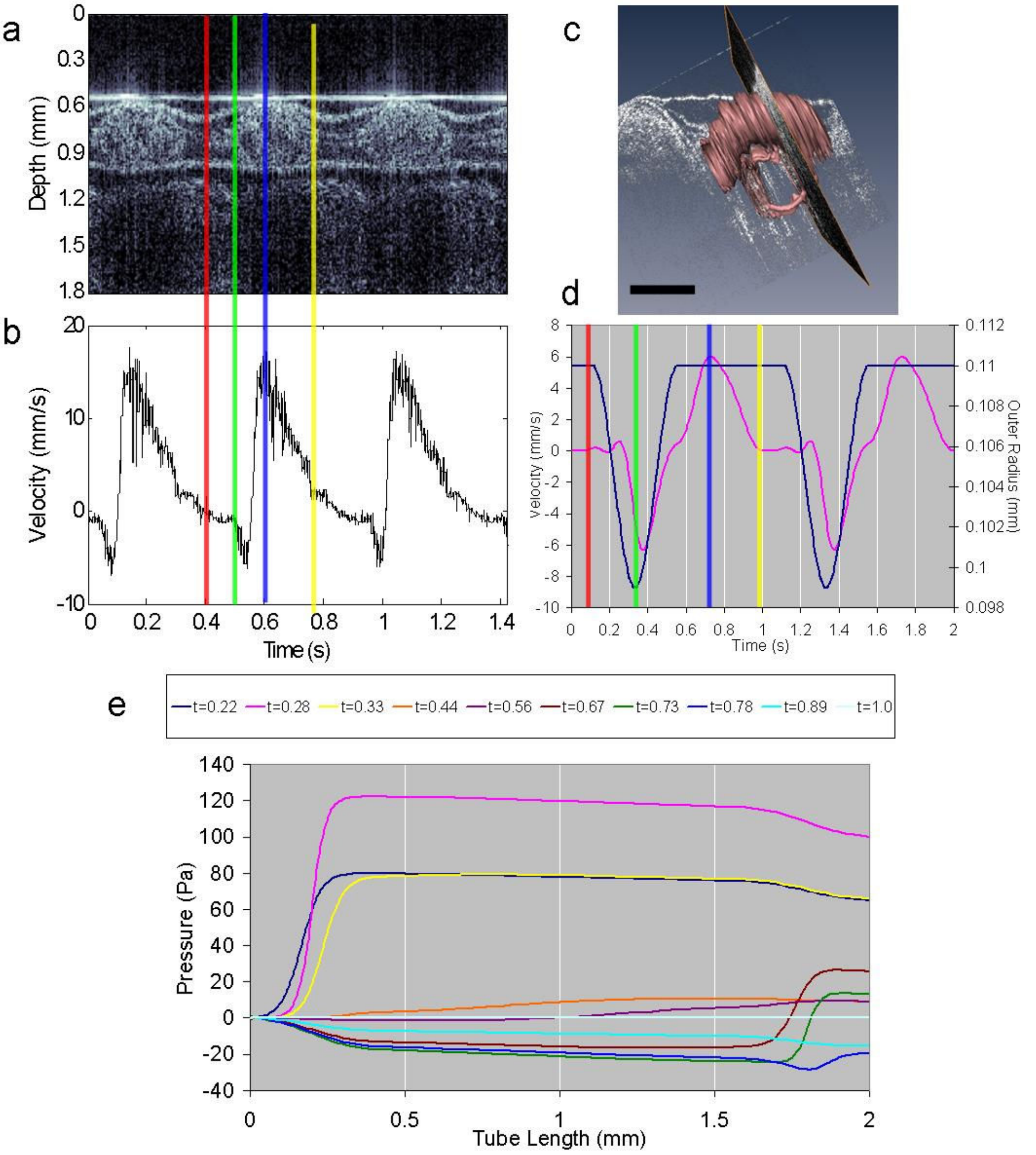

Figure 35: SDV and finite element modeling from center of heart tube. (a) and (b) M-mode and SDV measurements. (c) Volume rendering of heart tube containing cross-sectional slice where SDV measurements were acquired. (d) Finite element calculation of centerline velocity dynamics from the center of the heart tube, near the inflow (x = 0.4). (e) Calculated pressure along the length of the modeled heart tube. The legend corresponds to the time points for the pressure plots.

In addition to the embryo presented here, measurements from a similar location, mid-tube, has been performed in two other embryos. Figure 36 contains SDV measurements from all three embryos. For easier comparison between SDV plots of each embryo I normalized the magnitude and time scales and set t=0 such that the peaks from each plot are overlapped. These results are provided in Figure 37. The general waveform, as detailed in Figure 35 are similar in characteristic peaks between the three embryos. One major variability between the waveforms is timing and magnitude of the negative or back flow relative to the bulk forward flow of blood. I believe that these variabilities are due to differences in heart rate (timing) either by embryo variability or possibly temperature differences or functional differences between embryos.

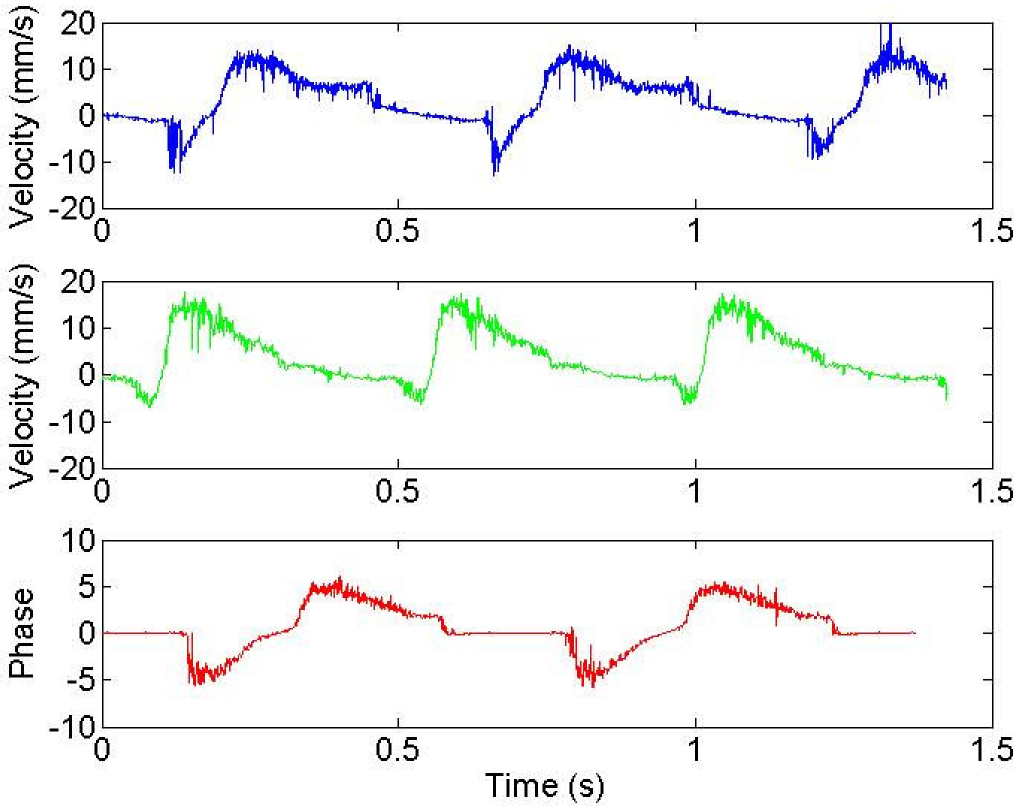

Figure 36: SDV measurements from center of tube in three separate embryos.

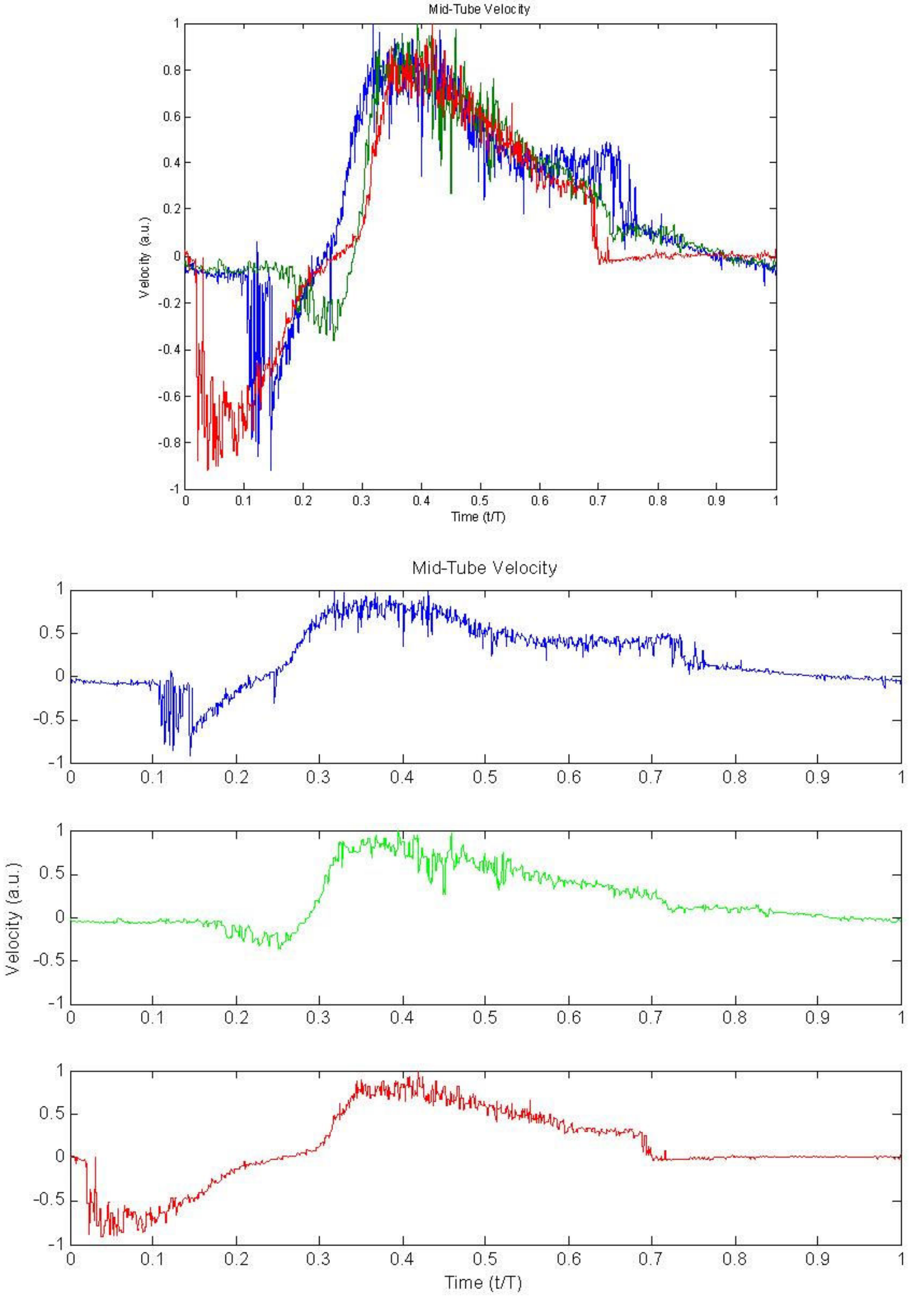

Figure 37: Mid-tube velocity plots N=3. SDV measurements from the middle of the heart tube taken from three separate embryos. These plots show blood flow velocity for one heart beat cycle. (a) For comparison purposes, these plots are normalized in magnitude and time and aligned at peak velocity blood flow. (b) Individual blood flow profiles from the same three embryos.

6.3.1.3 Outflow Tract Blood Flow Dynamics

SDV measurements were acquired at the outflow end of the heart tube. These results along with the finite element simulations of blood flow at the outflow cushions and calculation of pressure along the heart tube are provided in Figure 38.

When the contractile wave initiates closure of the inflow tract, the outflow tract is completely open (Figure 38 a and b, red line). The upstream lumen volume rapidly decreases due to the closure of the inflow cushions and causes blood to rapidly flow out of the outflow tract. As the contractile wave moves towards the middle of the tube (Figure 38 a and b, green line), both the inflow and outflow ends are open. Returning blood will flow into the heart tube behind the traveling contractile wave, the outflow blood velocity will be small due to increasing vascular resistance to flow. When the contractile wave approaches the outflow cushions, the lumen of the outflow tract will rapidly pinch closed. This forces a small amount of blood in the forward direction producing a second peak (Figure 38 a and b, blue line). With all of the blood that has been forced out of the heart tube, the pressure down stream from the outflow tract further increases. When the contractile wave is at the outflow cushions, it can completely block backflow of blood; however, as the outflow begins to reopen, with the passing of the contractile wave, the increased downstream pressure will cause some blood to flow back into the heart tube (Figure 38 a and b, yellow line).

The finite element calculations for centerline velocity through the outflow tract is shown in Figure 38d (pink line). As shown in the SDV measurements, when the contractile wave closes the inflow tract (Figure 38a and b, red line), there is a rapid forward flow of blood out of the outflow tract. When the contractile wave begins to close the outflow cushions (Figure 38a and b, blue line), blood is squirted through the cushion. Lastly, when the outflow cushions begin to reopen, the pressure in the center of the tube is lower than the downstream of the outflow tract (Figure 38e, $0.56 < t < 0.78$) creating backward flow (Figure 38a and b, yellow line). In the M-mode image (Figure 38a) a faint but distinct image of the inflow region of the heart tube can be seen below the outflow. Unlike the simulation, there is no lag between the reopening of the outflow and the closing of the inflow. This results in an immediate transition from backflow (Figure 38a and b, yellow line) to rapid forward flow (Figure 38a and b, red line) in the outflow tract. If there was a lag, we would expect a small period of time where zero net flow occurs through the outflow tract, as shown in the finite element velocity calculation (Figure 38d).

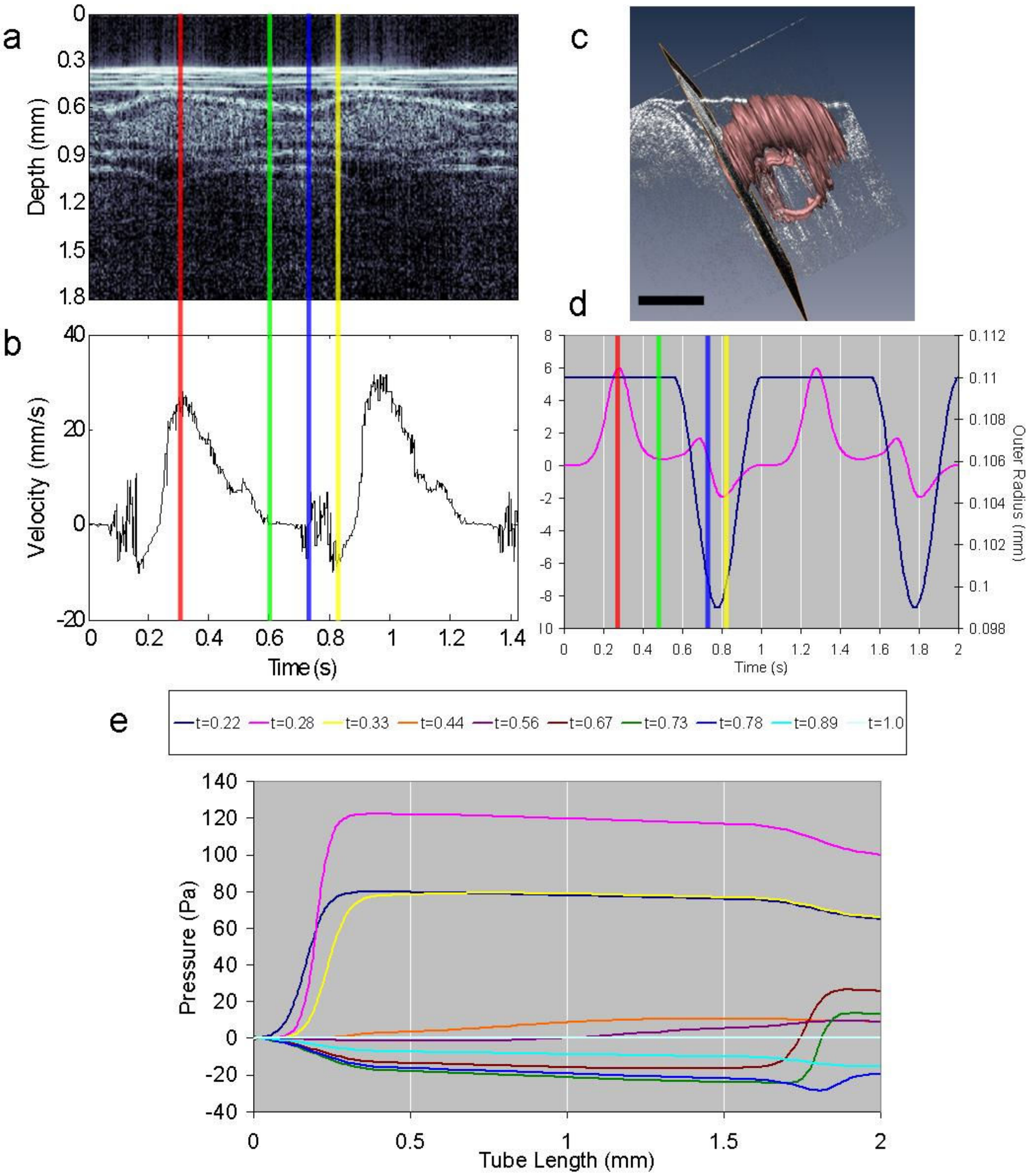

Figure 38: SDV and finite element modeling from outflow tract. (a) and (b) M-mode and SDV measurements. (c) Volume rendering of heart tube containing cross-sectional slice where SDV measurements were acquired. (d) Finite element calculation of centerline velocity dynamics at the outflow region of the heart tube. (e) Calculated pressure along the length of the modeled heart tube.

Figure 39 and Figure 40 shows raw and normalized SDV measurements, respectively, of blood flow dynamics through the outflow tract of five separate embryos. The normalized datasets were processed in the same ways as Figure 37 and aligned at peak blood flow. In four of the five embryos (Figure 40b, plots 2-5) the initial blood flow peak has almost identical shape. The fifth embryo has a broadened initial peak and relatively greater negative or backflow compared to the other four embryos. One important reoccurrence we see is that the blood flow dynamics during a heartbeat consistently presents two positive peaks before any negative or backflow occurs. Detailed discussion of this secondary peak is provided in Chapter 6.3.2.

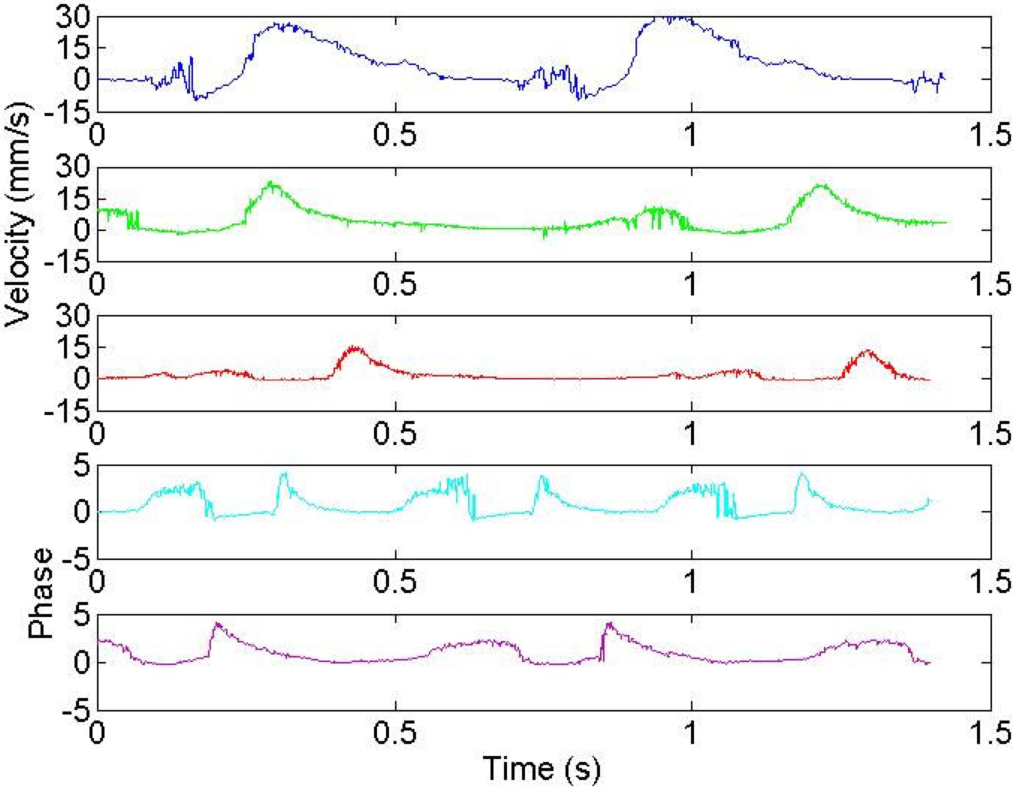

Figure 39: SDV measurements from outflow tract of five separate embryos.

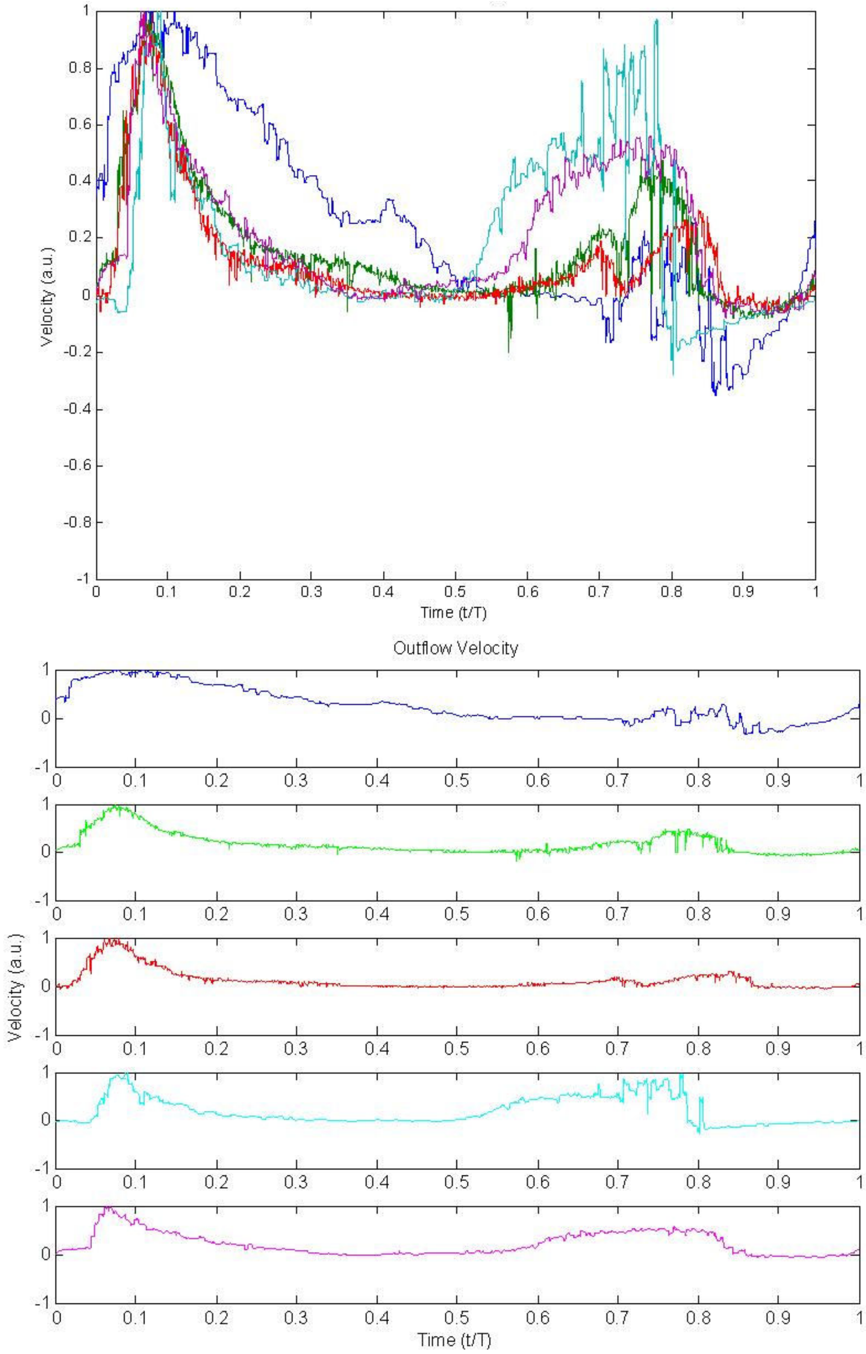

Figure 40: Outflow tract velocity plot N=5. SDV measurements from outflow tract of five separate embryos. These plots show blood flow velocity for one heart beat cycle. (a) For comparison purposes, these plots are normalized in magnitude and time and aligned at peak velocity blood flow. (b) Individual blood flow profiles from the same five embryos.

6.3.1.4. Comparison of Blood Flow Dynamics Between Inflow Tract, Center Tube, and Outflow Tract

Figure 41 shows the average (blue lines) and standard deviation (red lines) of SDV measurements acquired from the inflow tract, center and outflow tract of the heart tube. Figure 41a is the blood flow dynamics over one heartbeat taken from the inflow tract. This dataset is not averaged as I currently have SDV measurements from one embryo. Figure 41b is the blood flow dynamics over one heartbeat taken from a position in the center of the heart tube. This data set is the average and standard deviation of the three embryos shown in Figure 37. Figure 41c is the blood flow dynamics over one heartbeat taken from the outflow tract and is the average and standard deviation of the five embryos shown in Figure 40. Figure 41 shows that blood flow dynamics have very distinct characteristics depending on the location of the tube. Experimental and simulated data in Figure 34 suggest there is strong backflow that occurs at initiation of contraction which is caused by less vascular resistance upstream from the inflow tract compared to inside the tube. In the center of the tube region (Figure 35 and Figure 41b), like the inflow tract there is little upstream resistance compared to the resistance caused by the outflow cushions. therefore negative flow is measured prior to bulk forward flow. The timing between the negative flow and bulk forward flow in the center tube dynamics is much shorter than in the inflow tract. This difference in timing was also observed in the simulations in Figure 34d and Figure 35d. Two positive flow peaks are present in outflow tract (Figure 41c) blood flow dynamics which is a very unique characteristic to this location of the heart tube. This secondary peak is caused by the rapid closing of the outflow cushions which then force and additional volume of blood in the forward direction. This secondary peak is not observed, nor simulated, in the blood flow dynamics of from the inflow tract or center of the tube.

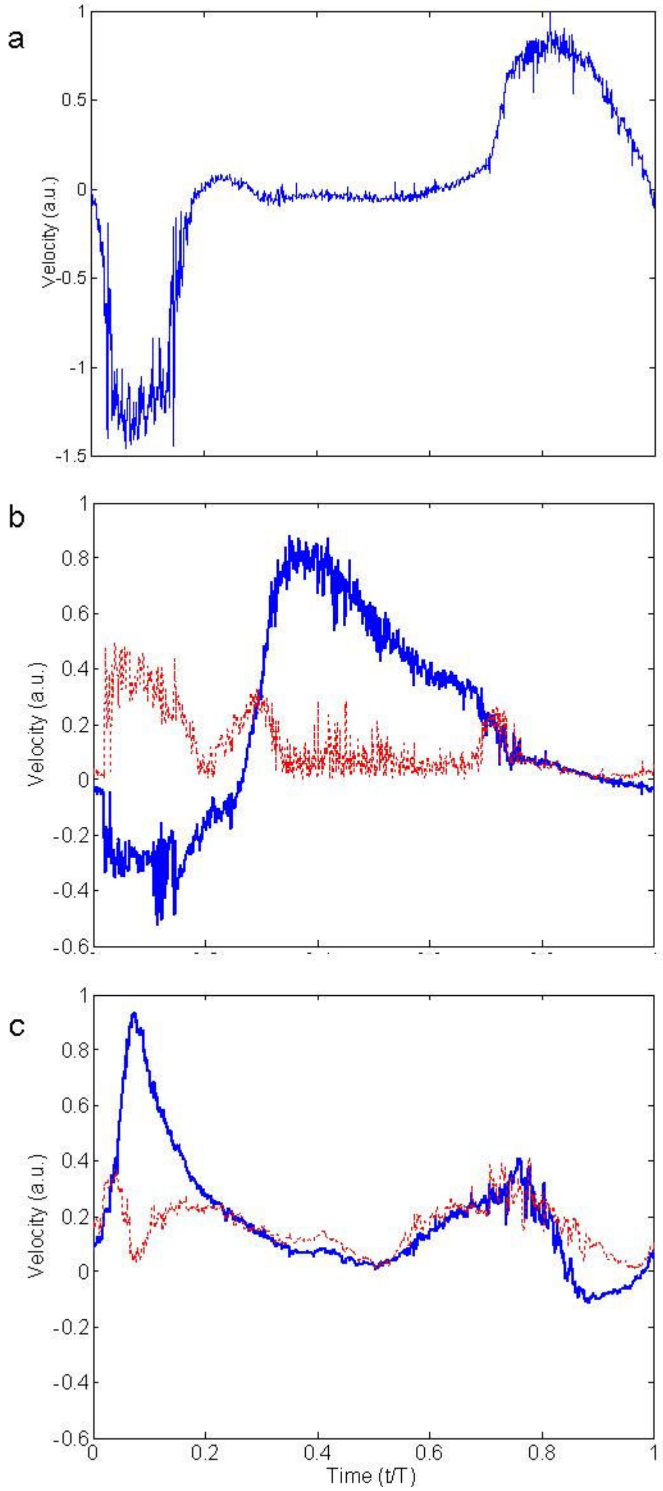

Figure 41: Average (blue) and standard deviation (red) of blood flow dynamics at three different locations in the heart tube. (a) Inflow tract, N=1; (b) Center-tube, N=3; (c) Outflow tract dynamics, N=5.

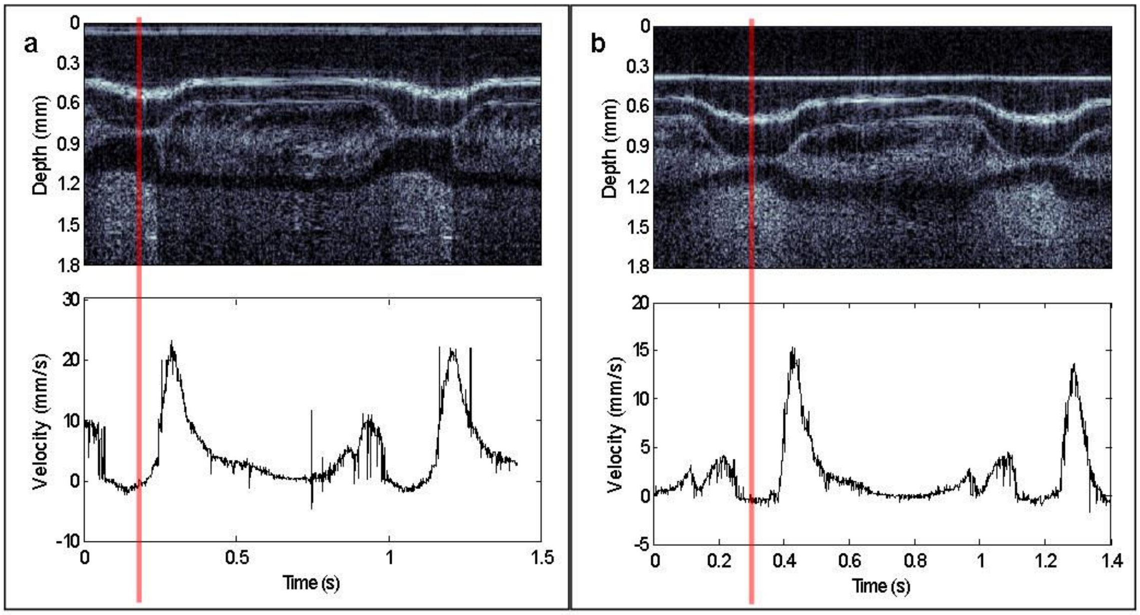

Figure 42: Outflow cushions cause secondary peak. SDV measurements taken from the outflow tract in two separate embryos (a) and (b) show the outflow tract pinches completely closed during contraction (red lines). As the outflow tract closes, it forces a small amount of blood in the forward direction, producing a second positive flow peak.

6.3.2 Outflow Cushions Cause Secondary Blood Flow Peak

In their finite element simulation of blood flow through the outflow cushions, Taber, et. al. [L. A. Taber et al., 2007] found that the rapid closing of the cushions causes a secondary flow peak in the forward direction (Figure 38d). This finding was unexpected; however, by examining the simulation in further detail it becomes evident that the small contraction in myocardium results in a considerably rapid decrease in lumen radius wherever the cushions are located. This quick “pinch” forces an additional small amount of blood in the forward direction (Figure 38b, blue line), resulting in a secondary peak. In Figure 42, we show M-mode images and SDV measurements from the outflow tract of two embryonic heart tubes. At full contraction (Figure 42, red line) the myocardium radius for the two heart tubes decreased by 22% and 33%, respectively. Also at full contraction, the cardiac jelly appears to thicken in the M-mode image. The “thickening” of the cardiac jelly arises from conservation of the cardiac jelly cross sectional area (Figure 43) during contraction. The cardiac jelly is an incompressible material which forms mounds in the early stages of endocardial cushion development. As illustrated in Figure 43b, a small decrease in myocardium radius results in a significant decrease in the heart tube lumen, due to the presence of the cushions. This concept was first described by Barry in the 1930's [A. Barry, 1948]. The occurrence of a secondary peak in the SDV measurements from the outflow tract was repeatedly measured in a total of 5 embryos (Figure 39 and Figure 40).

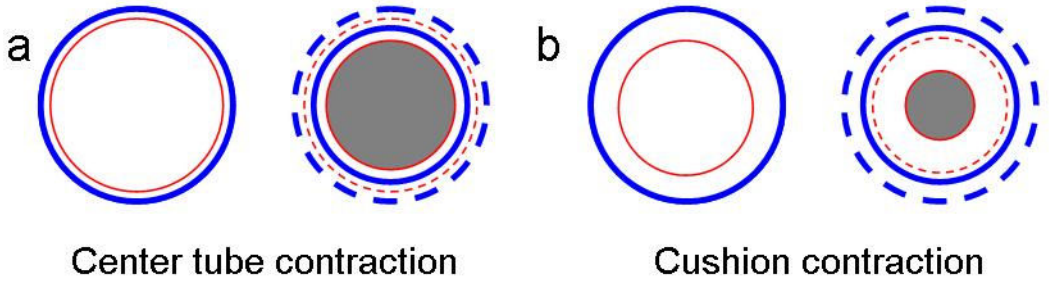

Figure 43: Illustration of changes in lumen area during contraction. (a) The heart tube wall is thinner in the center of the tube compared to the inflow and outflow regions which contain endocardial cushions (b). A 20% contraction of the myocardial radius (blue circles) causes a significantly smaller tube lumen (gray area) in regions with cushions compared to the center of the tube with no cushions. Blue lines, myocardium; red lines, endocardium; dotted lines indicate relaxed myocardial and endocardial radii.

In areas where there are no cushions, such as the center of the heart tube, an equivalent decrease in myocardium radius will not result in the same decrease in heart tube lumen as in the cushioned regions (Figure 43a). It is therefore expected that a secondary peak will not form, as the tube will not rapidly "pinch" closed. Figure 35d contains finite element velocity calculations from the center of the tube. As expected, only a single positive peak occurs after the contractile wave passes the center of the tube and has reached the outflow cushion. Figure 44 demonstrates in two separate chicken embryos that no secondary peak occurs in the centerline velocity dynamics from the center of the heart tube. The M-mode images in Figure 44 show that, unlike in Figure 42, when the contractile wave approaches the center of the heart tube, the lumen of the tube does not rapidly pinch closed. As a result, there is no extra squirt of blood that is forced in the forward direction, thus no secondary peak. I have confirmed that there is no secondary peak in SDV measurements from a total of three embryos (Figure 36 and Figure 37).

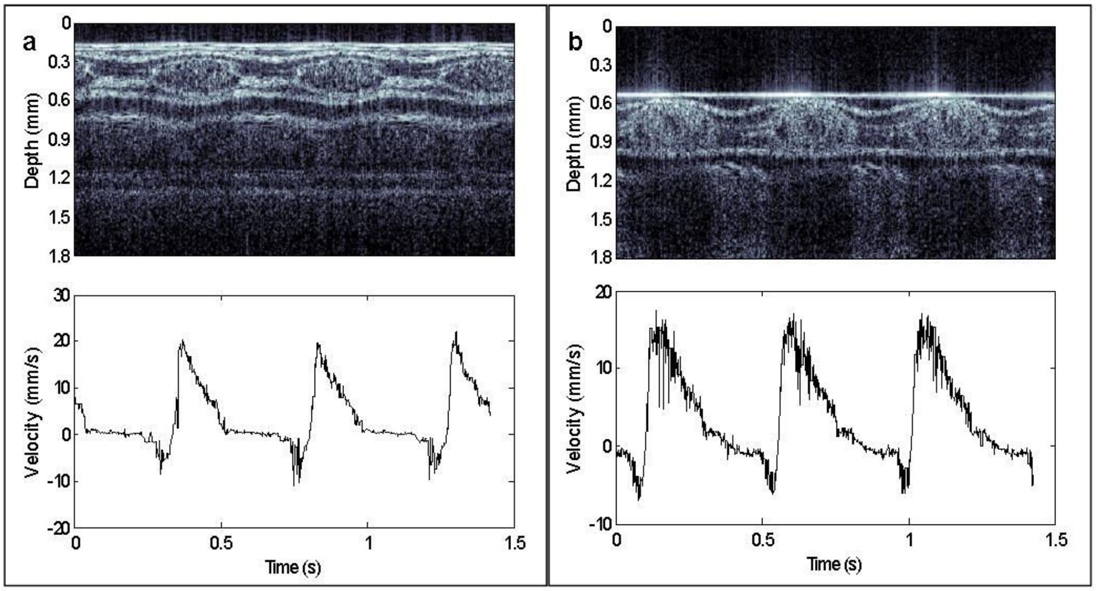

Figure 44: No secondary peak in the center region of the heart tube. Myocardial contraction in the center of the heart tube does not rapidly pinch the tube lumen closed because there are no cushions. Thus, there is no secondary peak.

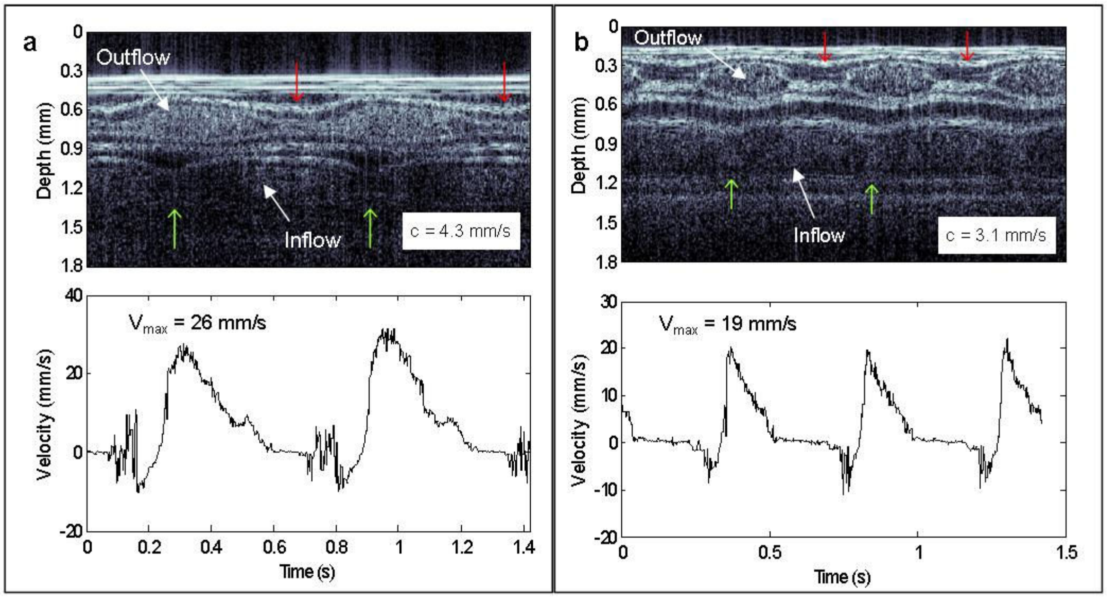

Figure 45: SDV measurements from the outflow tract (a) and primitive ventricle (b) demonstrate peak velocities faster than contractile wave speed. The M-mode images (top) display cardiac dynamics from the outflow and inflow regions of the heart tube. Contractile wave speed was calculated based on the time between the contractile wave leaving the inflow (green arrow) to reaching the outflow (red arrow) and divided by the length of the heart tube (measured using volumetric renderings). In both cases, peak velocities were 6 times faster than the contractile wave speed.

6.3.3 Peak Blood Flow Velocities Exceed the Contractile Wave Speed

The looping heart tube, once it is far enough into the looping stage, becomes horseshoe shaped. We have taken advantage of this stage of development to measure the contractile wave speed and compare it to peak blood flow velocity. This has been done by aligning the SDV / M-mode imaging position such that it simultaneously intersects both the inflow and outflow or primitive ventricle regions of the heart tube. Figure 45 shows M-mode and SDV measurements from the outflow and primitive ventricle from two separate embryos, respectively. The M-mode images were aligned for simultaneous visualization of both the inflow and either outflow or ventricle regions of the heart tube. The SDV plots display the centerline velocity dynamics from the outflow or primitive ventricle region of the heart tube. In Figure 45a and Figure 45b the green arrows point to the times when a new contractile wave has entered the heart tube. The red arrows correspond to the times when the contractile wave has traveled along the heart tube to the region in the outflow or primitive ventricle where SDV measurements were acquired. Using the same surface renderings that are used to measure the angle of flow, for quantification of blood flow velocity, the pathlength between the imaged inflow and outflow or primitive ventricle region was measured. Based on the measured pathlength and the time it took for the first contractile wave (Figure 45, first green arrow) to reach the outflow or primitive ventricle (Figure 45, first red arrow) we calculated the contractile wave speed to be 4.3 mm/s and 3.1 mm/s for the two respective embryos.

Peristalsis pumping in a simple tube of uniform thickness cannot produce peak velocities greater than the traveling speed of the contractile wave [L. A. Taber et al., 2007]. Here we show that in both embryos, peak blood flow velocities from the outflow tract and primitive ventricle were six times faster than the measured speed of the contractile wave. The contractile wave speed of the second embryo (Figure 45b) was 28% slower than the contractile wave speed of the first embryo. Similarly, the peak velocity of the measured in the second embryo was 27% slower than the peak velocity from the first embryo. This suggests that the contractile wave speed and blood flow velocities may be linearly related

6.4 Discussion

At the earliest stages of development, the embryonic heart begins to beat and blood starts to flow. It is believed that the purpose for blood flow at these stages development is not for convective transport of oxygen, nutrients, and waste, but rather to induces epigenetic signals for future development [J. R. Hove et al., 2003; W. W. Burggren, 2004]. Perturbations in blood flow, when the heart is still a tube, can create irreversible malformations of the heart, some of which are similar to those seen in humans born with congenital heart disease. To understand the cause of these malformations, we need to understand the mechanism for blood flow in the embryonic heart tube. It has long been theorized that blood flow is caused by a “peristatoid” motion [A. Barry, 1948]. Not until recently has this theory been analytically modeled.

Taber’s model of blood flow through the embryonic heart tube has now enabled us to predict what the blood flow velocity dynamics should look like through the heart tube as a contractile wave travels along the tube. Without experimental validation of this model, these simulations have little meaning. I have developed imaging and blood flow measurement technology for just this reason, to experimentally measure blood flow dynamics in the embryonic chick heart tube.

In Figure 34, Figure 35, and Figure 38 we have shown that the centerline blood velocity dynamics at the inflow, center, and outflow regions of the heart tube, respectively, have distinct forward and backward flow characteristics as predicted by simulations of a peristalsis pump through a embryonic heart tube modified with inflow and outflow cushions. At the inflow tract (Figure 34), blood flows into the heart tube significantly after the contractile wave has passed. This indicates that refilling of blood into the heart tube follows the contractile wave, rather than it being pushing ahead of the wave. Likewise, near the center of the tube (Figure 35), forward blood flow follows the passing of the contractile wave. The outflow tract presents a very different picture in the velocity dynamics compared to the inflow and center regions, with almost exclusively forward flow. The M-mode image in Figure 38a provides visualization of the outflow tract as well as a region near the inflow tract. From this, it is evident that when the outflow tract is completely open, the inflow tract is contracted. The opening and closing alternation of the inflow and outflow cushions is what allows for the rapid filling and ejection of blood into and out of the heart tube, respectively. The thicker cushions in these regions, acting like valves, decrease the amount of back flow that occurs. The absolute velocity values calculated using the finite element simulations are slower than what we measured. We believe that this difference arises from differences in the simulated versus actual percent of myocardial radius decrease. We consistently observe myocardial contractions near or greater than 30% of the resting myocardial radius compared to a 10% decrease in the simulations.

An unexpected observation from the finite element simulations was also validated when studying the blood velocity dynamics at the outflow cushions of the heart tube (Figure 38d). When the contractile wave reaches the outflow cushions, a second peak of forward moving blood is created. According to the simulations, this second peak only occurs ahead of the outflow cushions because they are caused by the rapid closing of the heart tube lumen pushing the blood in that region forward and out of the heart tube. We have shown in Figure 42 that on multiple occasions we see the outflow cushions pinch closed and, as predicted, when the outflow tract pinches closed, a second forward blood flow peak is created. To further support the predictions, we show in Figure 44 that in regions outside of the outflow tract, the secondary peak does not form. As expected, the contraction in the center of the tube does not pinch closed the tube lumen. Therefore, blood is forced in both directions, creating no secondary flow peak. These findings are not only important because they validate unexpected results from the finite element model, but they also suggest that blood volume motion through the heart tube is not in the form of a bolus, but rather gradual, with multiple peaks.

Peristaltic pumping through a simple tube of uniform radius will not produce flow faster than the speed of the pump. The finite element model shows that peristaltic pumping through a tube with narrow ends will produce faster flow velocities than the pump speed, although this may be intuitive if we think about velocities at the location of the cushions. Clearly, to be able to maintain flow rates when the lumen radius decreases, the velocity needs to increase. This is in fact what we show in Figure 45a; however, we also show that the velocities inside the outflow tract are also higher than the wave speed (Figure 45b). In both locations, the peak velocity was 6 times faster than the wave speed.

6.5 Conclusions

Understanding blood flow in the embryonic heart tube has been hampered by limited ability to image and quantify blood flow dynamics in the chicken embryo. I have developed OCT technology which now enables visualization and measurement of the dynamically pumping heart tube and blood flow. Recent work by Taber, et. al., provided new insights in the potential relationship between heart tube structure and blood flow dynamics. Taber predicted that the embryonic heart tube is a peristaltic pump with modified geometry. With his model he observed three things: 1) that the blood flow dynamics at the inflow, center, and outflow regions of the heart tube are distinctly different; 2) a secondary peak is formed after the primary peak only when looking at blood flow through the outflow cushions; and 3) unlike a peristaltic pump through a straight tube, blood flow velocities can exceed the velocity of the traveling contractile wave. In this Chapter I have tested these hypotheses and found that our SDV measurements closely correlate to calculated predictions. In conclusion we have presented a validation of the finite element simulation of peristaltic flow through the embryonic heart tube. Based on these results we believe that the embryonic heart tube is a peristaltic pump modified by inflow and outflow endocardial cushions.

7. Future Directions

This work has produced a wealth of information and data which has never been previously available. The ability to measure velocity dynamics while visualizing the inflow and outflow regions of the heart, simultaneous answers several questions pertaining to the relationship between flow and structure. It also raises even more questions pertaining to the relationship between flow and structure. Here I describe future directions this work could potentially go to advance our understanding of embryonic heart development.

7.1 The Embryonic Chick Heart Tube is Not an Impedance Pump

Recently, a group out of Cal Tech published work that stated the embryonic heart tube is a suction pump [A. S. Forouhar et al., 2006]. The basis of this work was to test, in the zebra fish embryo, certain characteristics that are required by a peristaltic pump model. These characteristics include that 1) there should be a unidirectional wave traveling down the heart tube; 2) blood cell velocities should be bounded by the traveling speed of the contractile wave, and 3) cardiac output should increase linearly with heart rate. In testing these characteristics they determined that upon activation, a contractile wave propagates in both directions relative to the location of activation. The propagating wave then reflects off an impedance mismatch induced by a change in vessel diameter between the inflow or outflow tracts and the venous return or aorta, respectively. Second, they qualitatively show that a single red blood cell moves farther than the contractile wave, indicating that the blood cell velocity is faster than the contractile wave. Additionally, they show that changing the heart rate of the zebra fish by cooling and heating results in a nonlinear dependence of the blood velocity for different heart rates. The last observation they make is that the blood acceleration occurs when the pressure gradient is negative, indicating the heart tube acts as a suction pump.

I hypothesize that the embryonic chick heart tube is not an impedance pump and plan to show that in the chicken embryo, outflow has a linear relationship within a reasonable range of heart rates. Already Taber, et. al. has demonstrated that a peristaltic pump through a tube with similar geometry to an embryonic chick heart tube with endocardial cushions can have blood flow velocities that exceed the contractile wave speed. Additionally, they show that negative pressure gradients can be produced by peristaltic pumping (see Section 6.3.1).

Forouhar, et. al. [A. S. Forouhar et al., 2006] altered the heart rate in the zebra fish by changing the temperature. This techniques is plagued with complications in that changing the temperature not only changes the heart rate but also changes the response of ion channels which then can alter conduction properties. I propose to increase the heart rate in the chicken embryo by administration of isoproterenol, a β-adrenergic agonist which is similar to epinephrine and commonly used to treat asthma. I also propose to decrease the heart rate by administration of cesium chloride (CsCl), a highly alkaline salt which inhibits the forward hyperpolarization-activating current in the sinoatrial node.

Prior to measuring outflow in response to isoproterenol/CsCl administration, a dose-response study should be conducted to gain insight in the relationships between concentration of drug with change in heart rate, as well as response time of drug administration.

Two things that need to be kept in mind prior to this study is that care needs to be taken in ensuring the embryo maintains a constant temperature. To this date I have attempted this by directing a heat lamp on the embryo during imaging session. However, it may be worthwhile to directly measure the change in temperature of an embryo over time. Secondly, drug concentrations need to be carefully chosen such that it changes the heart rate to a noticeable degree yet the response time is not too fast that it cannot be captured within the time it takes to realign the embryo after drug administration.

This study, in addition to results presented in Chapter 6 and simulations using Taber's finite element model, will form a compelling argument for the embryonic chick heart tube as a peristaltic pump.

7.2 Study Hemodynamics During Development

At the beginning of this project one area of interest in which this technology was developed for was to study hemodynamics over several stages of development. This type of study has never been performed in the chicken embryo before. In this dissertation, I have presented compelling evidence towards the impact of anatomical structure on the hemodynamic profile. The next step, I believe, would be to directly measure changes in hemodynamic profile as the heart develops. Such a study would pinpoint relationships between milestones in structural development and changes in blood flow dynamics. By quantifying blood flow over these stages, we could also estimate shear rate on the heart tube walls. This step would enable correlation of changes in shear to changes in development as well as future changes in blood flow.

I would expect that this study would be straight forward to implement. Figure 31 demonstrates a preliminary study in which I acquired volume and SDV measurements at two stages of development, HH 11 and HH 14. This study was performed under the original adapted microscope and had significantly wrapped phase. Also, I have already shown that we are capable of acquiring volumetric images over several stages of development of the chicken embryo (Figure 21) using this technology. The first thing I would recommend in building an incubating chamber around the egg which would enable the embryo to develop under the pivoting microscope. There are two reasons for building this incubating chamber. First, we could maintain a constant temperature for the embryo which would ensure the heart to function normally, including maintaining physiologically accurate heart rates. Second, the ability to keep the egg in the same position under the microscope would enable rapid imaging and SDV measurements over several days of development. Correlation between one time point to another would not be affected by possibly different embryo orientations. This incubating chamber would need to be utilized for the following studies, as well.

7.3 Correlation Between Blood Flow Dynamics and Electrical Action Potential

Developmental cardiologists often utilize electro-cardiograms (ECG) to study heart function. Therefore, I believe it would be of great value to develop methodology which would enable measurement of the electrical conduction of the embryonic heart while taking SDV measurements. Up to this point, I have used the M-mode images to identify the location and timing of the contractile wave. These M-mode images were then correlated to the SDV blood flow plots. One question that is often raised is, “what does the electro-cardiogram look like, relative to the M-mode images of the contractile wave and the SDV plots?” Incorporating ECG techniques will provide a full picture of the function of the embryonic heart. Once baseline measurements have been taken, studies could be conducted on the effects of mechanical, electrical, genetic, or chemical perturbations on cardiac structure and function.

ECG recordings in the chicken embryo is not a trivial technique, especially if we want to make them *in ovo*. Jenkins, et al. spent a considerable amount of time working on acquiring ECG measurements from the chicken embryo for their gated OCT system [Jenkins, 2006 #38]. Further investigation on the challenges of acquiring ECG recordings from the *in vivo* chicken embryo preparation would need to be conducted to evaluate the desire to carry out such studies.

7.4 Simultaneous Multi-site SDV Measurement

One challenge I faced in this project is the ability to pin-point the exact location where SDV measurements were taken. Due to relative limited imaging speed, especially for Doppler imaging, I limited SDV measurements to acquisitions of a single A-scan over time (i.e. no lateral scanning). In order to compare hemodynamics at different locations in the heart tube, sequential measurements needed to be acquired, where the embryo was repositioned between each acquisition. Development of either a faster OCT imaging system or techniques which enable simultaneous OCT measurements at multiple locations in the sample would be of great value. One key study that could be done using a multi-site measurement system is estimating pressure changes in the heart tube. Currently, there is no technique available which enables direct, non-invasive measurement of pressure. In the past micro-pipettes have been inserted into the heart tube to acquire pressure measurements. This technique is highly invasive therefore precluding longitudinal investigations over several stages of development. Pressure gradients are related to changes in blood flow velocity and different locations in the heart tube. If these velocity gradients could be measured, simultaneously, then the pressure gradient could be directly measured. Once baseline measurements are characterized, then studies involving perturbations of flow or chemical manipulations could be performed.

7.5. Doppler and SDV Applications in Zebrafish

This dissertation described new technology based on SDOCT for small animal imaging. I have developed technology towards the aim of not only providing a modality for structural imaging but also functional studies in the form of Doppler blood flow measurements. Although I concentrated on the chicken embryo, this technology can easily be applied to other small animals such as zebrafish. Zebrafish is a very common animal used to study heart development, An advantage of studying zebrafish is the ability to correlate blood flow measurements to genetic or protein expression. Many of the above proposed future studies in the chicken embryo could easily be applied to studies in the zebrafish. Additionally, genetic manipulations could be performed to study genetic impact on embryonic heart development. Lastly, due to its smaller size, studies in zebrafish could be performed over more stages of development before the heart becomes too big.

Appendix 1. Pivoting Microscope Solidworks® Design

Here I have provided the design files for the three parts which make up the pivoting microscope. The “Collimating_side” part is where the sample arm light of the 2X2 optical coupler is collimated and centered onto the two galvanometer mirrors. The “Galvo_side” is the back plate on which the x,y galvanometer mount (available through Cambridge Technologies) attaches. The “Focus_side” is designed to fit a 1” lens tube which houses the focusing lens. Note, the diameter of the aperture for the lens tube is actually the same size as the lens tube. The outside of the lens tube can be polished down to make it fit. Also a small tapped hole in the side of the plate is used for a set screw. The collimating side plate and the focusing side plate attach to the “Galvo_side” plate for a complete assembly.

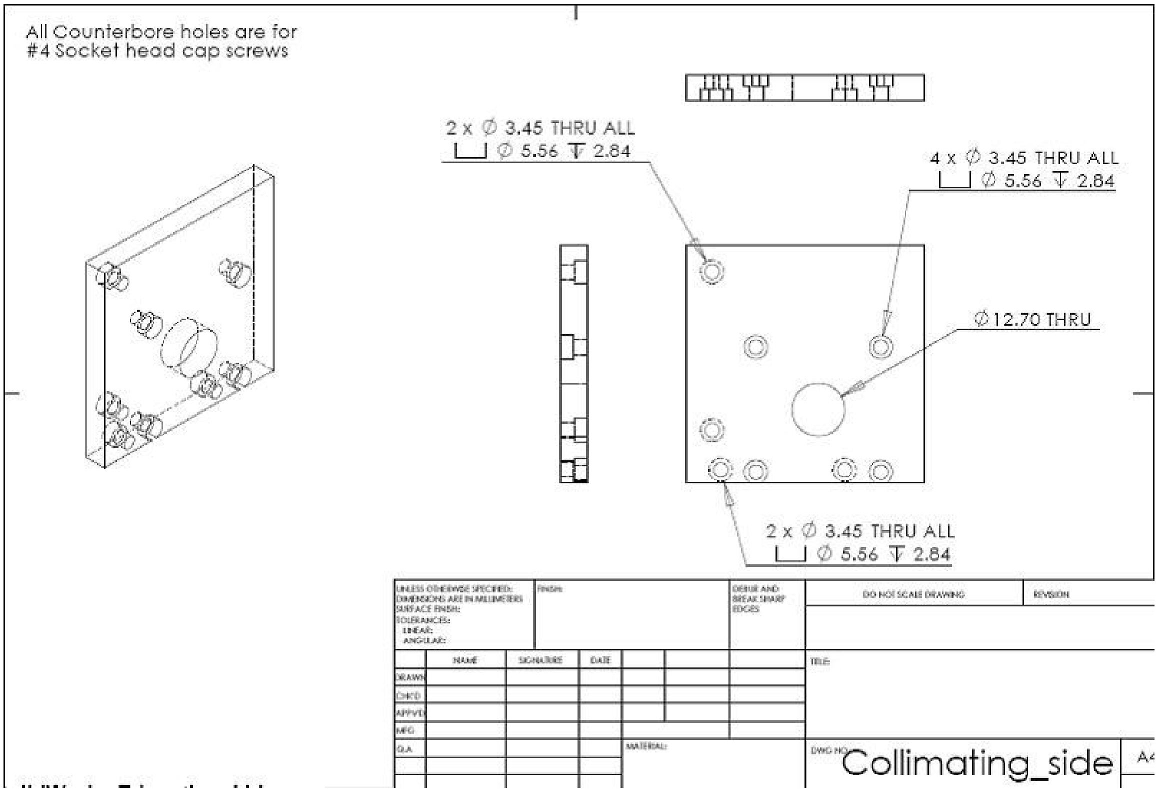
All Counterbore holes are for
#4 Socket head cap screws
2 x ∅ 3.45 THRU ALL
⌴ ∅ 5.56 ↧ 2.84
4 x ∅ 3.45 THRU ALL
⌴ ∅ 5.56 ↧ 2.84
∅12.70 THRU
2 x ∅ 3.45 THRU ALL
⌴ ∅ 5.56 ↧ 2.84
UNLESS OTHERWISE SPECIFIED:
DIMENSIONS ARE IN MILLIMETERS
SURFACE FINISH:
TOLERANCES:
LINEAR:
ANGULAR:
FINISH:
DEBUR AND BREAK SHARP EDGES
DO NOT SCALE DRAWING
REVISION
NAME
SIGNATURE
DATE
DRAWN
CHK'D
APPV'D
MFG
Q.A
MATERIAL:
TITLE:
DWG NO.
Collimating_side
A4

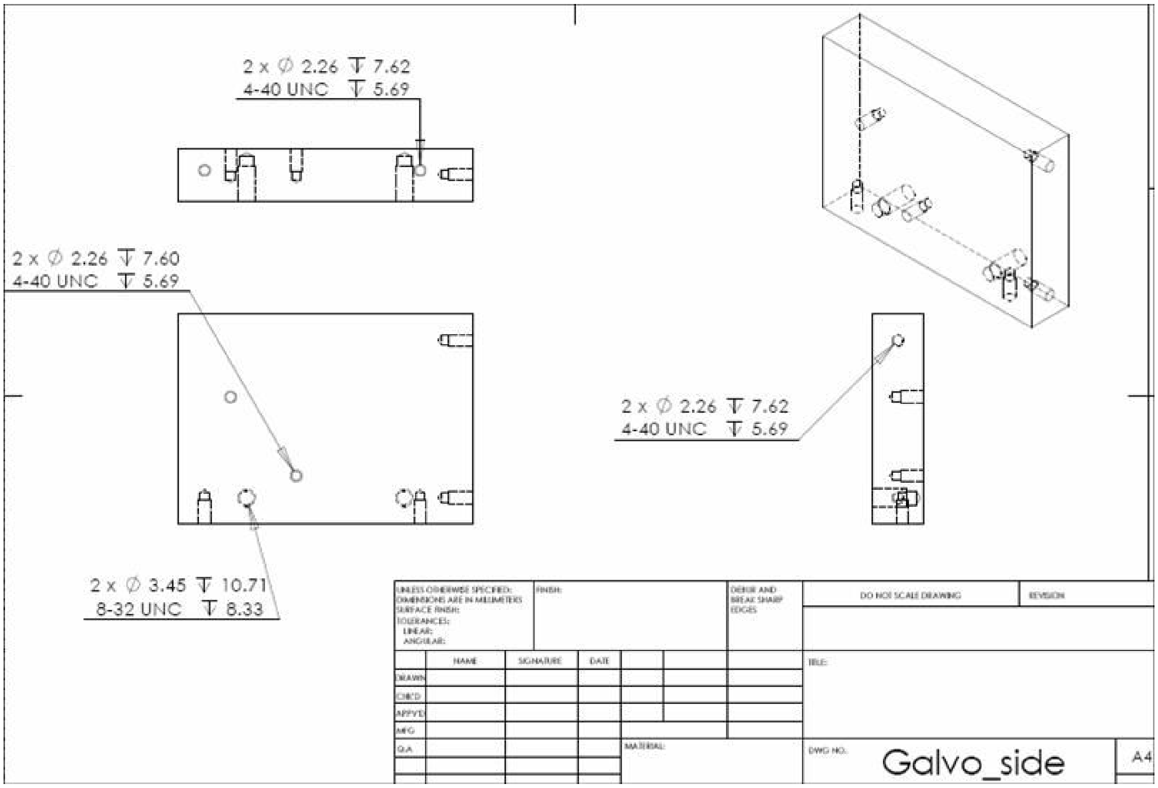
2 x ∅ 2.26 ↧ 7.62
4-40 UNC ↧ 5.69
2 x ∅ 2.26 ↧ 7.60
4-40 UNC ↧ 5.69
2 x ∅ 2.26 ↧ 7.62
4-40 UNC ↧ 5.69
2 x ∅ 3.45 ↧ 10.71
8-32 UNC ↧ 8.33
UNLESS OTHERWISE SPECIFIED:
DIMENSIONS ARE IN MILLIMETERS
SURFACE FINISH:
TOLERANCES:
LINEAR:
ANGULAR:
FINISH:
DEBUR AND BREAK SHARP EDGES
DO NOT SCALE DRAWING
REVISION
NAME
SIGNATURE
DATE
DRAWN
CHK'D
APPV'D
MFG
Q.A
MATERIAL:
TITLE:
DWG NO.
Galvo_side
A4

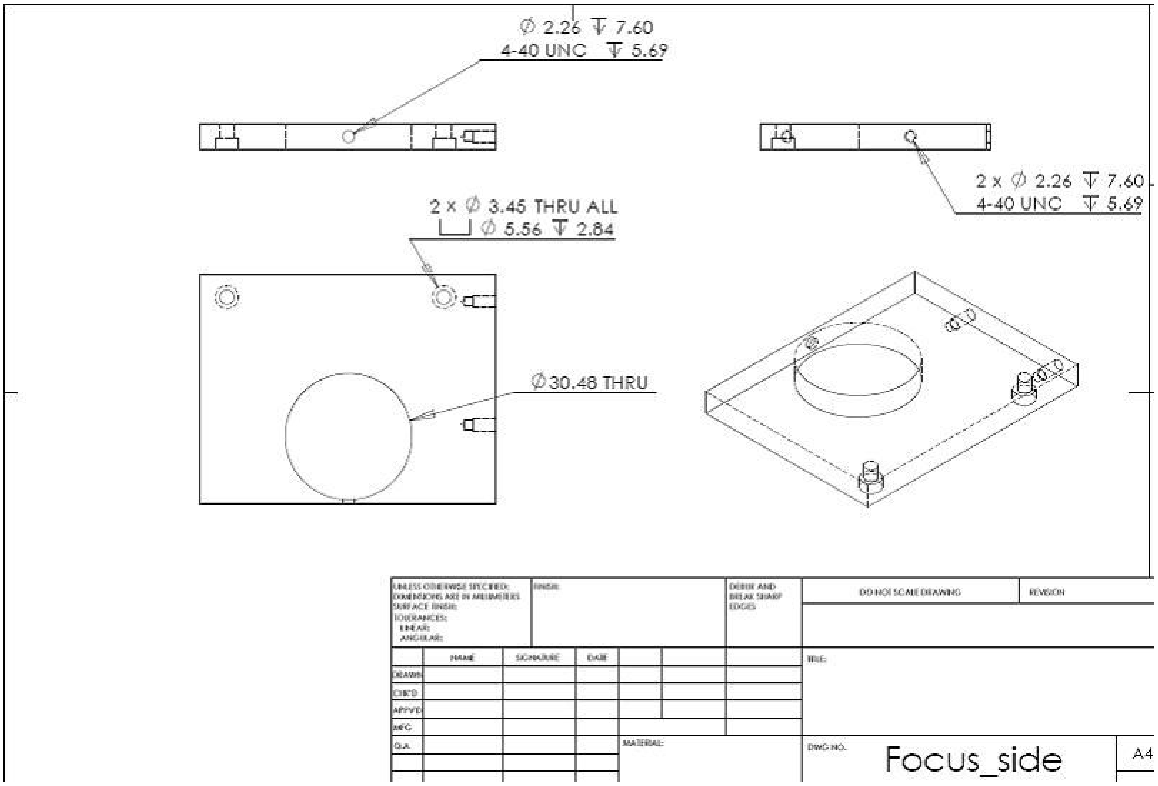
∅ 2.26 ↧ 7.60
4-40 UNC ↧ 5.69
2 x ∅ 2.26 ↧ 7.60
4-40 UNC ↧ 5.69
2 x ∅ 3.45 THRU ALL
⌴ ∅ 5.56 ↧ 2.84
∅30.48 THRU
UNLESS OTHERWISE SPECIFIED:
DIMENSIONS ARE IN MILLIMETERS
SURFACE FINISH:
TOLERANCES:
LINEAR:
ANGULAR:
FINISH:
DEBUR AND BREAK SHARP EDGES
DO NOT SCALE DRAWING
REVISION
NAME
SIGNATURE
DATE
DRAWN
CHK'D
APPV'D
MFG
Q.A
MATERIAL:
TITLE:
DWG NO.
Focus_side
A4

Appendix 2. Matlab® Code for Two-Dimensional Phase Unwrapping

This algorithm was developed by an undergraduate in our lab, Tzuo Hann Law. This algorithm was used to unwrapped phase data in Figure 31 and is based on methodologies described by [Ghiglia, 1998 #152].

```
load 72hrsE4_mmode_heartbeat
E1 = heartbeat_rad;
clear heartbeat_rad;

%% Select the image to unwrap and select region. Smooting with medfilt2
% Kernel size;
Image = E1;% DefineRegion(E1,3); AMD:removed '
%keep Image %AMD:
%Image = Image(:,2:1:end);  %AMD:changed steps of 4 to 2
%%% WINDOW SIZE!

RangeRow = 1:size(Image,1);
RangeCol =  1:size(Image,2);

Image = Image(RangeRow,RangeCol);
imagesc(Image)
%%%%%%%%%%%%%%%%%% Part 1
%% Identifying the residues via 2x2 summation of wrapped diffrences.
Flags = DetectRes(Image);
Flags(:,:,3) = zeros(size(Flags(:,:,1)));
% Flags = FlagRes(Flags);
imagesc(Flags(:,:,1)-Flags(:,:,2))

%% Removing dipoles from preprocessing
Flags = Dipoles(Flags,3);
Flags = Dipoles2(Flags,3);
Dips = Flags(:,:,3);
%%%%%%%%%%%%%%%%%% Part 2
%% Branch cuts
Flags = BranchCut(Flags,30);
Image = Image(1:size(Flags(:,:,1),1),1:size(Flags(:,:,1),2));

%%%%%%%%%%%%%%%%%% Path 3
%% Path Integration
% Flags = ModBranchCuts(Unwrap,Flags);
Unwrap = PathInt(Flags(:,:,3),Image);
Branches = Flags(:,:,3);
Plot2_1
figure(2)
% subplot(2,1,2)
ImageWhole = Image;
```

```
FlagsWhole = Flags;
BranchesWhole = Branches;
DipsWhole = Dips;
imagesc(10*DipsWhole + 5*FlagsWhole(:,:,1)-
5*FlagsWhole(:,:,2)+BranchesWhole);
colorbar

x1 = input('X1 ');
x2 = input('X2 ');
y1 = input('Y1 ');
y2 = input('Y2 ');
 [Branches,Dips,Flags,Image] =
UnwrapWindowIn(x1,x2,y1,y2,BranchesWhole,DipsWhole,FlagsWhole,ImageWhol
e);
ManualCut;
[BranchesWhole, DipsWhole,FlagsWhole,ImageWhole] =
UnwrapWindowOut(x1,x2,y1,y2,Branches,Dips,Flags,Image,BranchesWhole,
DipsWhole,FlagsWhole,ImageWhole);

-------------------------------------------------------------------
function [Flags] = DetectRes(Image);
XY = size(Image);
Diffrences(:,:,1) = Image(1:XY(1)-1,1:XY(2)-1)-Image(1:XY(1)-
1,2:XY(2));
Diffrences(:,:,2) = Image(1:XY(1)-1,2:XY(2))-Image(2:XY(1),2:XY(2));
Diffrences(:,:,3) = Image(2:XY(1),2:XY(2))-Image(2:XY(1),1:XY(2)-1);
Diffrences(:,:,4) = Image(2:XY(1),1:XY(2)-1)-Image(1:XY(1)-1,1:XY(2)-
1);
WrappedDiff(1:XY(1)-1,1:XY(2)-1) =
atan2(sin(Diffrences(:,:,1)),cos(Diffrences(:,:,1)))+atan2(sin(Diffrenc
es(:,:,2)),cos(Diffrences(:,:,2)))+atan2(sin(Diffrences(:,:,3)),cos(Dif
frences(:,:,3)))+atan2(sin(Diffrences(:,:,4)),cos(Diffrences(:,:,4)));

Flags(:,:,1) = WrappedDiff > pi;
Flags(:,:,2) = WrappedDiff < -pi;

-------------------------------------------------------------------
function Flags = Dipoles(Flags,N);
CutTemp = [];
Jump = 0;
[Ab,Bb] = find(Flags(:,:,1) == 1);
for b = 1:size(Ab,1)
    A = Ab(b);
    B = Bb(b);
    for n = 3:2:N
        % relating n to range before and after center
        Range = (n-1)/2;
        % Restricting Box to a defined domain
        BoxDomain = 0;
        BoxDomain = [(A-Range:A+Range)' (B-Range:B+Range)'];
        BoxDomain(BoxDomain(:,1) < 1,1) = 1;
        BoxDomain(BoxDomain(:,1) > size(Flags(:,:,1),1),1)  = 1;
        BoxDomain(BoxDomain(:,2) < 1,2) = 1;
        BoxDomain(BoxDomain(:,2) > size(Flags(:,:,1),2),2)  = 1;
        % Creating the active box
        for ab = 1:n
            ActiveBox1(1:n,ab) = BoxDomain(:,1)';
            ActiveBox2(ab,1:n) = BoxDomain(:,2);
        end
        for ab = 1:numel(ActiveBox1);
%             if ActiveBox1(ab) == A | ActiveBox2(ab) == B;
                if Flags(ActiveBox1(ab),ActiveBox2(ab),2) == 1
                    CutTemp = [CutTemp; Cuts([A B],[ActiveBox1(ab)
ActiveBox2(ab)])];
                    Flags(A,B,1) = 0;
                    Flags(ActiveBox1(ab),ActiveBox2(ab),2) = 0;
                    Jump = 1;
                    break
                end
%             end
        end
        if Jump == 1
            Jump = 0;
            break
        end
    end
end
for a = 1:size(CutTemp,1)
    Flags(CutTemp(a,1),CutTemp(a,2),3) = 1;
end

-----------------------------------------------------------------------
function [Flags] = BranchCut(Flags,N)
% FLAGS LEGEND POS  NEG Cut(1) Border(1) Balanced(1) Active(1)
% BOXES LEGEND POS  NEG BALANCED ACTIVE
% marking out the unbalanced stuff
Flags(:,:,5) = Flags(:,:,1) + Flags(:,:,2) == 0;
% all pixels are inactive
Flags(:,:,6) = zeros(size(Flags(:,:,5)));
% initiating the list of cuts
CutTemp = [];
% initiating the break value
Jump = 0;
%for all unbalanced residues
while sum(sum(Flags(:,:,5))) < numel(Flags(:,:,5));
    Active = [];
    % pick any one to start ActiveSets
    [Active(1), Active(2)] = find(Flags(:,:,5) == 0,1,'first');
    % Mark balanced
    Flags(Active(1),Active(2),5) = 1;
    % tally charge
    Charge = Flags(Active(1),Active(2),1) -
Flags(Active(1),Active(2),2);
    % mark active
    Flags(Active(:,1),Active(:,2),6) = 1;
    % for n = 3:2:{max box size}
    for n = 3:2:N;
```

```
        if Jump == 1
            break
        end
        % relating n to range before and after center
        Range = (n-1)/2;
        % for each active pixel which is updated
        ActiveOld = 0;
        while ActiveOld < size(Active,1);
            ActiveOld = size(Active,1);
            for a = 1:size(Active,1)
                if Jump == 1
                    break
                end
                %Restricting Box to a defined domain
                BoxDomain = [];
                BoxDomain = [(Active(a,1)-Range:Active(a,1)+Range)'
(Active(a,2)-Range:Active(a,2)+Range)'];
                BoxDomain(BoxDomain(:,1) < 1,1) = 1;
                BoxDomain(BoxDomain(:,1) > size(Flags(:,:,1),1),1)  =
1;
                BoxDomain(BoxDomain(:,2) < 1,2) = 1;
                BoxDomain(BoxDomain(:,2) > size(Flags(:,:,1),2),2)  =
1;
                %resetting Boxes
                Boxes = [];
                % centering nXn box at pixel
                Boxes = Flags(BoxDomain(:,1),BoxDomain(:,2),[1 2 4 5
6]);
                % creating box for index of nxn matrix
                ActiveBox1 = 0;
                ActiveBox2 = 0;
                for ab = 1:n
                    ActiveBox1(1:n,ab) = BoxDomain(:,1)';
                    ActiveBox2(ab,1:n) = BoxDomain(:,2);
                end
                % for each pixel in nXn box
                for b = 1:numel(Boxes(:,:,1))
                    if Jump == 1;
                        break
                    end
                    % if inactive residue
                    if (Boxes(b)+Boxes(n^2+b)).*~Boxes(4*n^2+b) == 1;
                        % if unbalanced
                        if Boxes(3*n^2+b) == 0;
                            % tally charge
                            Charge = Charge + Boxes(b) - Boxes(n^2+b);
                            % balance the box
                            Boxes(3*n^2 + b) = 1;
                            % Update Flags(Balanced?)
                            Flags(ActiveBox1(b),ActiveBox2(b),5) = 1;
                        end
                        % mark it active
                        Boxes(4*n^2 + b) = 1;
                        % update Flags(ACTIVE?)
                        Flags(ActiveBox1(b),ActiveBox2(b),6) = 1;
                        % Adding to Active in current set to repeat NxN
                        Active = [Active; [ActiveBox1(b)
ActiveBox2(b)]];
                        % branch cut
                        CutTemp = [CutTemp; Cuts([ActiveBox1(b)
ActiveBox2(b)], [Active(a,1) Active(a,2)])];
                        for A = 1:size(CutTemp,1)
                            Flags(CutTemp(A,1),CutTemp(A,2),3) = 1;
                        end
                    end
                    % if charge is 0, jump to statement
                    if Charge == 0;
                        Jump = 1;
                    end
                end
            end
        end
    end
    if Charge ~= 0;
        Dist(1) = min(Active(:,1)) - 1;
        Dist(2) = size(Flags(:,:,1),2) - max(Active(:,2));
        Dist(3) = size(Flags(:,:,1),1) - max(Active(:,1));
        Dist(4) = min(Active(:,2)) - 1;
        MinDist = min(Dist);
        switch MinDist
            case  Dist(1)
                Border = Active(Active(:,1) == min(Active(:,1)),:);
                CutTemp = [CutTemp; Cuts([Border(1,:)], [1
Border(1,2)])];
            case Dist(2)
                Border = Active(Active(:,2) == max(Active(:,2)),:);
                CutTemp = [CutTemp; Cuts([Border(1,:)], [Border(1,1)
size(Flags(:,:,1),2)])];
            case Dist(3)
                Border = Active(Active(:,1) == max(Active(:,1)),:);
                CutTemp = [CutTemp; Cuts([Border(1,:)],
[size(Flags(:,:,1),1) Border(1,2)])];
            case Dist(4)
                Border = Active(Active(:,2) == min(Active(:,2)),:);
                CutTemp = [CutTemp; Cuts([Border(1,:)], [Border(1,1)
1])];
        end
        for A = 1:size(CutTemp,1)
            Flags(CutTemp(A,1),CutTemp(A,2),3) = 1;
        end
    end
    % Updating all the Flags and resetting data.
    for A = 1:size(CutTemp,1)
        Flags(CutTemp(A,1),CutTemp(A,2),3) = 1;
    end
    %     subplot(2,1,1)
    %     imagesc(Flags(:,:,1)-Flags(:,:,2))
    %     colorbar
    %     subplot(2,1,2)
    %     imagesc(Flags(:,:,3)+2*Flags(:,:,6))
    %     colorbar
    %     keyboard
    Flags(:,:,6) = 0;
    Jump = 0;
    Active = [];
    Boxes = [];
    Charge = 0;
    CutTemp = [];
end

-----------------------------------------------------------------------
function [Unwrap] = PathInt(Flags,Image);
XY = size(Flags);
% Unwrap 1 = Unwrapped Image, Unwrap 2 = Unwrapped? (1,0)
Unwrap(:,:,1) = zeros(XY);
Unwrap(:,:,2) = zeros(XY);
Adj = zeros(XY);
while nnz(Unwrap(:,:,2)) < (numel(Image)-nnz(Flags));
    % starting pixel must not be unwrapped or branchcut
    A = Unwrap(:,:,2) == 0;
    B = Flags == 0;
    [A,B] = find(A.*B == 1,1,'first');
    AB = [A B];
    %           AB = AB(ceil(rand(1,1)*size(AB,1)),:);
    A = AB(1);
    B = AB(2);
    Unwrap(A,B,1) = Image(A,B);
    Unwrap(A,B,2) = 1;
    Adj(A,B) = 0;
    Step = [[1 0]; [0 1]; [-1 0]; [0 -1]];
    for a = 1:4;
        Stepa = [A+Step(a,1), B+Step(a,2)];
        if (Stepa(1) > 0 && Stepa(1) <= size(Image,1) && Stepa(2) > 0
&& Stepa(2) <= size(Image,2));
            Diffe = Image(Stepa(1),Stepa(2)) - Image(A,B);
            if Adj(Stepa(1),Stepa(2)) == 0;
                if Unwrap(Stepa(1),Stepa(2),2) == 0;
                    if Flags(Stepa(1),Stepa(2)) == 0;
                        Unwrap(Stepa(1),Stepa(2),1) = Unwrap(A,B) +
atan2(sin(Diffe),cos(Diffe));
                        Unwrap(Stepa(1),Stepa(2),2) = 1;
                        Adj(Stepa(1),Stepa(2)) = 1;
                    end
                end
            end
        end
    end
    while nnz(Adj) ~= 0;
        [Alist,Blist] = find(Adj == 1);
        for c = 1:size(Alist,1);
            A = Alist(c);
            B = Blist(c);
            Adj(A,B) = 0;
            Step = [[1 0]; [0 1]; [-1 0]; [0 -1]];
            for a = 1:4;
                Stepa = [A+Step(a,1), B+Step(a,2)];
                if (Stepa(1) > 0 && Stepa(1) <= size(Image,1) &&
Stepa(2) > 0 && Stepa(2) <= size(Image,2));
                    Diffe = Image(Stepa(1),Stepa(2)) - Image(A,B);
                    if Adj(Stepa(1),Stepa(2)) == 0;
                        if Unwrap(Stepa(1),Stepa(2),2) == 0;
                            if Flags(Stepa(1),Stepa(2)) == 0;
                                Unwrap(Stepa(1),Stepa(2),1) =
Unwrap(A,B) + atan2(sin(Diffe),cos(Diffe));
                                Unwrap(Stepa(1),Stepa(2),2) = 1;
                                Adj(Stepa(1),Stepa(2)) = 1;
                            end
                        end
                    end
                end
            end
        end
    end
end
while nnz(Unwrap(:,:,2)) < numel(Image);
    [A,B] = find(Flags == 1);
    Step = [[1 0]; [0 1]; [-1 0]; [0 -1]];
    for a = 1:size(A,1);
        Aa = A(a);
        Ba = B(a);
        for b = 1:4
            Stepa = [Aa+Step(b,1), Ba+Step(b,2)];
            if (Stepa(1) > 0 && Stepa(1) <= size(Image,1) && Stepa(2) >
0 && Stepa(2) <= size(Image,2));
                if Unwrap(Stepa(1),Stepa(2),2) == 1;
                    Diffe = Image(Aa,Ba) - Image(Stepa(1),Stepa(2));
                    Unwrap(Aa,Ba,1) = Unwrap(Stepa(1),Stepa(2)) +
atan2(sin(Diffe),cos(Diffe));
                    Unwrap(Aa,Ba,2) = 1;
                    Flags(Aa,Ba) = 0;
                    break
                else
                end
            end
        end
    end
end
Unwrap = Unwrap(:,:,1);

-----------------------------------------------------------------------
function [Branches,Dips,Flags,Image] =
UnwrapWindowIn(x1,x2,y1,y2,BranchesWhole,DipsWhole,FlagsWhole,ImageWhol
e);
Image = ImageWhole(x1:x2,y1:y2);
Flags = FlagsWhole(x1:x2,y1:y2,:);
Branches = BranchesWhole(x1:x2,y1:y2,:);
```

```
Dips = DipsWhole(x1:x2,y1:y2);
-----------------------------------------------------------------------
function [BranchesWhole, DipsWhole,FlagsWhole,ImageWhole] =
UnwrapWindowOut(x1,x2,y1,y2,Branches,Dips,Flags,Image,BranchesWhole,
DipsWhole,FlagsWhole,ImageWhole);
ImageWhole(x1:x2,y1:y2) = Image;
FlagsWhole(x1:x2,y1:y2,:)= Flags;
BranchesWhole(x1:x2,y1:y2,:) = Branches;
DipsWhole(x1:x2,y1:y2) = Dips;
```

Appendix 3. Matlab Code for Alignment of Multiple SDV Plots

Here is the Matlab code used to align SDV measurements from different embryos in Chapter 6.

```
waveX=M30_55hrsE3p2;
x1=273; x2=2475;
A=resample(waveX(x1:x2),2767,max(size(waveX(x1:x2))));
A=A/max(A);
for i=1:10
    [corr,index]=max(xcorr(wave4,A))
    shift=index-2767;
    x1=x1-shift; x2=x2-shift;
    A=resample(waveX(x1:x2),2767,max(size(waveX(x1:x2))));
    A=A/max(A);
    i
end;
```

References

AHA. 2004. "Congenital heart defects in children fact sheet". In. www.americanheart.org/children: American Heart Association

Alford P. W., Taber L. A. 2003. Regional epicardial strain in the embryonic chick heart during the early looping stages. J Biomech 36:1135-1141.

Badea C. T., Fubara B., Hedlund L. W., Johnson G. A. 2005. 4-D micro-CT of the mouse heart. Mol Imaging 4:110-116.

Barry A. 1948. The functional significance of the cardiac jelly in the tubular heart of the chick embryo. Anat Rec 102:289-298.

Bizheva K., Povazay B., Hermann B., Sattmann H., Drexler W., Mei M., Holzwarth R., Hoelzenbein T., Wacheck V., Pehamberger H. 2003. Compact, broad-bandwidth fiber laser for sub-2-microm axial resolution optical coherence tomography in the 1300-nm wavelength region. Opt Lett 28:707-709.

Bone S. N., Johnson G. A., Thompson M. B. 1986. Three-dimensional magnetic resonance microscopy of the developing chick embryo. Invest Radiol 21:782-787.

Burggren W. W. 2004. What is the purpose of the embryonic heart beat? Or how facts can ultimately prevail over physiological dogma. Physiol Biochem Zool 77:333-345.

Butcher J. T., McQuinn T. C., Sedmera D., Turner D., Markwald R. R. 2007. Transitions in early embryonic atrioventricular valvular function correspond with changes in cushion biomechanics that are predictable by tissue composition. Circ Res 100:1503-1511.

Chien S. 2007. Mechanotransduction and endothelial cell homeostasis: the wisdom of the cell. Am J Physiol Heart Circ Physiol 292:H1209-1224.

Choma M. A., Ellerbee A. K., Yang C., Creazzo T. L., Izatt J. A. 2005. Spectral-domain phase microscopy. Opt Lett 30:1162-1164.

Choma M. A., Sarunic M. V., Yang C., Izatt J. A. 2003. Sensitivity advantage of swept-source and Fourier-domain optical coherence tomography. Opt. Express 11:2183-2189.

Choma M. A., Yang C., Izatt J. A. 2003. Instantaneous Quadrature Low Coherence Interferometry With 3x3 Fiber Optic Couplers. Optics Letters 28:2162-2164.

Chu S.-W., Chen S.-Y., Tsai T.-H., Liu T.-M., Lin C.-Y., Tsai H.-J., Sun C.-K. 2003. *In vivo* developmental biology study using noninvasive multi-harmonic generation microscopy. Optics Express 11:3093-3099.

Davis A. M., Choma M. A., Izatt J. A. 2005. Heterodyne swept-source optical coherence tomography for complete complex conjugate ambiguity removal. J Biomed Opt 10:064005.

Davis C. L. 1924. The cardiac jelly of the chick embryo. Anat. Rec. 27:201-202.

de Jong F., Opthof T., Wilde A. A., Janse M. J., Charles R., Lamers W. H., Moorman A. F. 1992. Persisting zones of slow impulse conduction in developing chicken hearts. Circ Res 71:240-250.

deAlmeida A., McQuinn T., Sedmera D. 2007. Increased ventricular preload is compensated by myocyte proliferation in normal and hypoplastic fetal chick left ventricle. Circ Res 100:1363-1370.

Denk W., Strickler J. H., Webb W. W. 1990. Two-photon laser scanning fluorescence microscopy. Science 248:73-76.

Doetschman T., Gregg R. G., Maeda N., Hooper M. L., Melton D. W., Thompson S., Smithies O. 1987. Targetted correction of a mutant HPRT gene in mouse embryonic stem cells. Nature 330:576-578.

Drexler W. 2004. Ultrahigh-resolution optical coherence tomography. J Biomed Opt 9:47-74.

Effmann E. L., Johnson G. A., Smith B. R., Talbott G. A., Cofer G. 1988. Magnetic resonance microscopy of chick embryos in ovo. Teratology 38:59-65.

Fercher A. F., Hitzenberger C. K., Kamp G., Elzaiat S. Y. 1995. Measurement of Intraocular Distances by Backscattering Spectral Interferometry. Optics Communications 117:43-48.

Fishman M. C., Chien K. R. 1997. Fashioning the vertebrate heart: earliest embryonic decisions. Development 124:2099-2117.

Forouhar A. S., Liebling M., Hickerson A., Nasiraei-Moghaddam A., Tsai H. J., Hove J. R., Fraser S. E., Dickinson M. E., Gharib M. 2006. The embryonic vertebrate heart tube is a dynamic suction pump. Science 312:751-753.

Foster F. S., Zhang M. Y., Zhou Y. Q., Liu G., Mehi J., Cherin E., Harasiewicz K. A., Starkoski B. G., Zan L., Knapik D. A., Adamson S. L. 2002. A new ultrasound instrument for in vivo microimaging of mice. Ultrasound Med Biol 28:1165-1172.

Ghiglia D. C., Pritt M. D. 1998. Two Dimensional Phase Unwrapping, Theory, Algorithms, and Software. New York: Wiley.

Groenendijk B. C., Hierck B. P., Gittenberger-De Groot A. C., Poelmann R. E. 2004. Development-related changes in the expression of shear stress responsive genes KLF-2, ET-1, and NOS-3 in the developing cardiovascular system of chicken embryos. Dev Dyn 230:57-68.

Groenendijk B. C., Hierck B. P., Vrolijk J., Baiker M., Pourquie M. J., Gittenberger-de Groot A. C., Poelmann R. E. 2005. Changes in shear stress-related gene expression after experimentally altered venous return in the chicken embryo. Circ Res 96:1291-1298.

Hamburger V., Hamilton H. L. 1951. A series of normal stages in the development of the chick embryo. Journal of Morphology 88:49-92.

Harrison D. G., Widder J., Grumbach I., Chen W., Weber M., Searles C. 2006. Endothelial mechanotransduction, nitric oxide and vascular inflammation. J Intern Med 259:351-363.

Hogers B., DeRuiter M. C., Gittenberger-de Groot A. C., Poelmann R. E. 1999. Extraembryonic venous obstructions lead to cardiovascular malformations and can be embryolethal. Cardiovascular Research 41:87-99.

Hogers B., Gross D., Lehmann V., de Groot H. J., de Roos A., Gittenberger-de Groot A. C., Poelmann R. E. 2001. Magnetic resonance microscopy at 17.6-Tesla on chicken embryos in vitro. J Magn Reson Imaging 14:83-86.

Holdsworth D. W., Drangova M., Fenster A. 1993. A high-resolution XRII-based quantitative volume CT scanner. Med Phys 20:449-462.

Hove J. R., Koster R. W., Forouhar A. S., Acevedo-Bolton G., Fraser S. E., Gharib M. 2003. Intracardiac fluid forces are an essential epigenetic factor for embryonic cardiogenesis. Nature 421:172-177.

Hu N., Clark E. B. 1989. Hemodynamics of the stage 12 to stage 29 chick embryo. Circ Res 65:1665-1670.

Huang D., Swanson E. A., Lin C. P., Schuman J. S., Stinson W. G., Chang W., Hee M. R., Flotte T., Gregory K., Puliafito C. A., Fujimoto J. G. 1991. Optical Coherence Tomography. Science 254:1178-1181.

Huber R., Adler D. C., Fujimoto J. G. 2006. Buffered Fourier domain mode locking: Unidirectional swept laser sources for optical coherence tomography imaging at 370,000 lines/s. Opt Lett 31:2975-2977.

Huber R., Wojtkowski M., Fujimoto J. G., Jiang J. Y., Cable A. E. 2005. Three-dimensional and C-mode OCT imaging with a compact, frequency swept laser source at 1300 nm. Opt. Exp. 13:10523-10538.

Huisken J., Swoger J., Del Bene F., Wittbrodt J., Stelzer E. H. 2004. Optical sectioning deep inside live embryos by selective plane illumination microscopy. Science 305:1007-1009.

Ishiwata T., Nakazawa M., Pu W. T., Tevosian S. G., Izumo S. 2003. Developmental changes in ventricular diastolic function correlate with changes in ventricular myoarchitecture in normal mouse embryos. Circ Res 93:857-865.

Jenkins M. W., Adler D. C., Gargesha M., Huber R., Rothenberg F., Belding J., Watanabe M., Wilson D. L., Fujimoto J. G., Rollins A. M. 2007. Ultrahigh-speed optical coherence tomography imaging and visualization of the embryonic avian heart using a buffered Fourier Domain Mode Locked laser. Opt. Exp. 15:6251-6267.

Jenkins M. W., Rothenberg F., Nikolski V. P., Hu Z., Watanabe M., Wilson D. L., Efimov I. R., Rollins A. M. 2006. 4D embryonic cardiography using gated optical coherence tomography. Optics Express 14:736-748.

Krug E. L., Runyan R. B., Markwald R. R. 1985. Protein extracts from early embryonic hearts initiate cardiac endothelial cytodifferentiation. Dev Biol 112:414-426.

Lee J. Y., Ji H. S., Lee S. J. 2007. Micro-PIV measurements of blood flow in extraembryonic blood vessels of chicken embryos. Physiol Meas 28:1149-1162.

Leitgeb R., Hitzenberger C. K., Fercher A. F. 2003. Performance of fourier domain vs. time domain optical coherence tomography. Optics Express 11:889-894.

Liebling M., Forouhar A. S., Gharib M., Fraser S. E., Dickinson M. E. 2005. Four-dimensional cardiac imaging in living embryos via postacquisition synchronization of nongated slice sequences. J Biomed Opt 10:054001.

Manasek F. J. 1970. Sulfated extracellular matrix production in the embryonic heart and adjacent tissues. J Exp Zool 174:415-439.

Manasek F. J. 1975. The extracellular matrix: a dynamic component of the developing embryo. Curr Top Dev Biol 10:35-102.

Männer J. 2000. Cardiac Looping in the Chick Embryo: A Morphological Review With Special Reference to Terminological and Biomechanical Aspects of the Looping Process. The Anat. Rec. 259:248-262.

Mariampillai A., Standish B. A., Munce N. R., Randall C., Liu G., Jiang J. Y., Cable A. E., Vitkin I. A., Yang V. X. D. 2007. Doppler optical cardiogram gated 2D color flow imaging at 1000 fps and 4D *in vivo* visualization of embryonic heart at 45 fps on a swept source OCT system. Opt. Exp. 15:1627-1638.

Maronpot R. R., Sills R. C., Johnson G. A. 2004. Applications of magnetic resonance microscopy. Toxicol Pathol 32 Suppl 2:42-48.

Martinsen B. J. 2005. Reference Guide to the Stages of Chick Heart Embryology. Dev. Dyn. 233:1217-1237.

McQuinn T. C., Bratoeva M., Dealmeida A., Remond M., Thompson R. P., Sedmera D. 2007. High-frequency ultrasonographic imaging of avian cardiovascular development. Dev. Dyn. 236:3503-3513.

Oh W. Y., Yun S. H., Tearney G. J., Bouma B. E. 2005. Wide tuning range wavelength-swept laser with two semiconductor optical amplifiers. IEEE Photonics Technology Letters 3:678-680.

Patten B. M., Kramer T. C., Barry A. 1948. Valvular action in the embryonic chick heart by localized apposition of endocardial masses. Anat Rec 102:299-311.

Paulus M. J., Gleason S. S., Kennel S. J., Hunsicker P. R., Johnson D. K. 2000. High resolution X-ray computed tomography: an emerging tool for small animal cancer research. Neoplasia 2:62-70.

Pawley J. B. 2006. Handbook of biological confocal microscopy, 3rd ed: Springer.

Person A. D., Klewer S. E., Runyan R. B. 2005. Cell biology of cardiac cushion development. Int Rev Cytol 243:287-335.

Phoon C. K., Aristizabal O., Turnbull D. H. 2000. 40 MHz Doppler characterization of umbilical and dorsal aortic blood flow in the early mouse embryo. Ultrasound Med Biol 26:1275-1283.

Phoon C. K., Aristizabal O., Turnbull D. H. 2002. Spatial velocity profile in mouse embryonic aorta and Doppler-derived volumetric flow: a preliminary model. Am J Physiol Heart Circ Physiol 283:H908-916.

Phoon C. K., Turnbull D. H. 2003. Ultrasound biomicroscopy-Doppler in mouse cardiovascular development. Physiol Genomics 14:3-15.

Reneman R. S., Arts T., Hoeks A. P. 2006. Wall shear stress--an important determinant of endothelial cell function and structure--in the arterial system in vivo. Discrepancies with theory. J Vasc Res 43:251-269.

Sarunic M. V., Choma M. A., Yang C., Izatt J. A. 2005. Instantaneous Complex Conjugate Resolved Fourier Domain and Swept-Source OCT Using 3x3 Couplers. Optics Express 13:957-967.

Sedmera D., Pexieder T., Rychterova V., Hu N., Clark E. B. 1999. Remodeling of chick embryonic ventricular myoarchitecture under experimentally changed loading conditions. Anat Rec 254:238-252.

Smith B. R. 2001. Magnetic resonance microscopy in cardiac development. Microsc Res Tech 52:323-330.

Smith B. R., Huff D. S., Johnson G. A. 1999. Magnetic resonance imaging of embryos: an Internet resource for the study of embryonic development. Comput Med Imaging Graph 23:33-40.

Smith B. R., Linney E., Huff D. S., Johnson G. A. 1996. Magnetic resonance microscopy of embryos. Comput Med Imaging Graph 20:483-490.

Stern H. M., Zon L. I. 2003. Cancer genetics and drug discovery in the zebrafish. Nat Rev Cancer 3:533-539.

Taber L. A., Sun H., Clark E. B., Keller B. B. 1994. Epicardial strains in embryonic chick ventricle at stages 16 through 24. Circ Res 75:896-903.

Taber L. A., Zhang J., Perucchio R. 2007. Computational model for the transition from peristaltic to pulsatile flow in the embryonic heart tube. J Biomech Eng 129:441-449.

Tobita K., Keller B. B. 2000. Maturation of end-systolic stress-strain relations in chick embryonic myocardium. Am J Physiol Heart Circ Physiol 279:H216-224.

Troxler M., Wilkinson D. 2007. An Unusual Cause of a "Double Pulse". EJVES Extra 13:72-74.

Tsien R. Y. 1998. The green fluorescent protein. Annu Rev Biochem 67:509-544.

Ursem N. T., Stekelenburg-de Vos S., Wladimiroff J. W., Poelmann R. E., Gittenberger-de Groot A. C., Hu N., Clark E. B. 2004. Ventricular diastolic filling characteristics in stage-24 chick embryos after extra-embryonic venous obstruction. J Exp Biol 207:1487-1490.

van Leeuwen T., Kulkarni M. D., Yazdanfar S., Rollins A. M., Izatt J. A. 1999. High-flow-velocity and shear-rate imaging by use of color Doppler optical coherence tomography. Opt Lett 24:1584-1586.

Vennemann P., Kiger K. T., Lindken R., Groenendijk B. C., Stekelenburg-de Vos S., Ten Hagen T. L., Ursem N. T., Poelmann R. E., Westerweel J., Hierck B. P. 2006. In vivo micro particle image velocimetry measurements of blood-plasma in the embryonic avian heart. J Biomech 39:1191-1200.

Wang H., Riha G. M., Yan S., Li M., Chai H., Yang H., Yao Q., Chen C. 2005. Shear stress induces endothelial differentiation from a murine embryonic mesenchymal progenitor cell line. Arterioscler Thromb Vasc Biol 25:1817-1823.

Wang L., Wang Y., Guo S., Zhang J., Bachman M., Li G. P., Chen Z. 2004. Frequency domain phase-resolved optical Doppler and Doppler variance tomography. Optics Communications 242:345-350.

Wang Y., Bower B. A., Izatt J. A., Tan O., Huang D. 2007. In vivo total retinal blood flow measurement by Fourier domain Doppler optical coherence tomography. J Biomed Opt 12:041215.

Weinstein B. M., Fishman M. C. 1996. Cardiovascular morphogenesis in zebrafish. Cardiovasc Res 31 Spec No:E17-24.

Wojtkowski M., Kowalczyk A., Leitgeb R., Fercher A. F. 2002. Full range complex spectral optical coherence tomography technique in eye imaging. Opt Lett 27:1415-1417.

Wojtkowski M., Srinivasan V., Ko T., Fujimoto J., Kowalczyk A., Duker J. 2004. Ultrahigh-resolution, high-speed, Fourier domain optical coherence tomography and methods for dispersion compensation. Opt. Express 12:2404-2422.

Wolf M. J., Amrein H., Izatt J. A., Choma M. A., Reedy M. C., Rockman H. A. 2006. Drosophila as a model for the identification of genes causing adult human heart disease. Proc Natl Acad Sci U S A 103:1394-1399.

Yazdanfar S., Kulkarni M. D., Izatt J. A. 1997. High resolution imaging of *in vivo* cardiac dynamics using color Doppler optical coherence tomography. Optics Express 1:424-431.

Yelbuz T. M., Choma M. A., Thrane L., Kirby M. L., Izatt J. A. 2002. Optical coherence tomography: a new high-resolution imaging technology to study cardiac development in chick embryos. Circulation 106:2771-2774.

Yelbuz T. M., Zhang X., Choma M. A., Stadt H. A., Zdanowicz M., Johnson G. A., Kirby M. L. 2003. Images in cardiovascular medicine. Approaching cardiac development in three dimensions by magnetic resonance microscopy. Circulation 108:e154-155.

Yun S. H., Tearney G. J., Bouma B. E., Park B. H., de Boer J. F. 2003. High-speed spectral-domain optical coherence tomography at 1.3 mu m wavelength. Optics Express 11:3598-3604.

Yun S. H., Tearney G. J., De Boer J. F., Bouma B. E. 2004. Removing the depth-degeneracy in optical frequency domain imaging with frequency shifting. Opt. Exp. 12:4822-4828.

Zhang J., Nelson J. S., Chen Z. P. 2005. Removal of a mirror image and enhancement of the signal-to-noise ratio in Fourier-domain optical coherence tomography using an electro-optic phase modulator. Optics Letters 30:147-149.

Zhang X., Yelbuz T. M., Cofer G. P., Choma M. A., Kirby M. L., Johnson G. A. 2003. Improved preparation of chick embryonic samples for magnetic resonance microscopy. Magn Reson Med 49:1192-1195.

Zhu H., Zon L. I. 2004. Use of the DsRed fluorescent reporter in zebrafish. Methods Cell Biol 76:3-12.

Biography

Anjul Maheshwari Davis was born in Lincoln, Nebraska on September 19, 1977. She received her Bachelor's degree in Biomedical Engineering from Vanderbilt University and a Master's degree in Biomedical Engineering from the University of Rochester, New York. Anjul has three publications in peer-reviewed journals, one book chapter, and has contributed to two patents. She has also given presentations at six optical imaging and biomedical engineering conferences as well as two invited presentations to broader fields in small animal imaging and experimental biology. Below is a list of her publications:

Anjul M. Davis, Joseph A. Izatt, and Florence G. Rothenberg. "Quantitative measurement of blood flow dynamics in embryonic vasculature using spectral Doppler velocimetry." *Anatomical Record*, In Press (2008).

Anjul M. Davis, Michael A. Choma, Joseph A. Izatt. "Heterodyne Swept-Source Optical coherence Tomography for Complete Complex Conjugate Ambiguity Removal." *Journal of Biomedical Optics* Opt 10, 064005 (2005).

Brett A. Hooper, Anjul Maheshwari, Adam C. Curry, and Todd M. Alter. "Catheter for Diagnosis and Therapy with Infrared Evanescent Waves." *Applied Optics. 42(16):3205-3214,* June 2003.

Anjul M. Davis, Stephen A. Boppart, Florence G. Rothenberg, and Joseph A. Izatt. "OCT Applications in Developmental Biology." In *Optical Coherence Tomography: Technology and Applications.* In press (2008).